Gravitational Microlensing in the Milky Way with the Hubble Space Telescope and OGLE-III

A thesis submitted to The University of Manchester for the degree of
Doctor of Philosophy
in the Faculty of Engineering and Physical Sciences

2007

Szymon Kozłowski
School of Physics and Astronomy

Contents

List of Figures

List of Tables

The University of Manchester

ABSTRACT OF THESIS submitted by Szymon Kozłowski
for the Degree of Doctor of Philosophy and entitled
Gravitational Microlensing in the Milky Way with the *Hubble Space Telescope* and OGLE-III. August 2007

Gravitational lensing is a powerful tool for astronomers to study the Universe. It occurs on both cosmological and local (Galactic) scales. This thesis focuses on observational studies of Galactic microlensing, which, as I will show, have significant impact on studies of the Galactic structure and the mass function of lenses in the Milky Way.

The first chapter provides a basic treatment of gravitational lensing and of the data analysis procedures used throughout this thesis. The next chapter is devoted to the investigation of blending issues. The ground-based microlensed stars (blends) are resolved into separate components using the *Hubble Space Telescope* (*HST*). With Difference Image Analysis, seven microlensed stars are recognised. Blending fractions are calculated from the *HST* images and compared with the fractions derived from light curve fitting.

Chapters 3 and 4 present my studies of *HST* two-epoch images of 37 Galactic bulge fields; this work has been published in *Monthly Notices of the Royal Astronomical Society* and the *Astrophysical Journal*.

The superb resolution of the *HST* allows the measurement of stellar positions with milli-arcsecond accuracy. Using the two-epoch images, I build a catalogue of stellar proper motions for ~26,000 stars. For each field I calculate dispersions from the relative proper motions. Small gradients in these proper motion dispersions and in the anisotropy are clearly detected. For the first time, a covariance in the longitudinal and latitudinal motions is discovered. These results will provide strong constraints on theoretical Galactic models.

In the fourth chapter I present the first ever direct detection of a lens toward the

Galactic bulge. Using the *HST*, the luminous lens and source responsible for the microlensing event MACHO-95-BLG-37 were resolved. Having the colours of the stars, relative proper motion and parameters from the light curve fitting, I derive the distances to both the source and lens, as well as the lens mass. This method can in principle be extended to many other microlensing events in the future, and provides a promising way to constrain lens masses.

The final chapter presents an independent attempt to reduce the huge amount of OGLE–III data. To test the methodology, I focus on one OGLE–III field, in order to calculate the detection efficiency and derive the optical depth. I develop a pipeline for constructing template images, performing photometry and building a light curve database. The simulator for the OGLE–III images and the microlensing events' search engine are described. Reduction of the OGLE–III data combined with the Monte Carlo simulations leads to a robust determination of the detection efficiency and the optical depth $\tau = (2.91 \pm 0.77) \times 10^{-6}$ in the chosen field. The pipeline, together with the image simulator and calibration routines, will be used in the near future to construct the first observational map of the optical depth of the Galactic bulge.

Declaration

I declare that no portion of the work referred to in the thesis has been submitted in support of an application for another degree or qualification of this or any other university or other institute of learning.

Copyright Statement

Dedication

I would like to dedicate this work to
my parents – Jolanta and Marek Kozłowscy,
brother – Mariusz Kozłowski,
and grandparents – Teofila and Edmund Urbanek.

Acknowledgements

I would like to thank my parents Jolanta and Marek, brother Mariusz and grandparents Teofila and Edmund Urbanek for their continuous support and encouragement.

I am pleased to thank my supervisor Prof. Shude Mao, co-supervisor Dr. Przemysław R. Woźniak, advisor Prof. Ian W. Browne and collaborators: Dr. Łukasz Wyrzykowski, Dr. Nicholas Rattenbury, Dr. Eamonn Kerins, Dr. Alexander Wood, Dr. Martin C. Smith, Dr. Takahiro Sumi and Prof. Andrzej Udalski.

I thank Prof. Bohdan Paczyński, Prof. Andrew Gould, Prof. Joachim Wambsganss, Dr. Neal Jackson, Dr. Vasily Belokurov and Dr. Wyn Evans for helpful comments and discussions on my work.

I would like to thank my friends here at Jodrell Bank Observatory, whom I have been sharing life with for the last three years: Sanhita 'Aditi' Joshi, Ralph Eatough, Mike Keith, Ming Zhang, Dandan Xu, Satoru 'Saturn' Sakai, Cristobal Espinoza, Mike Peel, Richard Long, Dr. Megan Argo, Dr. Edward Boyce, Dr. Iain Brown, Dr. Paul Carr, Dr. David Champion, Dr. Adam Moss and Dr. Tom York as well as the always helpful staff: Directors of Jodrell Bank Observatory Prof. Phil Diamond and Prof. Andrew Lyne for making the facilities available for my research, Belinda Affleck, Mike Anderson, Dr. Myfanwy Bryce, Dr. Robert Dickson, Janet Eaton, Stella Freer, Beverley Hancock, Dr. Anthony Holloway, Prof. Ian Morison, Sarah Morris, Dr. Dave Stannard, Pat Stanway and Dr. Peter Thomasson.

I would also like to thank my friends and colleagues in Poland, the United Kingdom, Germany and the Netherlands: Marta Zub, Maciej Serylak, Krzysztof Maciesiak, Krzysztof Krzeszowski, Marina and Gio Melikidze, Prof. Gogi Melikidze, Prof. Janusz

Gil, Prof. Andrzej Maciejewski, Prof. Roman Juszkiewicz and Dr. Jarek Kijak, Dr. Marek Sendyk, Dr. Olaf Maron, Dr. Stanisław Wrona, Dr. Paweł Pietrukowicz and Dr. Robert Schmidt as well as Henryk Butkiewicz, Józef Grześkowiak, Andrzej Pilski, Emilia Gil, Władek Barylski, Emilia Jaśkiewicz, Mateusz Wiśniewicz, Elżbieta Łazarewicz-Wyrzykowska, Kasia and Andrzej Falenty, Szymon Schmidt, Magda and Maciej Lose, Radek Pior and Aleksander Dera.

This work was supported by the European Community's Sixth Framework Marie Curie Research Training Network Programme, Contract No. MRTN-CT-2004-505183 'ANGLES' to the Author through a generous studentship. I would like to thank all the memebers of our big ANGLES family.

This work would not be possible without the data obtained and delivered by the OGLE group. I am in particular thankful to Prof. Andrzej Udalski, Dr. Łukasz Wyrzykowski and Dr. Michał Szymański from the OGLE group for making the data available to me as well as for comments and discussions on the project.

This work also would not be possible without support for the proposal SNAP-10198, provided by NASA through a grant from the Space Telescope Science Institute, which is operated by the Association of Universities for Research in Astronomy, Inc., under NASA contract NAS5-26555.

I am grateful to Dr. Tom Vestrand, Dr. Przemysław R. Woźniak and Eloisa Michel for organising my two long visits to the Los Alamos National Laboratory, New Mexico, USA. Special acknowledgements to Prof. Bohdan Paczyński for support during my two visits to Princeton University, New Jersey, USA.

The Author

The Author was born in Zielona Góra, Poland in August 1979. He has been interested in Astronomy and Physical Sciences since he was nine years old. When he was 14 he joined the Polish Amateur Astronomical Society (PTMA). In 1999 he registered at the University of Zielona Góra, Poland, for both under- and graduate studies, where in September 2004 he obtained a MSc degree in Physics. His thesis was entitled ‘Deriving parameters of extrasolar planetary systems’. He then registered as a PhD student in Astronomy at the University of Manchester’s Jodrell Bank Observatory.

Supporting Publications

Publications

- **Kozłowski S.**, Woźniak P. R., Mao S., Wood A., 2007, ApJ in press – astro-ph/0701488
  The first direct detection of a gravitational microlens toward the Galactic bulge (Kozłowski et al. 2007).

- **Kozłowski S.**, Woźniak P. R., Mao S., Smith M. C., Sumi T., Vestrand V. T., Wyrzykowski Ł., 2006, MNRAS, 370, 435
  Mapping stellar kinematics across the Galactic Bar: HST measurements of proper motions in 35 fields (Kozłowski et al. 2006a).

Catalogues

- **Kozłowski S.**, Woźniak P. R., Mao S., Smith M. C., Sumi T., Vestrand V. T., Wyrzykowski Ł.
  Proper motions near Baade's Window (Kozłowski et al. 2006b).

Conference Contributions

- 17th January 2006, '*HST* proper motions of stars in the Galactic Bulge', The 10th Gravitational Microlensing Workshop, Nagoya, Japan

- 25th January 2006, '*HST* proper motions of stars in the Galactic Bulge', Galactic Bulges - EARA Workshop 2006, Padua, Italy

- 15th January 2007, 'The first direct detection of a gravitational microlens toward the Galactic bulge', The 11th Gravitational Microlensing Workshop, Daejeon, South Korea

- 24th January 2007, ‘The first direct detection of a gravitational microlens toward the Galactic bulge’, Seminar at Institute of Astronomy, University of Cambridge, UK

Posters

- Woźniak P. R., **Kozłowski S.**., Vestrand W. T., Mao S., 2005, AAS, 20713303 *HST Proper Motions in the Galactic bulge* (Woźniak et al. 2005).

The Galactic Centre Area

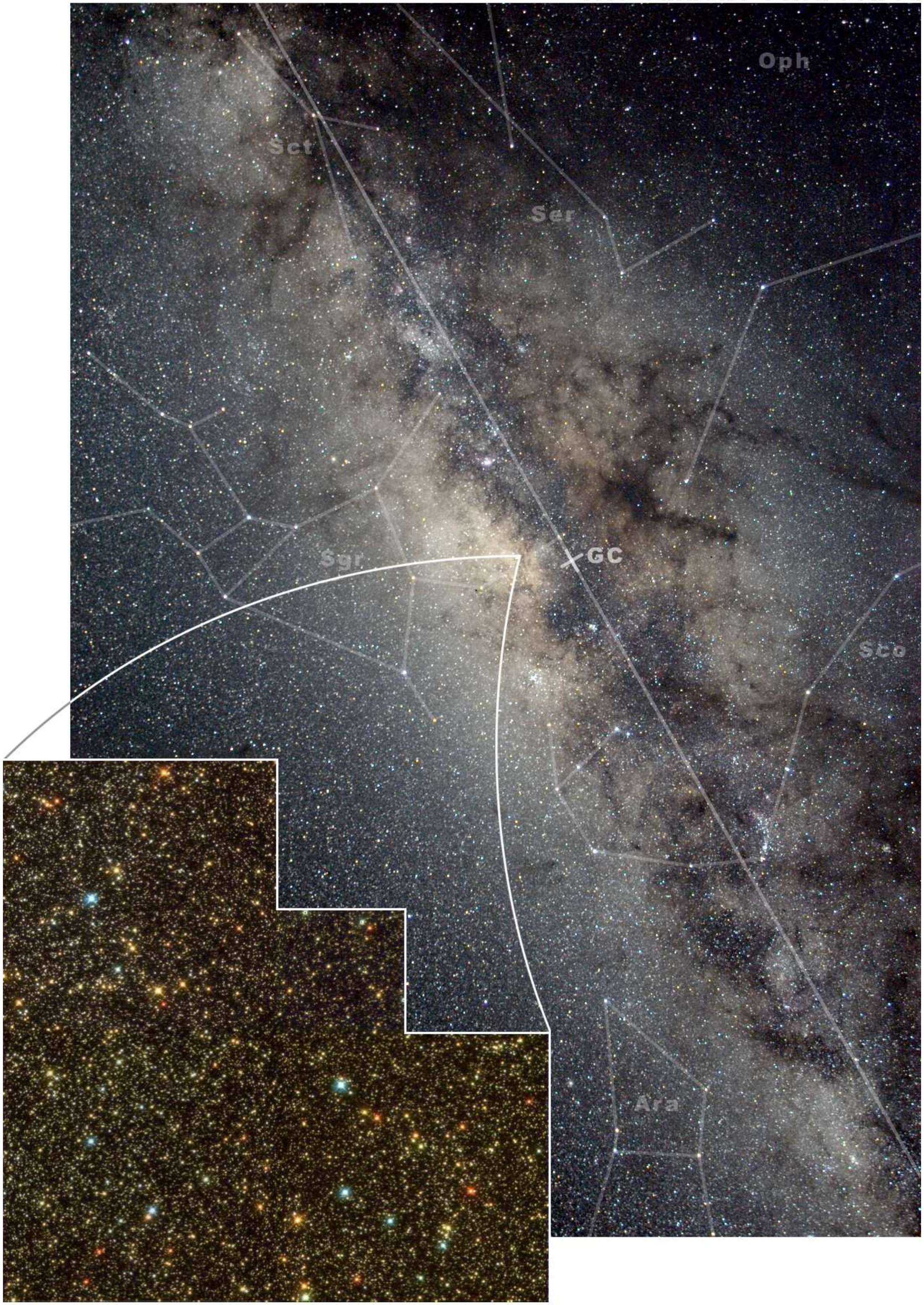

The field of MACHO-98-BLG-6 (HST/ WFPC2, S. Kozlowski)

1

Introduction

1.1 The Galaxy – Milky Way

Looking at the starry sky virtually all objects (except external galaxies such as M31 and the Magellanic Clouds) belong to the Galaxy – the formation of some 200 billion stars. Our Galaxy has the shape of a flat disk of about 30 kpc in diameter and 1 kpc in thickness (luminous component). The Galactic nucleus – some 8 kpc away (e.g. Paczyński and Stanek 1998) – hosts a supermassive black hole. Its mass is estimated to be three million solar masses (Ghez et al. 1998). There is a bulge surrounding the Galactic centre containing about 20 billion stars confined to a volume of several cubic kiloparsecs (e.g. Gerhard 2002). The view of the Galaxy from close to one of the Galactic poles would reveal the existence of a bar extending up to ~2 kpc from the Galactic centre and inclined at ~25° to the line of sight – the line joining Earth and the Galactic centre (e.g. Gerhard 2001; Rattenbury et al. 2007b). The younger (bluer) stars are spread over the Galactic disk, so called the thin disk. Its scale height is about ~300 pc and contains 95% of all the disk stars. The rest of the Galactic disk stars reside in the thick disk, with a height scale of ~1.2 kpc. These stars are older and redder. Within the Galactic disk, stars and gas form so-called spiral arms. There are three spiral arms between the Sun and the Galactic centre; counting along the line of sight to the Galactic centre they are the Sagittarius-Carina, Scutum-Crux and Norma arms, which are $\sim$1, $\sim$3 and $\sim$5 kpc away from us, respectively (Figure 11 in Georgelin and Georgelin 1976). Our Sun resides in the fourth arm, Orion. All three inner arms are host to increased densities of stars and gas, causing the patchy extinction of the bulge. Finally, the luminous Galaxy is surrounded by a quasi-spherical halo of dark matter and globular clusters. The Galactic dark matter halo contains roughly 90% of the total mass of the Galaxy.

1.1.1 The Galactic bulge / bar

The Galactic bulge hosts $\sim$10% of the Milky Way stars. They are distributed in a tri-axial structure – the bar. The earliest hints of the existence of the Galactic bar came as early as the 1960s from studies of the non-circular gas kinematics (de Vaucouleurs et al. 1964). Later on, in the 1990s as by-products of the optical sky surveys of the Galactic centre, for example the Optical Gravitational Lensing Experiment (OGLE, e.g. Udalski et al. 1994c), some interesting results were found regarding the asymmetries in star counts (e.g. Stanek et al. 1994), and differences in the apparent magnitudes of the Red Clump Giant stars (RCGs; standard candles) along the Galactic longitude (Stanek et al. 1994; Sumi et al. 2006), which were interpreted as a result of an inclined bar. Yet another way of proving the existence of the Galactic bar comes from microlensing. The first observation-based optical depths (probabilities of finding the microlensing events) were of a factor $\sim$6 higher than the predicted ones (e.g. Paczyński 1991 for theoretical values, and Udalski et al. 1994c; Alcock et al. 1997 for observed ones). An agreement was achieved by introducing a bar to the state-of-the-art Galactic models. This increases the theoretical optical depths by a factor of 3 – 4. An improving statistics of microlensing events reduced the observed values by $\sim$30%, reaching an agreement at $\tau \approx 2 \times 10^{-6}$ toward Baade's Window ($l = 1^\circ, b = -4^\circ$).

1.1.2 Dark matter in the Galactic halo

Observations of other spiral galaxies as well as our own show a significant discrepancy between the predicted circular velocities, based on the mass of the luminous component, and the observed ones. It is accepted nowadays that the 'missing' dark matter causing flat rotation curves is distributed thoughout the Galactic halo (e.g. Persic et al. 1996). If that matter was clumped into MAssive Compact Halo Objects (MACHOs; e.g. de Rujula et al. 1992), they would act as lenses to luminous background objects. The exciting idea of the Galactic halo being made of MACHOs, however, was proved to be false. If the Galactic halo was entirely made of MACHOs, with masses between 10^{-8} and 10^{8} $M_{\odot}$, we should detect dozens of microlensing events per year toward the Large Magellanic Cloud (LMC), and the corresponding optical depth would be $\tau_{\rm total} \approx 4.7 \times 10^{-7}$ (Bennett 2005). The actual optical depth measured by microlensing experiments is much smaller. The MACHO collaboration (Bennett et al. 1993), for example, presented a sample of about 10 microlensing event candidates toward the LMC and concluded that the fraction of dark matter in MACHOs ($f = \tau_{\rm MACHO}/\tau_{\rm total}$) is $f = 16 \pm 6\%$, suggesting the existence of a new, previously unknown population of MACHOs with masses ~ 0.5 $M_{\odot}$ (Alcock et al. 2000a; Bennett 2005). Their estimate of the optical depth toward the LMC is $\tau_{\rm LMC} = (1.0 \pm 0.3) \times 10^{-7}$. However, the EROS group (e.g. Aubourg et al. 1993), reported a null result based on their bright star sample and derived an upper limit on the optical depth due to MACHOs of $\tau_{\rm MACHO} < 0.36\times10^{-7}$, which implies $f \lesssim 8\%$ (Tisserand et al. 2007). The OGLE group reports $\tau_{\rm MACHO} = (0.45 \pm 0.25) \times 10^{-7}$ and $f \lesssim 10\%$ based on four microlensing candidates found in the OGLE–II database (Wyrzykowski 2007, private communication). Observations of microlensing events toward the Andromeda Galaxy (M31), however, show that the fraction of dark matter in MACHOs may be higher than 20% (Uglesich et al. 2004; Calchi Novati et al. 2005).

1.1.3 Toward a better understanding of the Galaxy

The research presented in this thesis is aimed at improving our understanding of the Galactic bulge/bar.

We start off with an analysis of the blending issues (blurring at least two stars into one object, as seen from the ground-based observations), which are present in all microlensing surveys. Using the *HST* we resolve seven microlensed stars from the OGLE–III database, derive the blending fractions and show the shift of a blend's centroid. The *HST* images, however, were taken in different pass bands from the $I-$band used by OGLE. Nevertheless, we were able to pinpoint the microlensed sources and find the blending fractions empiricaly, which were then compared with those found from the fitting of the light curve (Chapter 2).

The velocity dispersions along the Galactic longitude and latitude were measured using the *Hubble Space Telescope* (*HST*) and are presented in Chapter 3. We find small trends in the velocity dispersions with respect to the Galactic coordinates. For the first time we measure a covariance term in the longitudinal and latitudinal motions. These results will provide strong constraints on the theoretical models. Results from subsequent study by Rattenbury et al. (2007a) using the OGLE–II proper motions are in rough agreement with the values of dispersions and covariance term derived from the *HST*. These two papers show a new direction for Galactic bulge studies.

Further information on the Galactic bulge can be derived from the microlenses themselves. It is clear that a decade after detection of the first microlensing events it becomes possible to resolve a (luminous) lens and source with the *HST*. Chapter 4 is a presentation of a lens mass measurement. The increasing number of observed microlensing events opens another new direction for studies of the stellar mass function.

It would be interesting to compare a Galactic map of the optical depth to predictions from existing theoretical models. The current detection rate of microlensing events of ~500 per year allows the construction of such a map. Chapter 5 presents a calculation of the optical depth toward one of the bulge fields using data from the OGLE–III collaboration. This procedure, in principle, can be repeated for all bulge fields.

1.2 Microlensing surveys

Paczyński (1986) envisaged that observations of millions of stars in very dense fields in the direction of the bulge, Large and Small Magellanic Clouds (LMC & SMC) and Andromeda Galaxy (M31) should result in detections of the microlensing events. If the dark Galactic halo is made of dark compact objects there would be a non-zero probability that such objects could act as lenses of the background stars. In that paper Paczyński calculated the rough value of the optical depth in the direction of the bulge as $\tau \approx 0.4 \times 10^{-6}$. A few years after this publication many observational projects began to operate. Astronomers working in those groups wanted to confirm or reject the thesis of Paczyński. Thousands of events have been found so far, including exotic ones such as binary and planetary microlensing events.

A brief description of the major past and present microlensing surveys is presented below.

1.2.1 The OGLE, MACHO, EROS and MOA collaborations

One of the first established groups which dedicated its new telescope to search for microlensing events was a group of astronomers from the Warsaw Astronomical Observatory. The OGLE[1] group, under the supervision of Profs. B. Paczyński and A. Udalski, placed its telescope high in the mountains in Las Campanas, Chile. A new telescope with a mirror of 1.3 m diameter monitors millions of stars mainly in the bulge, LMC and SMC. The group started operation at the beginning of 1992. The most recent (third) phase, OGLE–III, has been working since 2001. Seven years of observing mainly the bulge have given about 3000 new microlensing events. OGLE–III

---

[1] `http://www.astrouw.edu.pl/~ogle/`

operates with a mosaic of eight CCD[2] chips each with 2048x4096 pixels, which gives a total of 8192x8192 pixels. The coverage of the sky is approximately equal to 0.26 arcsec per pixel, so the total field of view is $35' \times 35'$. Nowadays OGLE–III monitors ~200 million stars in the bulge.

Another group searching for microlensing events was the MACHO[3] collaboration. Their main objective was to prove that most dark matter within the Galaxy is made of objects such as brown dwarfs or planets. After a few years of observations it turned out that dark matter in the Galaxy is not made of these objects (less than 20%; Alcock et al. 2000a). MACHO's telescope with a mirror of 1.25 m diameter was placed at Mt. Stromlo, Australia. A double channel (colour) set of eight CCD chips was mounted at the focal plane of the telescope. The group started to monitor millions of stars in June 1992; the observations were finished in 1999.

The main objective of the EROS[4] (Experience pour la Recherche d'Objets Sombres) project is the search and study of dark stellar bodies such as brown dwarfs or MACHOs which are bound gravitationally to our Galaxy. EROS started operating in 1990. In the first phase of the project astronomers were using a 0.4 m telescope equipped with a 3.5-megapixel CCD camera. Nothing was found. Subsequent phases using 1.0 m and 1.5 m telescopes turned out to be more successful.

The MOA[5] (Microlensing Observations in Astrophysics) project is a Japanese and New Zealander collaboration that makes observations of dark matter, extra-solar planets and stellar atmospheres using the gravitational microlensing technique at the Mt. John Observatory in New Zealand. Since 1st December 2004 they have operated with a new 1.8 m class telescope.

---

[2] CCD stands for Charge Coupled Device; CCD detectors are most common astronomical detectors used in optical astronomy.

[3] `http://wwwmacho.mcmaster.ca/`

[4] `http://eros.in2p3.fr/`

[5] `http://www.phys.canterbury.ac.nz/moa/`

1.2.2 Follow-up surveys

Apart from the ‘regular’ microlensing experiments there also exist so-called microlensing follow-up networks. These networks operate on a number of telescopes spread over the globe, and are meant to deliver dense sampling of the most interesting events found by the regular microlensing surveys. The follow-up networks have been very successful so far, discovering for example four microlensing planets (Bond et al. 2004; Udalski et al. 2005; Beaulieu et al. 2006; Gould et al. 2006).

The Micro-FUN Collaboration[6] uses about 15 telescopes mainly of 0.4 m size. Five bigger telescopes are also involved, including the 2.4 m Hiltner telescope at MDM Observatory, the 60 inch Palomar telescope and three 1 m class telescopes.

PLANET[7] (Probing Lensing Anomalies NETwork) is a network of five telescopes: two 1.5 m telescopes, two 1 m telescopes and one 0.6 m telescope. The primary goal of this collaboration is to monitor microlensing events densely (median sampling of 1.6 h) in order to detect and study anomalies such as planetary microlensing.

The RoboNet Collaboration[8] is a network of three 2 m class telescopes. It is a collaboration of 10 UK universities, and its main goal is to deliver a dense sampling of astronomical phenomena such as planetary microlensing and gamma-ray bursts.

1.2.3 Microlensing surveys toward the Andromeda Galaxy (M31)

At a distance of ~780 kpc the nearest big galaxy, the Andromeda Galaxy, provides another unique line of sight to probe the dark matter halos of the Galaxy and M31 itself. The ongoing surveys have been successful, so far detecting both microlensing events and plenty of new variable stars.

The ongoing microlensing surveys of the Andromeda Galaxy are:

---

[6] `http://www.astronomy.ohio-state.edu/~microfun/`

[7] `http://planet.iap.fr/`

[8] `http://www.astro.livjm.ac.uk/RoboNet/`

Angstrom[9]: Andromeda Galaxy Stellar Robotic Microlensing Project – a survey searching for microlensing events in the Andromeda galaxy. The project uses five 2 m class telescopes at different locations across the planet. Similarly to the follow-up networks, this in principle allows for continuous observations of any event.

The POINT-AGAPE Collaboration[10]: This group uses the 2.5 m class Isaac Newton Telescope (INT) at La Palma, Canary Islands.

WeCAPP[11]: The Wendelstein Calar Alto Pixellensing Project uses a 1.23 m telescope located at Calar Alto, Spain and the Wendelstein 0.8 m telescope in Germany.

MEGA[12] (Microlensing Experiment Towards the Galaxy in Andromeda) is a microlensing and variable star survey of M31. Data are collected from the telescopes at Kitt Peak National Observatory (MDM), La Palma (INT), Mauna Kea (8.2 m Subaru Telescope and 3.6 m Canada-France-Hawaii Telescope).

1.3 Gravitational microlensing

1.3.1 Basics

One of the consequences of the General Theory of Relativity is the bending of a light ray passing a nearby massive object. The first theoretical calculations of the deflection angle based on Newtonian classical mechanics were made by Cavendish in 1794 and Söldner in 1801. Over a hundred years later (1916) Albert Einstein, using the General Theory of Relativity, predicted that this angle should be twice that derived by Cavendish and Söldner. The final equation for the deflection angle is given by (Refsdal 1964; Paczyński 1996)

---

[9] `http://www.astro.livjm.ac.uk/angstrom/index.php/The_Angstrom_Project`

[10] `http://www.point-agape.org/`

[11] `http://www.usm.uni-muenchen.de/people/arri/wecapp.html`

[12] `http://www.astro.columbia.edu/~arlin/MEGA/`

$$\alpha = \frac{4GM}{Rc^2}, \tag{1.1}$$

where G is the gravitational constant, M is the mass of the object, R is the impact parameter (the minimum distance of the light ray to the lens) and c is the speed of light. It quickly turned out that this phenomenon might have many applications in astronomical research. Zwicky (1937) predicted that distant galaxies might cause amplification of more distant objects. Galaxies with masses of order of $10^{11}\mathrm{M}_\odot$ can be used as 'big telescopes' to magnify background quasars. The first detection of a gravitational lens was made by Walsh et al. (1979). Paczyński (1986) suggested that even compact objects within the Galaxy may cause observable changes in the brightness of more distant stars in the Galactic bulge and nearby galaxies of the Local Group.

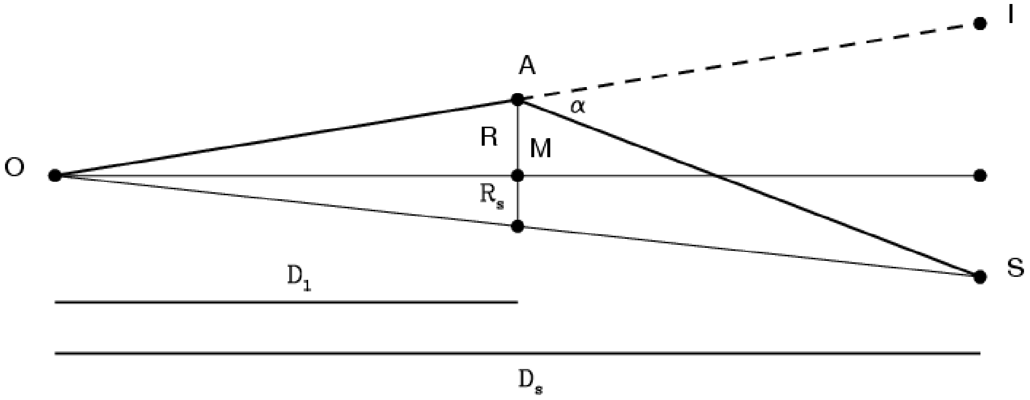

Figure 1.1: The side view of a gravitational lens is shown (from Paczyński 1996).

Figure 1.1 shows the lensing geometry. There are four main points marked on the figure: the observer O, lensing object M (point lens), source S and the image I. The distance between the observer and the lensing object D_l and the distance between the observer and the source D_s are marked. A light ray travels from S to the point A where it is deflected by the lens M and then travels to the observer O. The angle on the sky between M and S is equal to $R_\mathrm{s}/D_\mathrm{l}$, and the angle between M and I is equal to R/D_l, where R_s and R are linear distances between M and S, and M and I in the lens plane, respectively.

From Figure 1.1 simple geometrical dependencies can be deduced. The 'lens equation' can be written as

$$R + R_\mathrm{s} = \alpha(D_\mathrm{s} - D_\mathrm{l})\frac{D_\mathrm{l}}{D_\mathrm{s}} = \frac{4GM}{Rc^2}\frac{(D_\mathrm{s} - D_\mathrm{l})D_\mathrm{l}}{D_\mathrm{s}}. \tag{1.2}$$

We can rewrite this equation as

$$R^2 + R_\mathrm{s}R - R_\mathrm{E}^2 = 0, \tag{1.3}$$

where $R_\mathrm{E}^2 = 2R_\mathrm{g}D$ and $D = (D_\mathrm{s} - D_\mathrm{l})D_\mathrm{l}/D_\mathrm{s}$ and $R_\mathrm{g} = 2GM/c^2$. Equation 1.3 has two solutions which correspond to two images of the source S. The images of the source are on opposite sides of the lens M (Figure 1.2) at distances

$$R_\pm = \frac{1}{2}\left[R_\mathrm{s} \pm \left(R_\mathrm{s}^2 + 4R_\mathrm{E}^2\right)^{\frac{1}{2}}\right], \tag{1.4}$$

which correspond to angles $\theta_+ = R_+/D_\mathrm{l}$ and $\theta_- = R_-/D_\mathrm{l}$ on the sky (Figure 1.2).

Gravitational lensing conserves the surface brightness. The ratio A of the image and source fluxes can be calculated directly from the ratio of their areas:

$$A_\pm = \left|\frac{R_\pm}{R_\mathrm{s}}\,\frac{dR_\pm}{dR_\mathrm{s}}\right| = \frac{u^2 + 2}{2u\,(u^2 + 4)^{\frac{1}{2}}} \pm \frac{1}{2}, \tag{1.5}$$

where $u = R_\mathrm{s}/R_\mathrm{E}$. The amplification during a lensing event is given by

$$A = A_+ + A_- = \frac{u^2 + 2}{u\,(u^2 + 4)^{\frac{1}{2}}}. \tag{1.6}$$

All objects in the Universe are in permanent motion. Geometrical configurations between celestial objects change over time. During the motion of the massive body M with respect to the source S, the parameter u changes in the following way:

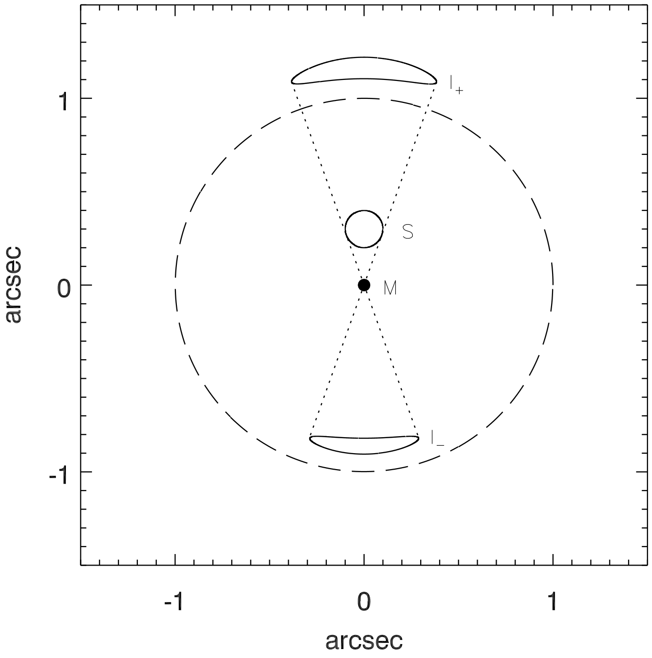

Figure 1.2: The gravitational lens geometry as seen on the sky is shown. The Einstein ring (if the M and S are aligned the two images merge together into a ring image), shown here as the dashed circle, has a dimeter of 1 arcsec.

$$u(t) = \sqrt{u_0^2 + \left(\frac{t - t_{\mathrm{max}}}{t_{\mathrm{E}}}\right)^2}, \tag{1.7}$$

where u_0 is the minimum impact parameter (Figure 1.4), which describes the minimal angular distance between the massive body M and the source S normalised to the angular Einstein radius $\theta_{\mathrm{E}} = R_{\mathrm{E}}/D_{\mathrm{l}}$, and t_{max} is the time of the closest approach. The smaller the impact parameter u_0, the higher the magnification A during the microlensing event (Figure 1.3). The standard magnification curves are shown in Figure 1.3.

The configuration shown in Figures 1.1 and 1.2 is temporary and the characteristic time duration t_{E}, the time taken by the lens to cross one Einstein radius R_{E}, is

$$t_{\mathrm{E}} = \frac{R_{\mathrm{E}}}{v_{\mathrm{t}}}, \tag{1.8}$$

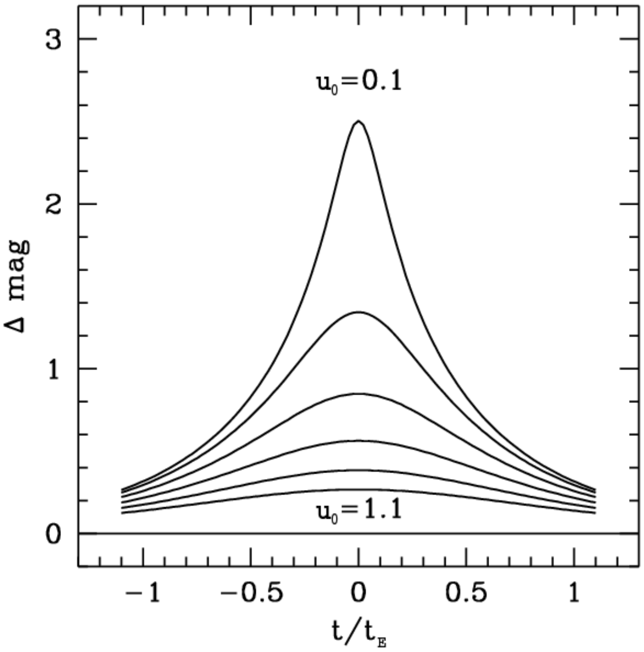

Figure 1.3: The standard magnification curves are shown. The smaller the impact parameter u_0 the higher the magnification during the event (from Paczyński 1996).

where v_t is the transverse velocity of the massive body M with respect to the source S. For objects moving within our Galaxy equation 1.8 can be rewritten as

$$t_E = 0.214 \left(\frac{M}{M_\odot}\right)^{1/2} \left(\frac{D_l}{10\ \mathrm{kpc}}\right)^{1/2} \left(1 - \frac{D_l}{D_s}\right)^{1/2} \left(\frac{200\ \mathrm{km\ s}^{-1}}{v_t}\right) \mathrm{year}. \tag{1.9}$$

Simple calculations show that the timescale of microlensing events in the Galaxy is of the order of one month.

All microlensing experiments observe dense stellar fields such as the Galactic bulge, LMC, SMC and M31. On the ground-based images many stars are blended together, so a lensed star usually contributes only a fraction of the total blend's flux. This fraction, f_s, can be defined as

$$f_s = \frac{F_s}{F_s + \mathrm{F_b}}, \tag{1.10}$$

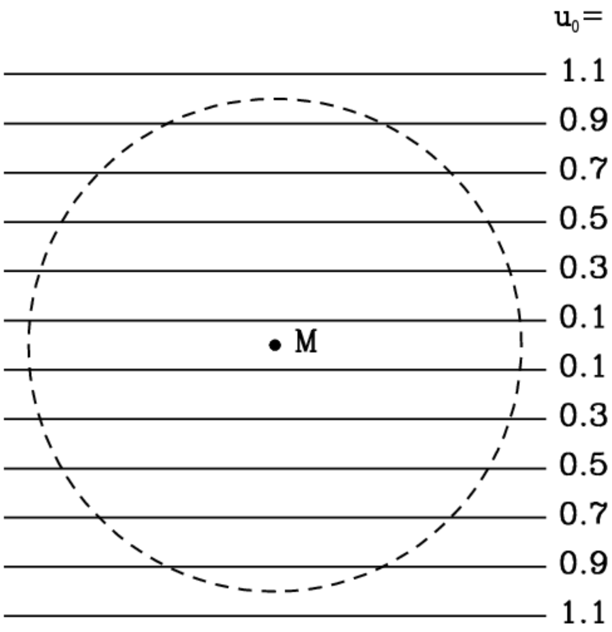

Figure 1.4: Trajectories of the source relative to the lens for given impact parameters u_0 are shown. The dashed line indicates the Einstein ring for the lens M (from Paczyński 1996).

where F_s is the flux of the lensed source and F_b is the flux of the remaining stars within the blend. A standard light curve modelling is based on a five parameter fit to the data,

$$m_\mathrm{observed} = m_\mathrm{baseline} - 2.5 \log(f_\mathrm{s}(A-1)+1) \tag{1.11}$$

where m_baseline is the baseline magnitude of the blend, f_s is the blending fraction, and the magnification A depends directly (through Equations 1.6 and 1.7) on three more parameters: t_max, the peak time; t_E, the Einstein radius crossing time; and u_0, the minimum impact parameter.

1.3.2 The optical depth

The probability of a microlensing event occuring at any given time in any direction on the sky is called the optical depth, τ. All lenses between the observer and source contribute to the total optical depth, which can be calculated as

$$\tau = \int_0^{D_\mathrm{s}} \frac{4\pi G\rho(D_\mathrm{l})}{c^2} \frac{(D_\mathrm{s} - D_\mathrm{l})D_\mathrm{l}}{D_\mathrm{s}} dD_\mathrm{l}. \qquad (1.12)$$

where ρ is the average mass density along the line of sight. An experiment-based optical depth can be calculated from the equation

$$\tau = \frac{\pi}{2N_* T_\mathrm{exp}} \sum_i^{N_\mathrm{events}} \frac{t_{\mathrm{E},i}}{\epsilon(t_{\mathrm{E},i})}, \qquad (1.13)$$

where N_* is the total number of stars a given experiment monitors, T_exp is the duration of the experiment, $t_{\mathrm{E},i}$ is the Einstein radius crossing time of the i-th event, and $\epsilon(t_{\mathrm{E},i})$ is the detection efficiency as a function of timescale.

1.4 Data Analysis Techniques

Throughout this thesis I use various techniques to analyse astronomical data. In this section I briefly describe different photometric and astrometric techniques.

1.4.1 Profiles of stars

A star's profile usually resembles a Gaussian and can be divided into two different parts: the core and the wings. There is no clear distinction between the core and wings but this border lies approximately 2 sigma from a star's centre. In astronomy we use several different profiles:

Gaussian profile (elliptical)[13]

A star's flux intensity I at a position (x, y) can be calculated from

---

[13] based on IRAF manual.

$$\begin{aligned}
I(x,y) &= I_0 \exp\left(-\frac{1}{2}z^2\right) + I_b, && (1.14)\\
z^2 &= c_1(x-x_0)^2 + c_2(y-y_0)^2 + c_3(x-x_0)(y-y_0), && (1.15)\\
c_1 &= \frac{\cos^2\phi}{\sigma_x^2} + \frac{\sin^2\phi}{\sigma_y^2}, && (1.16)\\
c_2 &= \frac{\sin^2\phi}{\sigma_x^2} + \frac{\cos^2\phi}{\sigma_y^2}, && (1.17)\\
c_3 &= 2\sin\phi\cos\phi\left(\frac{1}{\sigma_x^2} - \frac{1}{\sigma_y^2}\right). && (1.18)
\end{aligned}$$

This profile has seven parameters: I_0 – the central intensity, I_b – the background intensity, x_0 and y_0 – the position of a star, ϕ – the position angle of the point spread function (PSF), σ_x and σ_y – describing both shape and size of the PSF. The full width at half maximum (FWHM) of a Gaussian profile is expressed as $\mathrm{FWHM}_{x,y} = 2\sqrt{2\ln 2}\,\sigma_{x,y} \approx 2.355\,\sigma_{x,y}$[14].

Pseudo-Gaussian profile (elliptical)[15]

$$\begin{aligned}
I(x,y) &= I_0\left(1 + z^2 + \frac{1}{2}\beta_4 z^4 + \frac{1}{6}\beta_6 z^6\right)^{-1} + I_b, && (1.19)\\
z^2 &= \frac{1}{2}\left(c_1(x-x_0)^2 + c_2(y-y_0)^2 + c_3(x-x_0)(y-y_0)\right), && (1.20)
\end{aligned}$$

where β_4 and β_6 are user-adjustable parameters. This profile is derived from the Gaussian function expanded in a Taylor series, and dropping terms higher than third order. It is used in the D P software (Schechter et al. 1993). The pseudo-Gaussian allows for better handling of the PSF wings.

Generic profile (elliptical)

$$I(x,y) = I_0\left(1 + \frac{1}{2}z^2\right)^{-\alpha} \qquad (1.21)$$

---

[14] based on `http://mathworld.wolfram.com/GaussianFunction.html`

[15] based on D P manual.

The parameter α defines different profiles: $\alpha = 0.9$ – Lugger profile, $\alpha = 1$ – Hubble profile, $\alpha = X.Y$ – MoffatXY profile. The parameter z for this profile is given by equations 1.15 – 1.18.

1.4.2 Aperture photometry

The easiest way of measuring a star's brightness is to use aperture photometry. This technique is based on measuring the flux of a star and the background flux in two different areas. We define three annuli, all of them centered on the star. The radius of the inner annulus should be about 2.5 times the FWHM of that star – this is where we measure the star's flux. A star's profile is Gaussian-like, where the wings extend to the distance of many FWHM from the star's centre. Therefore setting up the middle and outer annuli should be done at the distance from the star's centre, where the star does not contribute the flux to the background ring, preferably with the middle annulus at 4 FWHM from the centre. The area of the background ring (area between the middle and outer annuli) should be about three times the area within the inner annulus.

The measurement procedure is as follows:

$$f_{\mathrm{star}} = \sum_{i=1}^{n_{\mathrm{pix}}} f_i - \frac{n_{\mathrm{pix}}}{m_{\mathrm{pix}}} \sum_{j=1}^{m_{\mathrm{pix}}} b_j, \tag{1.22}$$

where f_{star} is the star's total flux, f_i is the flux value per pixel inside the inner annulus, b_j is the flux value per pixel inside the background ring, and n_{pix} and m_{pix} are the numbers of pixels within the inner annulus and inside the background ring, respectively.

As the wings extend – in principle – to 'huge' distances, the inner radius does not collect all the flux from the star. To account for the wing's flux we apply an aperture correction. This procedure is done by measuring the ratio of fluxes for very bright stars while changing the inner radius size. Knowing the ratio of fluxes which are contained between the inner and 'infinite' annuli and within the inner annulus we can introduce an aperture correction to any star in our field.

Aperture photometry is applicable only to sparse stellar fields, where we are actually in a position to set up all three annuli without having any star inside the background ring. In the ground-based experiments it is rather impossible to get reliable results using aperture photometry for dense stallar fields such as the Galactic bulge, globular clusters, etc.

1.4.3 Signal-to-Noise Ratio

One of the most important characteristics of the data analysis is the signal-to-noise ratio (S/N). In the case of image analysis it usually describes how well a star (or other object) is defined on an image (how strong or bright it is). With S/N $\approx$ 3 one can say that the star is marginally detected, while S/N $\approx$ 100 represents a good quality detection. The higher the S/N the better the photometric and astrometric accuracy.

The first order calculation of the S/N, taking into account only a stars's flux, is governed by the Poisson statistics and can be written as

$$S/N = \frac{N}{\sqrt{N}} = \sqrt{N}, \tag{1.23}$$

where N is the measured flux (in electrons, not ADUs – Analog-to-Digital Units). In order to convert ADUs to electrons the number counts in ADUs have to be multiplied by the gain (G) of the CCD detector.

Since the CCD detectors are electronic devices, they generate noise themselves. The S/N equation accounting for all additional sources of CCD-related noise is expressed as

$$S/N = \frac{N}{\sqrt{N + n_{\rm pix}\left(1 + \frac{n_{\rm pix}}{n_B}\right)\left(N_S + N_D + N_R^2 + G^2\sigma_f^2\right)}}, \tag{1.24}$$

where $n_{\rm pix}$ is the number of pixels, n_B is the number of background pixels, N_S is the total number of the background photons per pixel, N_D is the total number of the dark current photons per pixel, N_R is the total number of the read noise photons per pixel and σ_f is an estimation of the 1σ error in the A/D converter. A thorough summary of CCD related topics is given in Howell (2000).

The astrometric precision depending on the S/N is described in detail in Kuijken & Rich (2002). The 1σ uncertainties in the position of a star described by the Gaussian and Moffat15 profiles are as follows:

$$1\sigma_{\mathrm{Gaussian}} = 0.6\,\frac{\mathrm{FWHM}}{\mathrm{S/N}}, \qquad 1\sigma_{\mathrm{Moffat15}} = 0.67\,\frac{\mathrm{FWHM}}{\mathrm{S/N}}. \tag{1.25}$$

1.4.4 Profile photometry (and astrometry)

A better way of handling very crowded fields is using the profile photometry. The procedure of measuring magnitudes in dense fields is as follows: we chose a representative number of bright but not saturated stars. It is quite easy to fit one of the profiles described in §1.4.1 to the sample of stars. Since it is very likely that one star would have two different PSFs in two different places on a CCD chip, it is wise to perform spatial fitting of the PSFs (especially for big arrays). This is done by allowing parameters such as σ's and ϕ to vary with position, e.g. $\sigma_x(x, y)$ or $\phi(x, y)$. Having built the (spatially variable) PSF we can use it to fit to the fainter stars. This procedure is likely to split properly the flux between the stars of a blend (which is impossible with aperture photometry). So after the first iteration all bright stars are measured and then subtracted out from the image. In the next iteration another ‘level’ of magnitudes is measured and the stars are subtracted out from the image. Each iteration reveals fainter and fainter stars. Depending on the stellar density it usually takes a couple of dozen iterations to reach the level where ‘all’ stars are subtracted and the fitting of the profiles does not converge to acceptable χ^2 (no more stars are detected).

1.4.5 Fitting PSFs (models) to the data

In order to derive parameters of the PSF (and later on the magnitude and position of a star) we have to fit a chosen profile (§1.4.1) to the data. The goodness of the fit is estimated using chi-squared function – χ^2 (depending on the parameters $\mathbf{p}$), which needs to be minimized. The simplest way of estimating χ^2 is the least-squares method. We look for such a set of parameters **p**, for which the function $\chi^2(\mathbf{p})$ reaches the smallest value. The chi-squared function is expressed as

$$\chi^2 = \sum_{i=1}^{N} \left(\frac{x_{\mathrm{obs},i} - x_{\mathrm{model},i}(\mathbf{p})}{\sigma_i} \right)^2 , \tag{1.26}$$

where N is the number of fitted data points (pixels), $x_{\mathrm{obs},i}$ is the observed value on i^{th} pixel, $x_{\mathrm{model},i}(\mathbf{p})$ is the modelled value on the i^{th} pixel, and σ_i is the uncertainty of an observed value on the i^{th} pixel. The reduced $\chi^2(\mathbf{p})$ (per degree-of-freedom, dof) can be expressed as

$$\chi^2_{dof} = \frac{1}{N - N_p} \sum_{i=1}^{N} \left(\frac{x_{\mathrm{obs},i} - x_{\mathrm{model},i}(\mathbf{p})}{\sigma_i} \right)^2 , \tag{1.27}$$

and if the model is correct χ^2_{dof} should be close to unity. N_p is the number of fitted parameters.

There are two ways of arriving at the minimum of χ^2 function: using either gradient or non-gradient methods.

Gradient methods are based on finding the maximum change of χ^2. To do so we have to differentiate our function over the parameters **p**, which gives us the gradient of the function. The general method is as follows. For an initial set of parameters **p** we calculate both the gradient and value of the function χ^2. Next, we make small a step in the opposite direction to the gradient and for a new set of parameters we calculate a new gradient and value of the function χ^2. We repeat this procedure until we reach the minimum of the function, i.e. when the gradient squared is smaller than a given tolerance. There are various types of gradient methods. The most common ones are: gradient descent, conjugate gradient method, Levenberg-Marquardt algorithm, etc. (e.g. Press et al. 1992).

Non-gradient methods are based on finding a change of χ^2, by calculating values of the function for different points (different parameter sets) and following the path of its decreasing value. The minimum is reached when the difference in values of adjacent points is smaller than a desired tolerance. The most commonly used non-gradient methods are simplex and genetic algorithms.

Minimization package M

During the course of the work in this thesis most applications for finding the minimum of a funcion used the minimisation package M[16]. M is a clever set of routines for finding the minimum of a function χ^2 as defined in Equation 1.26. Depending on the problem a user can choose either a gradient method (M), non-gradient method (S) or both (M). Another routine, M, allows the proper determination of errors, as it accounts for both parameter correlations and non-linearities. A detailed description of the package can be found at `http://wwwasdoc.web.cern.ch/wwwasdoc/minuit/`.

1.4.6 Difference Image Analysis

Measuring well-separated stars' fluxes is a relatively easy task to perform (§1.4.2). A more complicated issue is to measure the brightness of a given star in a very crowded field. The measured flux is usually contaminated by the flux(es) of the neighbour star(s), known as blending. The only method of spliting flux between stars making up a blend is profile photometry (§1.4.4). This is, however, a difficult task. If one intends to measure the residual flux of a variable object, which changes its brightness over time, one may use Difference Image Analysis (DIA). This method has been developed by Alard and Lupton (1998) and later on by Woźniak (2000) and Woźniak et al. (2001). Procedures written by Woźniak (2000) are available for download at `http://www.camk.edu.pl/~pych/` or `http://science.simkoz.com/`. One example of a comparison of profile photometry and DIA is showed in Figure 1.5.

The primary idea of DIA is to match (both astrometricaly and photometrically) an image – which is to be analysed – with a good-seeing reference image. Having both images registered in the same reference frame, the subtraction of one from the other

---

[16] `http://wwwasdoc.web.cern.ch/wwwasdoc/minuit/`

gives us the residual flux. If the PSFs are well matched the residual image will reveal mainly the photon noise across the whole image with sparse positive or negative residuals due to variable objects. There might be other reasons for the positive or negative residuals, such as: saturated stars, cosmic-rays, wrong astrometric or photomeric matching, wrong setup of parameters for the subtraction process, and fast moving objects, etc.

The method

In the first step of DIA a reference (template) image needs to be chosen. It can be a single good-seeing and low-background image, or if we have plenty of images for the same area of sky, we can build the template image using the best available images. Stacking about a dozen images is preferred over a single image, as it is characterised by higher signal-to-noise ratio and lower background. In addition it allows for removal of cosmic-rays. In the next step each analysed image is registered in the coordinate frame of the reference image. Having done that we are able to convolve the template image to match the seeing of the other, analysed frames. Finding the kernel of a transformation (a function transforming the template image to match an analysed image) is done by finding the least-square solution (§1.4.5) of the equation

$$I(x,y) = Kernel(x,y;u,v) \otimes Ref(u,v) + Bkg(x,y), \tag{1.28}$$

where $Ref(u,v)$ denotes our reference image, $I(x,y)$ is an analysed image, $Bkg(x,y)$ is the difference between backgrounds of two images and the symbol $\otimes$ denotes convolution. Solving Equation 1.28 is a non-linear problem, which means that finding a solution is very time-consuming for computers. The problem can be linearised by decomposition of the kernel using basis functions (Gaussians multiplied by polynomials) and becomes a standard linear least-square problem.

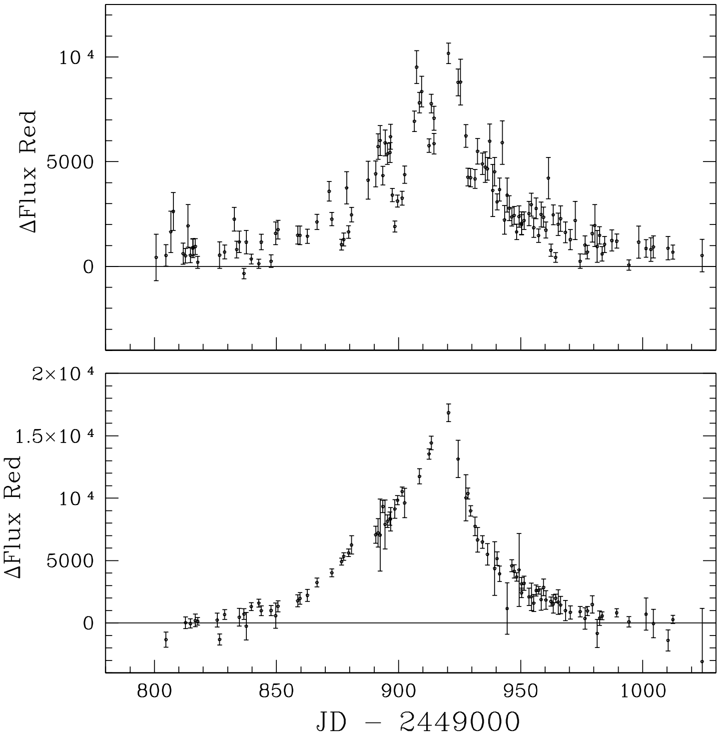

Figure 1.5: Difference between the S D P photometry (upper panel) and the DIA photometry (lower panel) shown for an exotic microlensing event. As shown on these panels the DIA method better handles the crowded stellar fields. Error bars for the DIA data points are much smaller then for S D P , and also the light curve is more smooth (Alcock et al. 2000b).

DIA software by Woźniak (2000)

The DIA version used in this thesis was written by Woźniak (2000) and consists of 15 independent modules, which can be called by a shell script (called a pipeline). A detailed description of all these modules can be found in Woźniak (2000). A short introduction is presented below. Module

- – finds the kernel and performs the subtraction of images,
- – performs rough matching of two images,

- 2 – changes output of , a database (*.db) into FITS table,
- 2 – changes float-type image (BITPIX=-32) to integer-type image (BITPIX=16),
- – finds the parameters of the point spread function,
- – searches for variable object on a series of subtracted images (output from),
- – performs simple arithmetic calculation on pixel arrays,
- – same as ,
- – co-adds images into one image (used for building reference images),
- – performs aperture and profile photometry on subtracted images,
- – resamples an image to the desired coordinates frame,
- – searches for stars on an image,
- _ – crops an image to the desired size,
- 2 – changes integer-type image (BITPIX=16) to float-type image (BITPIX=-32),
- – finds a/the polynomial transformation between two lists of coordinates/stars,
- – matches two lists of coordinates/stars using the triangle method,
- – same as .

The DIA method will be used in Chapters 2, 4 and 5.

2

Resolving blending in the microlensing surveys with the *HST*[1]

2.1 Abstract

Under typical ground-based seeing conditions, many microlensing events detected in dense stellar fields are blended. We present an analysis of the blending of seven OGLE-III microlensing events for which high-resolution images were available from the *Hubble Space Telescope* archive (in 2005). These images clearly demonstrate diverse blending conditions in microlensing events. We combine the OGLE ground-based photometry and difference image analysis astrometry with the *HST* photometry and astrometry to identify the lensed star and measure the blending parameter for each event. It is also shown that with sparse samplings, some binary events can be misidentified as single events with incorrect timescales.

---

[1] A draft paper based on Kozłowski S., Wyrzykowski Ł., Mao S., Woźniak P. R. and the OGLE collaboration (2007, in preparation).

2.2 Introduction

The microlensing optical depth in the local group is only of the order 10^{-6} (see e.g. Paczyński 1996 for a review). To maximise the numbers of microlensing events observed in an experiment, one has to monitor millions of stars in dense stellar fields, such as the Galactic bulge, Large and Small Magellanic Clouds and even M31. Fifteen years ago, there was some scepticism as to whether microlensing experiments could differentiate variable stars from microlensing events. In the last decade, such doubts have been convincingly dispelled. Several thousand microlensing events have been discovered by a number of collaborations (e.g., Udalski 2003; Woźniak et al. 2001; Sumi et al. 2003; Alcock et al. 2000b; Afonso et al. 2003a). Most of these events were discovered toward the Galactic bulge; a small number of microlensing candidates have also been identified toward the Magellanic Clouds (e.g., Alcock et al. 2000a; Afonso et al. 2003b) and M31 (e.g., Kerins and Point-Agape Collaboration 2003; de Jong et al. 2004). The large database of microlensing event toward the Galactic bulge can in principle be used for many diverse applications (e.g. Paczyński 1996). Recently, four extra solar planets were discovered using the microlensing technique (Bond et al. 2004; Udalski et al. 2005; Beaulieu et al. 2006; Gould et al. 2006). With the up-coming optical and infra-red interferometers, the two images of a source in microlensing can be resolved for bright microlensing events (Delplancke et al. 2001; Dalal and Lane 2003); this would be particularly exciting for the identification of stellar mass black holes; several such candidates have already been proposed (e.g., Mao et al. 2002; Bennett et al. 2002).

One common problem that has affected many applications of microlensing is blending, since microlensing experiments monitor dense stellar fields. Under typical ground-based seeing conditions, many stars can be blended within the seeing disk of the lensed star. In addition, the lens itself may contribute additional light (Di Stefano and Esin 1995; Buchalter et al. 1996; Kozłowski et al. 2007; Chapter 4). It is well known that blending changes the measured event duration (e.g. Alard 1997); in the most extreme cases, blending causes a degeneracy between the blending parameter, minimum impact parameter and the event duration (Woźniak and Paczyński 1997). Somewhat surprisingly, Sumi et al. (2006) showed that blending is present for faint as well as bright microlensing events. As the standard estimator of the optical depth (τ) is proportional to the timescale, blending can therefore directly affect the value of τ. It is thus important to understand blending in microlensing events.

In this chapter, we searched the *Hubble Space Telescope* (*HST*) data archive for images of the Galactic bulge fields containing microlensing events detected during the third phase of the Optical Gravitational Lensing Experiment (OGLE–III).

We identified seven events with *HST* images. Due to the superior resolution of the *HST* and the astrometry obtained from the Difference Image Analysis (DIA; e.g. Alard and Lupton 1998; Alard 2000; Woźniak 2000; Udalski 2003) method for the OGLE frames, we were able to identify the lensed star among the blends and therefore explore the effects of blending on microlensing. The chapter is organised as follows. In §2.3, we describe how we search for OGLE microlensing events coincident with *HST* pointings. The data reduction is then described. The data analysis is discussed in §2.4. In §2.5, we present fits to the light curves and derive the lensing parameters. In §2.6, we discuss our results and finish with a conclusion in §2.7.

2.3 *HST* and OGLE images and data reduction

2.3.1 Searching for OGLE microlensing events in the *HST* archive

The Early Warning System (EWS)[2] of the OGLE–III survey (Udalski 2003) discovered about 1500 microlensing events towards the Galactic bulge between 2002 and 2004. As the purpose of the EWS was mainly to identify events rapidly in real time, it had missed some events, especially in the early years of OGLE-III; the EWS is also likely to miss events with some variations in the baseline. Therefore, an independent search

---

[2] `http://ogle.astrouw.edu.pl/~ogle3/ews/ews.html`

was performed for microlensing events using an algorithm similar to the one used in Sumi et al. (2006). The catalogue will be published in the near future (Wyrzykowski, in preparation). It contains about 400 new events in addition to those identified by the EWS, giving a total of about 2000 events. Subsequently, using the coordinates of the microlensing events we searched through the *HST* archive on the website of the Space Telescope Science Institute[3] to find any images in the vicinity of our targets. In our search we selected only those images taken with the Wide Field and Planetary Camera 2 (WFPC2), the Advanced Camera for Surveys (ACS) and the Space Telescope Imaging Spectrograph (STIS) detectors.

Having the coordinates of each microlensed star, we searched for the archive *HST* observations whose centres fall within a certain radius of the star. This search radius is determined for each *HST* detector according to its field of view: WFPC2 (all chips) – $1.8'$, ACS (High Resolution Channel, HRC) – $20''$, ACS (Wide Field Channel, WFC) – $2.4'$ and STIS (CCD) – $35''$. These radii are equal to one half of the length of the diagonal of the square detectors. The probability that our target is on the CCD chip within the search radius is $2/\pi \approx 64\%$. For the WFPC2 detector, which has the famous 'L' shape, we adopt a search radius that is equal to the diagonal of one Wide Field (WF) detector, and the corresponding probability is lower, $\approx 52\%$. Within the search radii, 27 out of about 2,000 events were found in the *HST* archive, but it turned out that 17 of them were located outside the chip. After removing three events with very noisy light curves, we were left with 7 events for further blending analyses. The identified events are presented in Table 2.1 with details of the *HST* observations (name of detector, exposure time, filter and proposal ID). Note that the event BLG205.1.121022 was first discovered by the MOA collaboration as MOA-2002-BLG-33 (Abe et al. 2003).

---

[3] `http://archive.stsci.edu/hst/`

Table 2.1: Log of the *HST* archive images.

Event	OGLE ID*	Detector	Exposure	Filter	Proposal ID
OGLE-2002-BLG-178	BLG170.6.97168	ASC/WFC	600 s	F775W	9488
OGLE-2003-BLG-199	BLG163.4.131992	ASC/WFC	400 s	F775W	9984
OGLE-2003-BLG-319	BLG101.3.37299	ASC/WFC	1230 s	F658N	10009
OGLE-2003-BLG-449	BLG101.3.43456	ASC/WFC	1230 s	F658N	10009
OGLE-2004-BLG-029	BLG206.8.52366	WFPC2/WF3	700 s	F606W	10084
OGLE-2004-BLG-123	BLG346.6.131804	STIS/MIRVIS	400 s	clean	9708
MOA-2002-BLG-33	BLG205.1.121022	ASC/HRC	160 s	F814W	9691

* The OGLE–III ID of each event contains the field name, CCD chip number and star number (separated by periods).

2.3.2 *HST* and OGLE data

The basic reduction of the ACS images was done on-the-fly by the standard *HST* archive pipeline. It includes de-biasing, dark frame subtraction, flat-field correction, cosmic-ray cleaning, and combining images using the M (Koekemoer et al. 2002) and/or D software (Fruchter and Hook 2002), which were implemented in the standard pipeline since 2004. We worked with the final drizzled images. The WFPC2 and STIS images were reduced on-the-fly by the standard *HST* archive pipeline. We then used the standard IRAF (e.g. Tody 1993) tasks to remove cosmic rays, register and combine images into final images for analysis.

The OGLE data used in this chapter were collected with the 1.3 m Warsaw telescope at the Las Campanas Observatory, Chile (operated by the Carnegie Institution of Washington), equipped with a wide field CCD mosaic camera. The camera consists of eight 2048×4096 pixel SITe ST002A detectors. The pixel size of each of the detectors is 15 μm giving a 0.26 arcsec/pixel scale at the focus of the telescope. The full field of view is about $35' \times 35'$. More details on the instrumental setup of the telescope can be found in Udalski (2003).

In this chapter we use observations of the Galactic bulge collected between 2001 and 2004, i.e. almost 4 bulge seasons (OGLE-III started in mid 2001). All the observations were taken in the *I*-band filter with an exposure time of 120 seconds. The images were then preprocessed (de-biased and flat-fielded) in real time with the standard OGLE-III photometric data pipeline based on the DIA method.

Apart from the photometry, we also obtained the astrometry (centroid) of all the objects on the reference frames using D P (Schechter et al. 1993), which is based on the fitting of the point spread function (PSF). In addition, from the DIA method we obtained the true position of the microlensed star for each event. This is because the DIA subtracts off all the constant stars, and hence only the varying lensed star is left on the subtracted frame. DIA therefore allows us to measure the difference between the position of the lensed object and the centroid of the OGLE blend (see Table 2.2).

The standard magnitude system widely used is based on the *UBV* Johnson and Morgan (1953) system and *RI* Cousins (1976) system. The *HST* uses three basic magnitude systems: ABMAG, STMAG and VEGAMAG. The VEGAMAG system was designed to reflect as closely as possible the Johnson-Morgan-Cousins system (Sirianni et al. 2005). The magnitudes for Vega in all filters are by definition equal to 0 in the Vega-based system. The easiest way to calculate the instrumental *HST* magnitudes is to use header keywords from the FITS file: $photflam$ and $photzpt$, which describe the mean flux density and zero point in the STMAG system respectively. Having measured the flux (Data Numbers, DNs) in a given aperture or with the PSF photometry method, using the exposure time $t_{\rm exp}$ of an image, the magnitudes in the STMAG system can be calculated as

$$m_{\rm ST} = -2.5\ \log\left(\frac{\rm flux \times F_\lambda}{\rm t_{exp}}\right) + m_0, \tag{2.1}$$

where F_λ is the mean flux density ($photflam$) and m_0 is the zero-point ($photzpt$). It is straightforward to ‘shift’ the measured magnitudes in the STMAG system in any given filter to the VEGAMAG system magnitudes, by accounting for the zero-point in a given filter (WFPC2 – Holtzman et al. 1995, ACS – Sirianni et al. 2005). Nevertheless, magnitudes of the same object taken in the *HST* F814W filter might be slightly different from that taken in the *I*-band Cousins filter, due to different transmissions of the two filters. In order to transform the *HST* magnitudes to standard *UBVRI* magnitudes at least two images are necessary in two different filters.

The magnitudes presented in Tables 2.3 and 2.4 are in the STMAG and VEGAMAG systems, and they have not been transformed into the standard *UBVRI* system. Notice, however, that the blending parameter (the fraction of light contributed by the lensed source), f_s, is independent of the zero-points and magnitude systems and depends only on the wavelength (filter).

The magnitudes shown in Tables 2.3 and 2.4 are presented to give an indication of the brightness of the components of the OGLE blends.

2.4 Analysis

Using the task DAOFIND in IRAF, we first determined the positions of the stars on the OGLE and *HST* images. Next, for each microlensing event, we used 15 – 150 common stars from both the *HST* and OGLE images to find the transformation that matches these two frames. For simplicity, we used only a first order polynomial. Transformations with higher order polynomials did not increase the accuracy substantially, for example a second-order polynomial improved positions by less than 10% when compared with a first-order polynomial.

The stellar positions in the *HST* and OGLE frames can be matched with a RMS accuracy of $0.03''$. The uncertainties of the positions of the stars in the OGLE-III database were between $0.05''$ and $0.1''$ depending on the brightness of a star. Thus, the combined precision of the position of an OGLE star in the *HST* image is roughly $0.058''$ – $0.104''$.

Figures 2.1 and 2.2 present the OGLE and *HST* sub-frames of cross-identified bulge fields with OGLE-III microlensing events. A circle of radius $1.5''$ marks the position of each event. It is striking that each OGLE star is composed of at least two components. In order to determine exactly which *HST* stars contribute to the OGLE star, we studied the radial surface brightness profile of the OGLE star and checked whether a given star on the *HST* image has sufficient brightness and is close enough to the centroid to contribute to that blend. We only included those stars whose magnitudes are above the background magnitude in the OGLE image. Figure 2.3 shows zoomed views of the *HST* images close to the lensed stars, in which we labelled the stars contributing to the OGLE blend. The photometry of each component was performed using both the aperture photometry task PHOT and the PSF photometry task in DAOPHOT. The results are presented in Tables 2.3 and 2.4.

Three out of our seven stars were saturated on the *HST* images. We applied the following scheme to solve the problem of measuring the magnitudes of these stars and deriving the blending fractions for them and their companions. First, we derived the magnitudes of the fainter companions in the usual way. Second, we assumed that the total composite magnitude of all the stars on the *HST* image is equal to the mean I-band baseline magnitude of the OGLE star. This was a simplification as most of the *HST* observations we analysed were taken in different filters, rather than the I-band (see Table 2.1). This in principle can be repeated for the I-band magnitudes if there are more data available in the future. The magnitude of the lensed star is obtained by subtracting the other stars from the OGLE composite magnitude. The saturated stars in Tables 2.3 and 2.4 are marked by the superscript ‘2’.

We assumed that the *HST* observations were taken during the constant part of the microlensing event and the measured brightnesses corresponded to the baseline magnitudes of the lensed sources. This was true in all the events except OGLE-2004-BLG-029. The *HST* image of this event was taken on HJD = 2453059.9, just 0.8 days after the peak of the event. Thus the fact that the source was amplified during the *HST* observation had to be taken into account. We applied the same procedure used for the saturated stars (in fact the lensed star was saturated in the *HST* image) for obtaining the baseline source magnitude and the blending parameter for this event.

Subsequently, we used the information from the DIA method about the position of the lensed star and compared it to the position of the centroid of the OGLE star at the baseline. Differences between the position of the centroid of a blend and the position

Table 2.2: The equatorial coordinates (RA, Dec) of the microlensed stars and the differences in RA and Dec between the position of the centroid of the OGLE star and the position of the true microlensed star obtained from the DIA method are listed. The last column shows the error in the difference.

Name of the event	OGLE database name	RA (J2000.0)	Dec (J2000.0)	Δ RA [$''$]	Δ Dec [$''$]	Δ Error [$''$]
OGLE-2002-BLG-178	BLG170.6.97168	18:10:47.621	-31:42:29.57	0.173	-0.162	0.118
OGLE-2003-BLG-199	BLG163.4.131992	17:53:57.421	-31:33:56.74	0.051	0.005	0.078
OGLE-2003-BLG-319	BLG101.3.37299	17:54:26.665	-29:49:26.19	-0.132	-0.265	0.102
OGLE-2003-BLG-449	BLG101.3.43456	17:54:31.994	-29:48:15.97	0.095	0.089	0.097
OGLE-2004-BLG-029	BLG206.8.52366	17:58:46.000	-29:07:43.30	0.084	-0.003	0.073
OGLE-2004-BLG-123	BLG346.6.131804	17:41:44.001	-24:07:35.21	-0.057	0.014	0.072
MOA-2002-BLG-33	BLG205.1.121022	17:58:24.617	-29:06:09.72	0.014	0.080	0.077

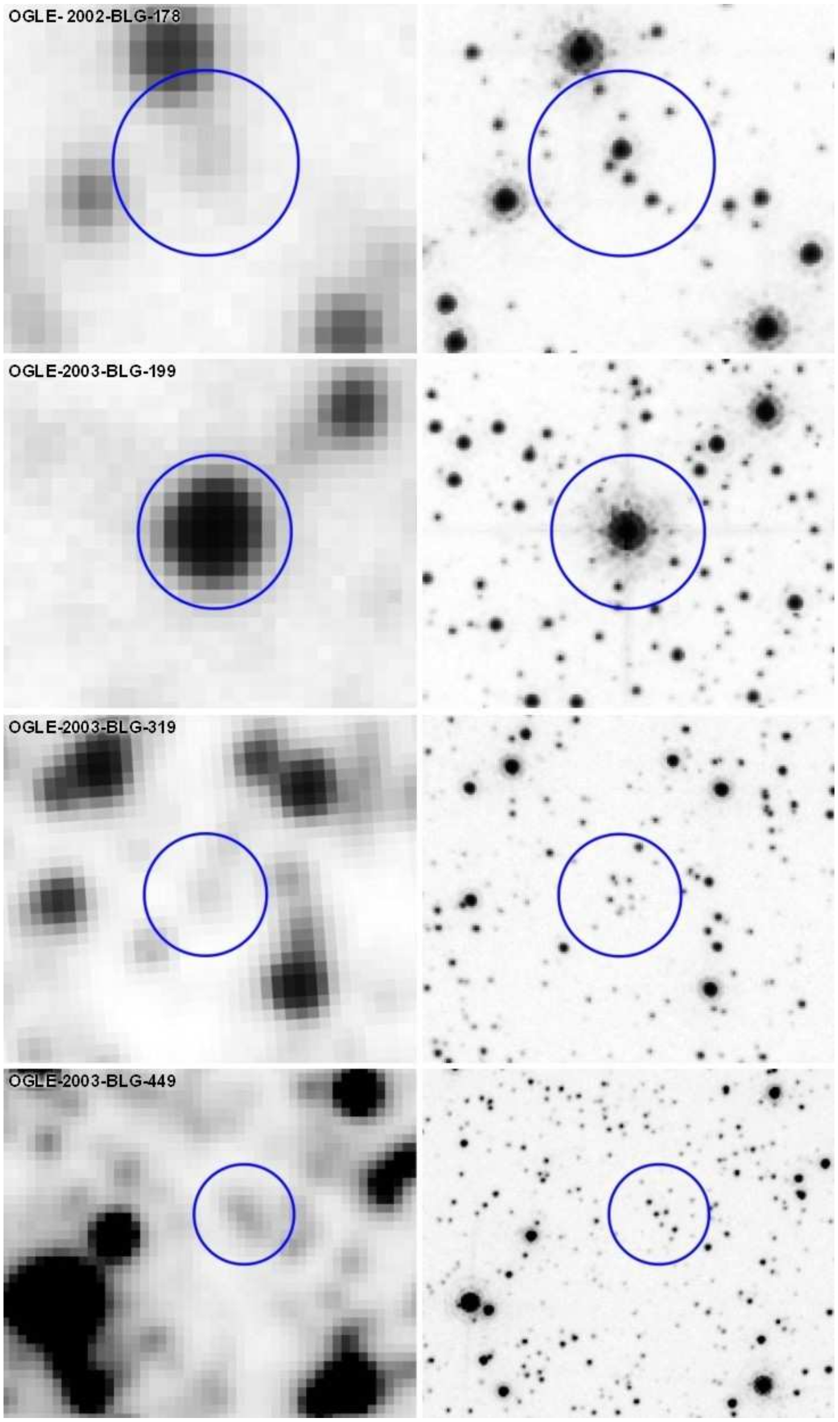

Figure 2.1: Comparison between the OGLE (left) and *HST* (right) images. The dark circle has a diameter of 3 arc seconds. From top to bottom: OGLE-2002-BLG-178, OGLE-2003-BLG-199, OGLE-2003-BLG-319 and OGLE-2003-BLG-449. North is to the right and east is up.

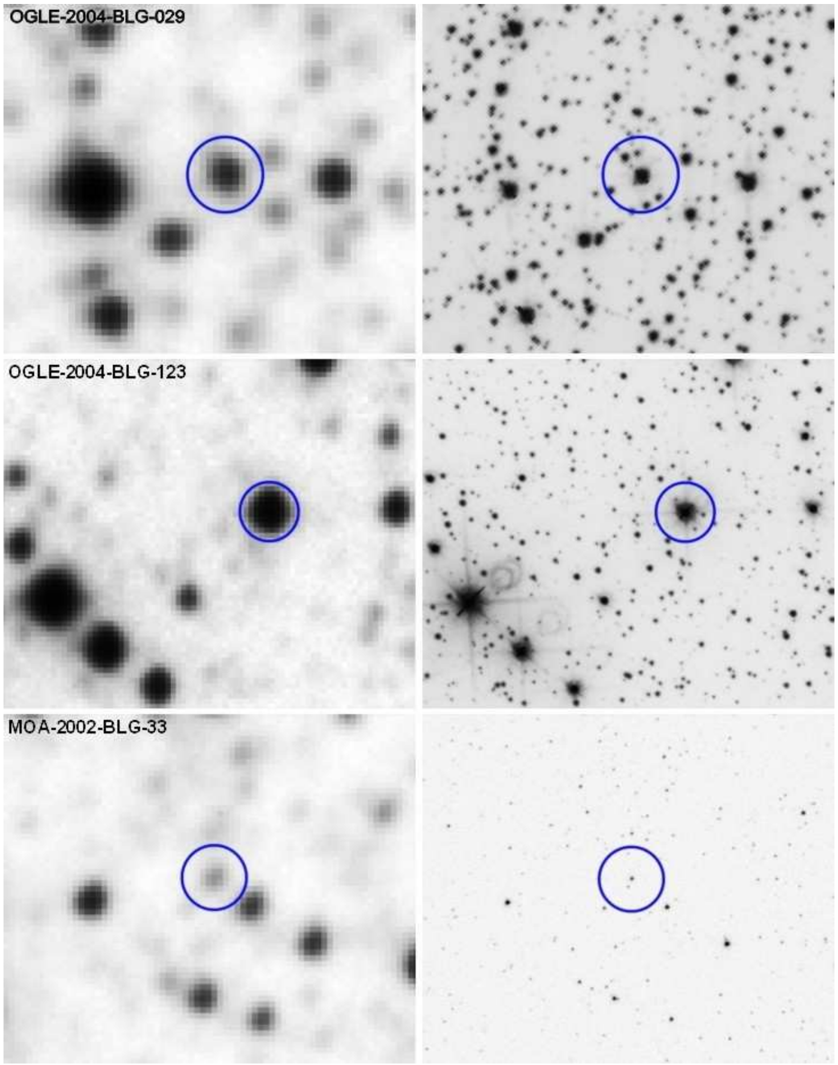

Figure 2.2: Comparison between the OGLE (left) and *HST* (right) images. The dark circle has a diameter of 3 arc seconds. From top to bottom: OGLE-2004-BLG-029, OGLE-2004-BLG-123 and MOA-2002-BLG-33. North is to the right and east is up.

of the microlensed star from DIA are shown in Table 2.2. Applying these differences in our analyses we identified the lensed star in the *HST* image for each microlensing event. The positions of the centroid of the OGLE star and the microlensed star are marked with crosses in each panel of Figure 2.3. If there is no cross marked, it means that the difference between the position of the centroid of the OGLE star and the position of the lensed object was smaller than the measurement error. This implies that the brightest

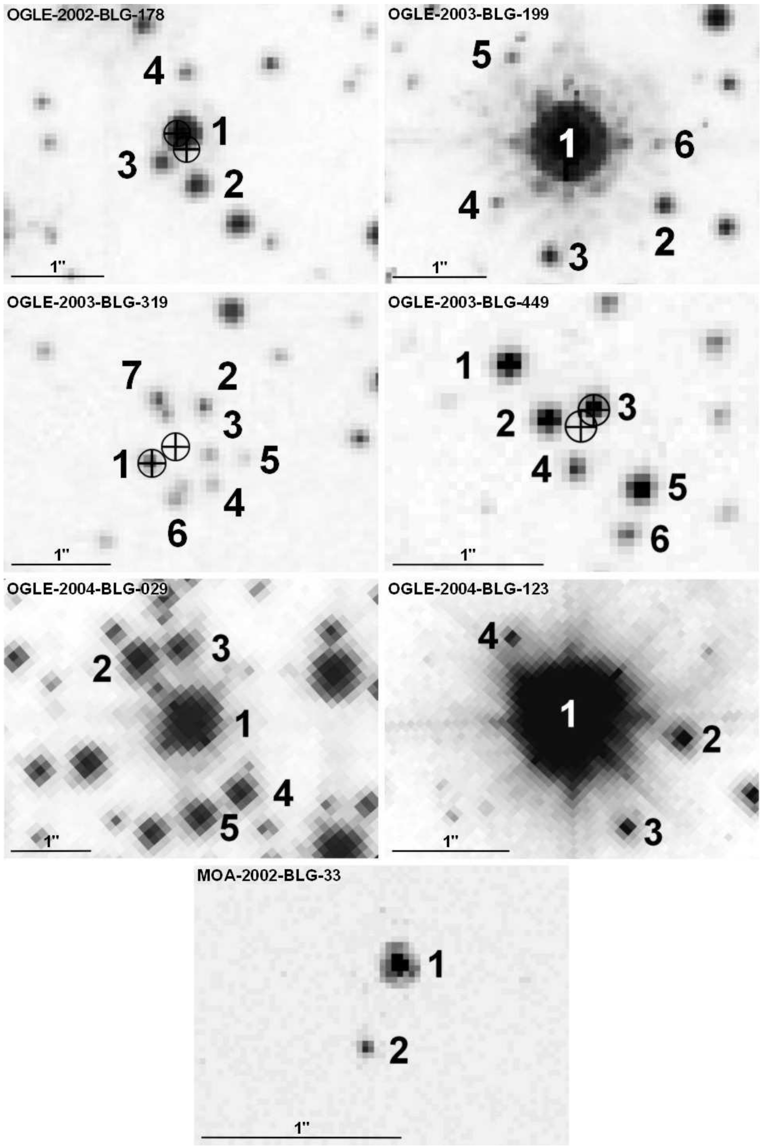

Figure 2.3: The components of stars OGLE-2002-BLG-178, OGLE-2003-BLG-199, OGLE-2003-BLG-319, OGLE-2003-BLG-449, OGLE-2004-BLG-029, OGLE-2004-BLG-123 and MOA-2002-BLG-33 are shown. These are close-ups from the *HST* images. Dark crosses mark the positions of the centroids of the components of a blend and the position of the microlensed star in this blend taken from DIA. The cross over a star on the image indicates the microlensed star. If there is no cross shown it means that the brightest star on the image was microlensed and the difference in the positions was much smaller than the uncertainty of the star's position. The sizes of the crosses indicate the uncertainties of the positions. North is to the right and east is up.

star was lensed. The size of the cross indicates the uncertainty of the measured position (of the centroid) of the OGLE star/the *HST* lensed star. In Tables 2.3 and 2.4, each identified lensed star is marked in bold.

2.5 Microlensing parameters from photometry and astrometry

Using the OGLE-III data we performed fitting of the light curves of the events with the standard model (e.g., Paczyński 1986; Smith et al. 2002), which is characterised by five parameters: the baseline magnitude I_{base}, the Einstein radius crossing time t_{E}, the time when the peak magnification is reached t_{peak}, the minimum impact parameter u_0, and the blending parameter f_{s}, which is the fraction of light contributed by the lensed star ($f_{\mathrm{s}} = 1$ if there is no blending).

The best-fit parameters are found by the standard χ^2 minimisation procedure using the MINUIT routine (§1.4.5). Figure 2.4 shows the best fits together with the data points. The best-fit parameters are presented in Table 2.5. Below we discuss each event in turn.

Notice that most of the *HST* observations were taken in different filters than the OGLE observations (Table 2.1). The OGLE *I*-band filter centres around 800nm, while this is similar to the F814W filter (centred around 806nm), it is significantly different from the F658N and F608W filters (centred around 658nm and 592nm respectively). The difference in the filters makes it difficult to compare the blending parameters obtained from the *HST* images and from the light curve fitting if the colours of the lensed star and the blends are different.

For OGLE-2002-BLG-178, the standard model fits the data well, but the blending fraction and timescale are not well-constrained. When the blending fraction is fixed to the observed value in the F775W filter ($f_{\mathrm{s}} = 0.784$), χ^2 becomes slightly worse (with $\Delta\chi^2 = 0.5$) than the best-fit χ^2 when f_{s} is allowed to vary freely. As the latter model

Table 2.3: Magnitudes and the fraction of light contributed by the stars.

Name (*HST* filter)		1	2	3	4	5	6	7	**sum**
OGLE-2002-BLG-178	ST mag	**20.207**	22.325	22.727	23.880	—	—	—	**19.943**
(F775W)	VEGA mag	**19.070**	21.188	21.590	22.743	—	—	—	**18.806**
	mag err	**0.004**	0.017	0.041	0.110	—	—	—	—
	$f_{\rm s}$	**0.784**	0.111	0.078	0.027	—	—	—	**1.000**
OGLE-2003-BLG-199	ST mag	**—**[2]	22.216	22.062	23.271	23.227	23.192	—	**—**[2]
(F775W)	VEGA mag	**14.786**[2]	21.079	20.925	22.134	22.090	22.055	—	**14.775**[2]
	mag err	**0.003**	0.040	0.026	0.119	0.109	0.091	—	**0.003**
	$f_{\rm s}$	**0.990**	0.003	0.004	0.001	0.001	0.001	—	**1.000**
OGLE-2003-BLG-319	ST mag	**21.445**	21.767	22.295	22.483	23.167	21.710[1]	21.233[1]	**19.745**
(F658N)	VEGA mag	**20.662**	20.984	21.512	21.700	22.384	20.927[1]	20.450[1]	**18.962**
	mag err	**0.076**	0.106	0.186	0.211	0.408	0.092[1]	0.067[1]	—
	$f_{\rm s}$	**0.209**	0.155	0.095	0.080	0.043	0.164[1]	0.254[1]	**1.000**
OGLE-2003-BLG-449	ST mag	20.846	20.876	**21.177**	21.807	20.789	22.076	—	**19.214**
(F685N)	VEGA mag	20.063	20.093	**20.394**	21.024	20.006	21.293	—	**18.431**
	mag err	0.030	0.031	**0.044**	0.076	0.031	0.105	—	—
	$f_{\rm s}$	0.226	0.219	**0.164**	0.092	0.230	0.070	—	**1.000**

[1] on the *HST* image this star is a blend of two stars.

[2] the star on the *HST* image is saturated; we adopted the OGLE *I*-band magnitude as the total magnitude of the composite, and then calculated the fraction of light contributed by each star to the blend (see the text).

Table 2.4: Magnitudes and the fraction of light contributed by the stars (continuation of Table 2.3).

Name (*HST* filter)		1	2	3	4	5	6	7	**sum**
OGLE-2004-BLG-029	ST mag	**—** [3]	19.674	20.649	20.195	20.448	—	—	**—** [3]
(F606W)	VEGA mag	**15.551**[3]	19.360	20.335	19.881	20.134	—	—	**15.472**[3]
	mag err	**0.003**	0.005	0.011	0.007	0.009	—	—	**0.003**
	f_s	**0.934**	0.026	0.011	0.016	0.013	—	—	**1.000**
OGLE-2004-BLG-123	ST mag	**14.412**[2]	22.018	22.629	22.622	—	—	—	**14.410**[2]
(CLEAN)	mag err	**0.003**	0.015	0.025	0.023	—	—	—	**0.003**
	f_s	**0.9985**	0.0009	0.0005	0.0005	—	—	—	**1.000**
MOA-2002-BLG-33	ST I mag	**18.532**	20.572	—	—	—	—	—	**18.382**
(F814W)	VEGA I mag	**17.243**	20.572	—	—	—	—	—	**17.090**
	mag err	**0.023**	0.060	—	—	—	—	—	—
	f_s	**0.871**	0.129	—	—	—	—	—	**1.000**

[2] the star on the *HST* image is saturated; we adopted the OGLE *I*-band magnitude as the total magnitude of the composite, and then calculated the fraction of light contributed by each star to the blend (see the text).

[3] the *HST* image was taken when the event was close to the peak of the event; the magnitude and the blending fraction shown correspond to the baseline.

(when f_s is free) has one more parameter, the difference in χ^2 is not significant.

OGLE-2003-BLG-199 is a very bright event, with a baseline magnitude of $I \approx 14.8$. The lensed star clearly dominates the light in the *HST* image and its blending parameter is nearly 1 ($f_s = 0.990$). Unfortunately, the light curve fitting did not converge and thus we fixed the f_s parameter to be unity. $\chi^2 = 433.9$ for 219 degrees of freedom, indicating that the error bars may be under-estimated, which is often the case for very bright stars in the OGLE *I*-band photometry (a similar trend was seen in the OGLE–I photometry, Udalski et al. 1994c).

OGLE-2003-BLG-319 has a composite magnitude of $I = 18.47$. When f_s is allowed to vary, the fitted timescale and the blending parameter have uncertainties of about 20% and 30%, respectively. The blending parameter in the OGLE *I*-band agrees with the value ($f_s = 0.209$) determined from the F658N filter *HST* image to within 1σ. When the blending parameter is fixed to this value, the best-fit χ^2 increases by only 0.2, while the fitted timescale decreases by about 10% (but still within the 1σ error bar of the f_s value when it is allowed to vary freely).

The blending parameter for the next event, OGLE-2003-BLG-449, is well constrained from the light curve fit ($f_s = 0.567 \pm 0.145$), however the sampling of the light curve is rather sparse. The total $\chi^2 = 1796.3$ for 366 degrees of freedom. The large χ^2 per degree of freedom is likely due to a combination of some source variability and an under-estimate of the error bars. However, our analysis of the *HST* image reveals that the lensed source contributed only 16.4% of the total light in the F658W fitler. When f_s is fixed to 0.164, the best-fit model has $\chi^2 = 1821.8$, significantly worse than the original fit ($\Delta\chi^2 \approx 25.5$). The difference in the obtained values of f_s is relatively large. This difference in the blending fraction may be because measurements are made in different filters (F658W for the *HST* vs. *I*-band for the OGLE) and the lensed star and the blended stars have different colours. Another possible explanation of this discrepancy is intrinsic variability of the source, which can be seen in the noisy baseline of this event. Unfortunately, it is currently impossible to distinguish these two possibilities; more detailed investigations (e.g. multi-colour *HST* observations) are required to resolve this issue.

OGLE-2004-BLG-029 is a bright event, with a baseline magnitude of $I = 15.47$. The *HST* observations of this event were taken almost at the moment of the maximum amplification, which was taken into account as described above (see §2.4). It is clearly seen in Figure 2.2 that the lensed star is blended with many nearby companions. The standard fit cannot converge to a blending parameter when it is allowed to vary freely, so we fixed $f_{\rm s}$ to 1. The best-fit model has $\chi^2 = 2020.9$ for 296 degrees of freedom. If we fix the blending parameter to 0.934, as determined from the F606W filter on the *HST* image after correcting for the magnification, χ^2 changes slightly (from 2020.9 to 2021.1). Both fits have a large χ^2, probably reflecting an under-estimate of the error bars in the I-band OGLE photometry, and/or some intrinsic variability of the lensed source or one (or more) of the components of the blend.

OGLE-2004-BLG-123 is the brightest of the seven microlensing events, with a baseline magnitude of 14.41. From the *HST* image, it is clear that the lensed star dominates the total blended light – it contributes $\approx 99.9\%$ of the total light of the OGLE blend. The standard fit again could not converge, so we fixed the blending parameter $f_{\rm s} = 1$. In this case, the fit parameters stay virtually the same if we adopt $f_{\rm s} = 0.999$, the value determined from the photometry of the *HST* image.

The event MOA-2002-BLG-33 was first discovered by the MOA collaboration. It reached a peak magnification as high as 450 and was used to constrain the source limb-darkening profile (Abe et al. 2003) and the ellipticity of the source star (Rattenbury et al. 2005). However, the peak of magnification was not observed by OGLE, so there are no signatures of the binarity of the lens as seen by MOA. In fact, the OGLE data alone can be reasonably well fitted with the standard model with a $\chi^2 = 479.7$ for 226 degrees of freedom. In this fit the blending parameter is well constrained with a value of $f_{\rm s} = 0.557 \pm 0.010$. However, the $f_{\rm s}$ value determined from the *HST* image ($f_{\rm s} = 0.871$) differs significantly. We emphasise that for this event, the OGLE and *HST* filters are very similar, so their blending fractions can be directly compared. When we fixed the blending parameter to this empirically determined value, the best-fit model has a much worse χ^2 of 1186.9 for 227 degrees of freedom, indicating that we are using the wrong model as it cannot match the data points in the lensed part of the light curve. This event highlights the fact that with sparse sampling, some events apparently well fitted by the standard single lens model can in fact have more complex origins.

2.6 Discussion

High resolution *HST* observations revealed that the OGLE microlensed stars are usually composed of at least two or more components. For the seven events we examined, there seems to be an important difference between the bright and faint events. The bright OGLE stars consist of one dominating bright star and numerous dimmer components, where the brightness ratio between the bright and the faint components is at least 10:1. On the other hand, the fainter OGLE stars consist of a few components with comparable brightness. In our sample, stars brighter than $I = 15$ mag usually contribute more than 90% of the light to the OGLE microlensed blend. But this may not be true in general. Dim components of the bright composite may also be microlensed, but they require much higher amplification to be detected. Real examples are known: in the OGLE-II binary lensing event SC5_6550, with a baseline magnitude of $I = 16.18$, the lensed star contributed only 1% of the total light (Jaroszyński 2002). Recently, Sumi et al. (2006) simulated a dense bulge field using the Baade's Window luminosity function and checked the blending distribution as observed in the OGLE–II survey. They found that for bright events the fraction of the Red Clump Giant stars blended with fainter components is ~38%. Virtually every faint star of $I \geq 17$ is a member of some blend.

Another important issue is the comparison of the blending parameter obtained from the light curve fitting and that measured from the *HST* image. A problem we encountered was that for the three bright events there is a strong degeneracy in the model and we were unable to determine the blending parameters reliably. They were therefore fixed to $f_{\rm s} = 1$, which turned out to be close to the values measured from the

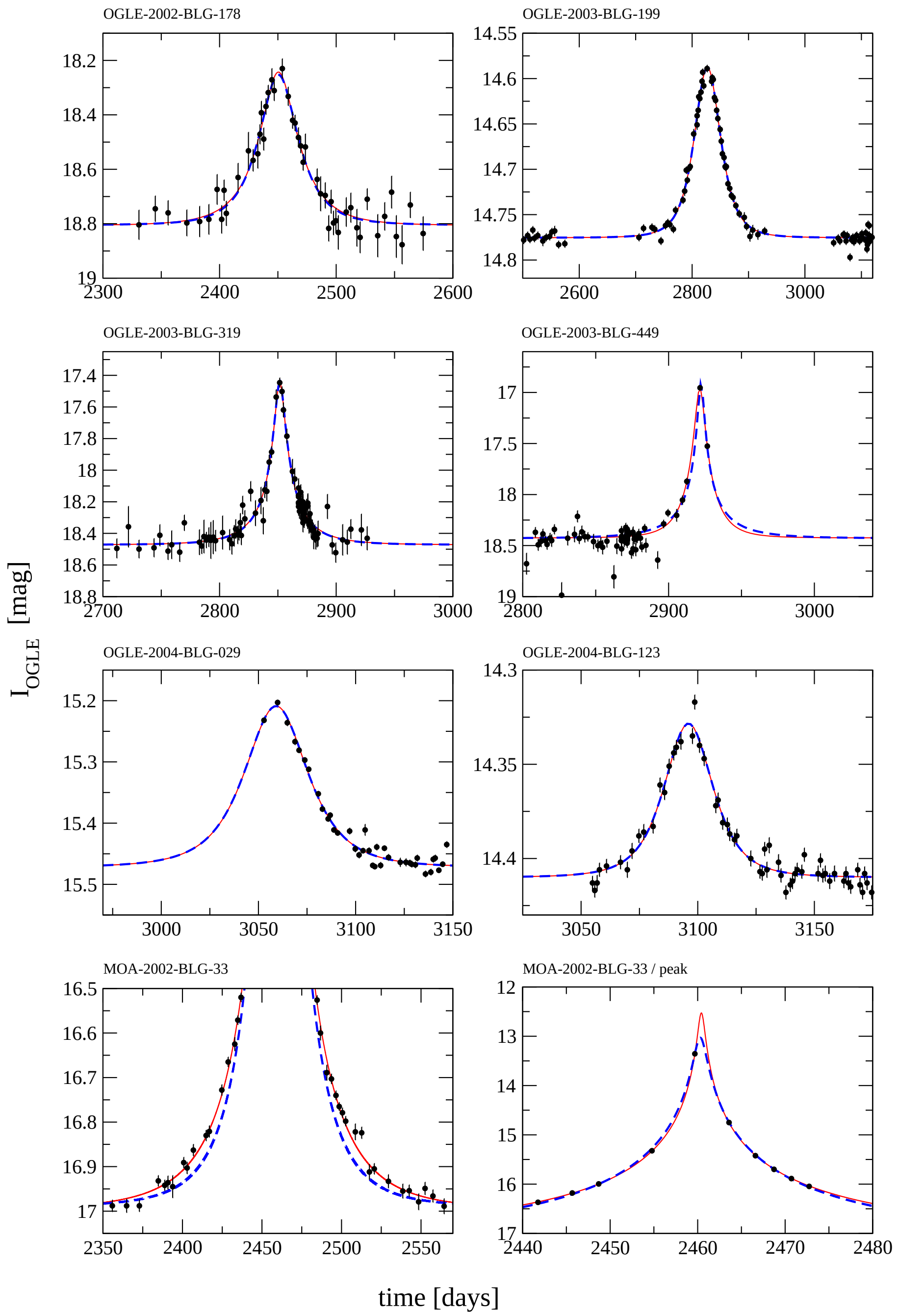

Figure 2.4: Light curves for the events. Only the lensed portions of the light curves are shown. The event MOA-2002-BLG-33 (two bottom panels) is a binary event, but the OGLE data can be fitted reasonably well with a single light curve. The dashed line shows the best fit with fixed blending parameter, the solid line shows the best fit with free (or fixed to 1; see Tables 2.3 and 2.4) blending parameter.

Table 2.5: Fit parameters for the seven microlensing events. Error equal to 0 means the parameter value was fixed.

Event	BF[1]	t_{peak}	t_{E}	u_{min}	I_{base}	f_{s}	χ^2/dof
OGLE-2002-BLG-178	N	2450.4 (0.5)	34.932 (12.409)	0.410 (0.221)	18.806 (0.007)	0.428 (0.317)	118.6 / 106
OGLE-2002-BLG-178	Y	2450.4 (0.5)	26.891 (1.365)	0.616 (0.017)	18.805 (0.006)	0.784 (0)	119.1 / 107
OGLE-2003-BLG-199	Y[2]	2827.2 (0.2)	23.955 (0.239)	1.303 (0.005)	14.775 (0.001)	1.000 (0)[2]	433.9 / 219
OGLE-2003-BLG-199	Y	2827.2 (0.2)	24.025 (0.240)	1.298 (0.004)	14.775 (0.001)	0.990 (0)	433.9 / 219
OGLE-2003-BLG-319	N	2851.6 (0.2)	41.459 (8.359)	0.103 (0.029)	18.472 (0.004)	0.182 (0.054)	663.5 / 390
OGLE-2003-BLG-319	Y	2851.6 (0.2)	37.874 (0.952)	0.117 (0.003)	18.472 (0.004)	0.209 (0)	663.7 / 391
OGLE-2003-BLG-449	N	2921.5 (0.2)	18.897 (3.023)	0.166 (0.037)	18.425 (0.003)	0.567 (0.145)	1796.3 / 366
OGLE-2003-BLG-449	Y	2922.2 (0.2)	41.736 (1.401)	0.051 (0.002)	18.429 (0.003)	0.164 (0)	1821.8 / 367
OGLE-2004-BLG-029	Y[2]	3059.1 (0.5)	18.487 (0.307)	1.107 (0.005)	15.472 (0.001)	1.000 (0)[2]	2020.9 / 296
OGLE-2004-BLG-029	Y	3059.1 (0.3)	18.856 (0.312)	1.0729 (0.005)	15.472 (0.001)	0.934 (0)	2021.1 / 296
OGLE-2004-BLG-123	Y[2]	3096.1 (0.3)	8.544 (0.228)	1.831 (0.015)	14.410 (0.001)	1.000(0)[2]	438.3 / 191
OGLE-2004-BLG-123	Y	3096.1 (0.3)	8.548 (0.229)	1.830 (0.015)	14.410 (0.001)	0.999(0)	438.3 / 191
MOA-2002-BLG-33[3]	N	2460.4 (0.0)	42.394 (0.621)	0.009 (0.001)	16.997 (0.001)	0.557 (0.010)	479.7 / 226
MOA-2002-BLG-33[3]	Y	2460.3 (0.0)	29.886 (0.066)	0.023 (0.001)	16.991 (0.001)	0.871 (0)	1186.9 / 227

[1] BF – blending fixed: Y – yes, N – no.

[2] The fitting program did not converge for the blending parameter, so the f_{s} parameter was fixed to 1.

[3] This microlensing event was a binary event, nevertheless we fitted the light curve with a point mass lens model.

HST images. For the four remaining events we were able to determine the value of f_s. For the event MOA-2002-BLG-33, both the OGLE and *HST* observations were taken in I-band. Nevertheless, the blending fraction obtained from the standard model is significantly different from that obtained from the *HST* images. It turns out that the difference arises because the event was a binary lensing event, a fact not readily seen with the OGLE sampling. The behaviour of another event, OGLE-2003-BLG-449, may be affected by some intrinsic variability of the lensed source or one of the blend components, in any case the light curve of the event is sampled very sparsely. Nevertheless, the fitted f_s value agrees within 3σ with that determined from the *HST* image photometry.

In general, the better the coverage of a light curve, the better the agreement for the f_s values we found from the *HST* images and light curve modelling. This is an encouraging result as the vast majority of OGLE events have no coincident *HST* images, and therefore it is re-assuring to confirm that for a densely sampled light curve the blending fractions obtained from light curve modelling alone are reasonably reliable.

The true position of the lensed star is obtained by comparing the *HST* images and the lensed star position obtained from the DIA. For most events, no such *HST* images are available, nevertheless it is still possible to gain some information about the position of the lensed star by examining the OGLE images using DIA method. This is easily seen on the *HST* images (Figure 2.3) – the position of the microlensed star found by the DIA method agrees very well with the position of the lensed star identified in the *HST* image. Without the *HST* images, analysis of the OGLE images using the DIA method offers an alternative for studying the blending in microlensing events. In particular, if the lensed star is faint and there is an astrometric offset between the lensed star and the blend, then the offset can be most easily detected with the centroid motions (Sumi et al. 2006).

2.7 Conclusions

In this chapter, we have studied seven microlensing events that have both *HST* images and ground-based OGLE-III photometry. We found that blending is present in all seven cases, confirming the conclusion of Sumi et al. (2006) that blending cannot be neglected even for bright sources. For events with a converged single lens model, there is reasonably good agreement between the fitted blending parameter and the measured value from the *HST* high-resolution images. We also demonstrated the advantages of the DIA method applied to ground-based observations, as it can provide additional information about the blending.

The event MOA-2002-BLG-33 should serve as a clear warning. It shows that although an event may be reasonably described by the standard model with a well determined blending parameter, its true nature may be more complex (e.g. it could be due to a close binary). It would be interesting to find out the fraction of such events in the lensing surveys, as an accurate determination of the optical depth should account for such events.

As the number of microlensing events increases by ~500 per year, there will be more and more microlensing events with coincident archive *HST* images. It will be interesting to repeat studies such as this one in the future.

Acknowledgments

We thank Prof. Bohdan Paczyński for helpful comments.

3

HST proper motions in the Galactic centre [1]

3.1 Abstract

We present a proper motion mini-survey of 35 fields in the vicinity of Baade's Window, $(l, b) = (1^\circ, -4^\circ)$, sampling roughly a $5^\circ \times 2.5^\circ$ region of the Galactic bar. Our second-epoch observations collected with the ACS/HRC instrument on board the *Hubble Space Telescope* were combined with the archival WFPC2/PC images. The resulting time baselines are in the range of 4 – 8 years. Precise proper motions of 15,863 stars were determined in the reference frame defined by the mean motion of stars with magnitudes in the range $I_{F814W} = 16.5 - 21.5$ along the line of sight. We clearly detect small gradients in proper motion dispersions $(\sigma_{\rm l}, \sigma_{\rm b}) \approx (3.0, 2.5)$ mas yr^{-1}, and in the amount of anisotropy ($\sigma_{\rm l}/\sigma_{\rm b} \approx 1.2$). Both the longitude dispersion $\sigma_{\rm l}$ and its ratio to the vertical motion $\sigma_{\rm b}$ increase toward the Galactic plane. The decline of the anisotropy ratio $\sigma_{\rm l}/\sigma_{\rm b}$ toward the minor axis of the bulge is mostly due to increasing $\sigma_{\rm b}$. We also find, for the first time, a significant negative covariance term in the transverse velocity field $\sigma_{\rm lb}/(\sigma_{\rm l}\sigma_{\rm b}) \approx -0.10$. Our results extend by a factor of ~15 the

---

[1] The work presented in this chapter has been published as Kozłowski S., Woźniak P. R., Mao S., Smith M. C., Sumi T., Vestrand W. T., Wyrzykowski Ł., 2006, MNRAS, 370, 435.

number of the Galactic bar fields with good proper motion dispersions.

3.2 Introduction

The Milky Way appears to be a typical spiral galaxy with a disk and bulge (§1.1). While our unique inside view of the Galaxy helps to understand the galactic structure in general, it also tends to hide the forest behind the trees. The case for existence of the Galactic bar – first proposed by de Vaucouleurs et al. (1964) – is easier to make knowing that bars are common in external galaxies.

There is now conclusive evidence that the Galactic bulge is of a barred type. The longitude asymmetry of the *COBE* photometric maps (Blitz and Spergel 1991; Dwek et al. 1995), high optical depths to gravitational microlensing (e.g. Zhao et al. 1995), asymmetric star counts (Stanek et al. 1994; Babusiaux and Gilmore 2005), non-circular gas kinematics (de Vaucouleurs et al. 1964), and triaxiality of the stellar velocity field (Zhao et al. 1994, 1996) have all been interpreted as signatures of the Galactic bar. Unfortunately, the size and precise orientation of the bar are still being debated. Recently Benjamin et al. (2005) found that the infra-red star counts collected by the *Spitzer Space Telescope* are best explained assuming a bar with a half-length of 4.4 ± 0.5 kpc placed at a $\sim 44^\circ$ angle to the Sun–Galactic centre line. Most previous studies prefer a bar at $\sim 25^\circ$ extending out to ~ 3.5 kpc in length (e.g. Gerhard 2001; Rattenbury et al. 2007b). Such apparently conflicting evidence may be an indication that the inner Galaxy hides even more complicated structures. A secondary bar (Alard 2001; Babusiaux and Gilmore 2005) and a ring (Sevenster and Kalnajs 2001) have been suggested, since these features are also evident in many other spiral galaxies (e.g. Erwin and Sparke 1999).

Binney (2005) discussed the progress of the dynamical modelling techniques in the context of major observational advances expected from the future space mission *GAIA*. The two dominant approaches to construct self-consistent dynamical Galaxy models are the Schwarzschild method (Zhao et al. 1994; Häfner et al. 2000) and N-body simulations with particle weights determined by the Syer and Tremaine (1996) ‘made-to-measure’ algorithm. The first Galactic bar model employing the latter method was built by Bissantz et al. (2004). Neither of these techniques can fully address the structure of the inner Galaxy without constraints on stellar kinematics. The refinement of the models is limited largely by the scarcity of good proper motion and radial velocity measurements. Bissantz et al. (2004), for example, compared kinematic predictions of their model with the data for just two lines of sight. A handful of samples published since the pioneering photographic work of Spaenhauer et al. (1992) is not enough to remove the non-uniqueness of the model parameters.

In a study based on two lines of sight Kuijken and Rich (2002) demonstrated that high-quality relative proper motions can be obtained with a relatively modest investment of time using the *Hubble Space Telescope* (*HST*). At the resolution of the Wide Field Planetary Camera 2 (WFPC2) instrument the required time baseline is only a few years. The *HST* archive contains a number of images suitable as the first-epoch data, so the tedious part of accumulating the baseline can be avoided entirely. Most of these serendipitous fields are centred around microlensing events discovered by the MACHO collaboration (e.g. Popowski et al. 2005). Using a similar concept, we carried out a mini-survey of proper motions in 35 of the available MACHO fields to study the kinematics of microlensed sources. Here we present the measurement techniques and results for the general stellar population along these 35 lines of sight.

3.3 *HST* images and data reduction

The log of the *HST* observations used in our proper motion mini-survey is given in Tables 3.1 and 3.2. The first-epoch images (selected from the *HST* archive[2]) were all taken with the WFPC2/PC camera, and cover the time interval 1996–2000. The second-epoch data come from our own SNAP program (cycle 13; proposal ID 10198) and were collected in 2004 and 2005 using the High Resolution Channel (HRC) of

---

[2] `http://archive.stsci.edu/hst/`

Table 3.1: The *HST* proper motion mini-survey: data.

			First epoch				Second epoch	
MACHO field	RA	Dec	Year	F814W exp.	F555W exp.	Prop. ID	Year	F814W exp.
108-C	18:00:01.276	−28:27:41.23	1996.82	6 × 260 s	....	6756	2005.16	4 × 260 s
119-C	18:03:03.010	−30:09:56.50	1996.82	6 × 260 s	....	6756	2005.15	4 × 260 s
119-D	18:04:24.825	−30:05:58.94	1996.82	6 × 260 s	....	6756	2004.78	4 × 260 s
120-A	18:07:26.441	−29:39:34.22	1996.82	6 × 260 s	....	6756	2005.15	4 × 260 s
167-A	18:13:32.154	−26:31:10.33	1996.82	6 × 260 s	....	6756	2005.16	4 × 260 s
101-C	18:07:32.649	−27:31:35.60	1997.47	6 × 260 s	....	6756	2005.15	4 × 260 s
95-BLG-11 ..	18:04:37.239	−30:12:11.45	1996.67	6 × 260 s	....	6756	2005.16	4 × 260 s
96-BLG-17 ..	18:06:09.107	−27:53:38.59	1996.81	6 × 260 s	....	6756	2005.17	4 × 260 s
119-A	18:03:35.789	−29:42:01.26	1996.68	6 × 160 s	2 × 400 s	6756	2005.14	4 × 160 s
95-BLG-7 ...	18:13:29.298	−26:13:58.12	1998.84	2 × 40 s	3 × 40 s	7431	2005.46	4 × 40 s
95-BLG-10 ..	17:58:16.011	−29:32:10.86	1997.82	2 × 40 s	3 × 40 s	7431	2004.66	4 × 40 s
95-BLG-13 ..	18:08:47.038	−27:40:47.25	1999.45	2 × 40 s	3 × 40 s	7431	2005.12	4 × 40 s
95-BLG-14 ..	18:01:26.308	−28:31:14.03	2000.45	2 × 40 s	3 × 40 s	7431	2005.40	4 × 40 s
95-BLG-19 ..	18:11:32.487	−27:45:26.99	1998.49	2 × 40 s	3 × 40 s	7431	2005.44	4 × 40 s
97-BLG-18 ..	18:03:15.254	−28:00:14.06	1998.59	2 × 40 s	3 × 40 s	7431	2005.31	4 × 40 s
104-C	18:03:34.050	−28:00:18.94	1998.73	2 × 40 s	3 × 40 s	7431	2005.43	4 × 40 s
104-D	18:03:29.024	−28:00:30.99	1998.80	2 × 40 s	3 × 40 s	7431	2005.45	4 × 40 s
108-A	18:00:25.866	−28:02:35.24	1998.80	2 × 40 s	3 × 40 s	7431	2005.16	4 × 40 s

Table 3.2: The *HST* proper motion mini-survey: data (continuation of Table 3.1).

			First epoch				Second epoch	
MACHO field	RA	Dec	Year	F814W exp.	F555W exp.	Prop. ID	Year	F814W exp.
128-B	18:07:18.624	−28:59:29.83	1998.49	2 × 30 s	3 × 40 s	7431	2005.37	4 × 30 s
104-B	18:03:09.046	−28:01:45.25	1999.45	2 × 40 s	3 × 40 s	7431	2005.39	4 × 40 s
128-A	18:06:57.621	−29:00:55.15	1999.33	2 × 40 s	3 × 40 s	7431	2005.49	4 × 40 s
94-BLG-3	17:58:25.300	−29:47:59.50	1997.82	2 × 40 s	3 × 40 s	7431	2005.48	4 × 40 s
94-BLG-4	17:58:36.766	−30:02:19.27	1997.82	2 × 40 s	3 × 40 s	7431	2005.16	4 × 40 s
95-BLG-36	18:07:20.775	−27:24:09.69	1998.80	2 × 40 s	3 × 40 s	7431	2005.39	4 × 40 s
95-BLG-37	18:04:34.452	−28:25:33.46	1999.43	2 × 40 s	3 × 40 s	7431	2004.67	4 × 40 s
95-BLG-38	17:59:41.851	−28:12:10.31	1998.81	2 × 40 s	3 × 40 s	7431	2005.33	4 × 40 s
95-BLG-41	18:02:06.332	−28:50:45.26	1999.46	2 × 40 s	3 × 40 s	7431	2005.44	4 × 40 s
96-BLG-14	18:05:15.421	−27:58:25.01	1997.83	2 × 40 s	3 × 40 s	7431	2004.67	4 × 40 s
96-BLG-4	18:06:11.954	−28:16:52.77	1998.79	2 × 26 s	3 × 40 s	7431	2004.82	4 × 26 s
97-BLG-38	18:04:06.083	−27:48:26.25	1998.51	2 × 40 s	3 × 40 s	7431	2004.63	4 × 40 s
97-BLG-24	18:04:20.253	−27:24:45.28	1998.35	2 × 40 s	3 × 40 s	7431	2005.49	4 × 40 s
96-BLG-5	18:05:02.497	−27:42:17.23	1999.45	4 × 160 s	2 × 400 s	8490	2005.12	4 × 160 s
98-BLG-6	17:57:32.812	−28:42:45.41	2000.48	2 × 100 s	2 × 260 s	8654	2004.73	4 × 100 s
97-BLG-41	17:56:20.691	−28:47:41.97	2000.47	4 × 100 s	4 × 160 s	8654	2004.62	4 × 100 s
99-BLG-22	18:05:05.281	−28:34:41.69	2001.77	4 × 400 s	4 × 400 s	9307	2005.16	4 × 400 s

the Advanced Camera for Surveys (ACS). Our SNAP survey was optimized toward high execution rates and, therefore, we only requested F814W observations to keep the required target visibility as low as possible. Both PC and HRC detectors cover a similar field of view ($25'' \times 29''$ and $35'' \times 35''$, respectively) and have different pixel scales (27 versus 45.5 mas). There were no restrictions on the telescope roll angle during ACS observing. While the latter relaxed condition decreased the number of possible proper motion determinations, it greatly improved scheduling opportunities. Most of the subsequent analysis for each of the 35 fields is based on a pair of good-quality F814W (*I*-band) images constructed by stacking all suitable data for a given epoch. In some cases, the first-epoch data included F555W (*V*-band) images that allowed us to construct colour-magnitude diagrams (CMDs). We also re-analysed two additional fields previously studied by Kuijken and Rich (2002), increasing to 37 the total number of Galactic bulge fields considered here.

3.3.1 Image reductions

The basic reductions of the ACS images, i.e. de-biasing, dark frame subtraction, flat-fielding, and cosmic-ray removal, were performed on-the-fly by the standard *HST* data processing pipeline. The pipeline also takes care of dithering, cosmic-ray splits and geometric corrections using the M software (Koekemoer et al. 2002), which in turn uses the D routines (Fruchter and Hook 2002). Our ACS observations employed a generous 4-point dithering pattern combined with a 2-way cosmic-ray split, providing the final drizzled images with high S/N ratio, excellent dynamic range and highly reliable cosmic-ray rejection. In the case of the first-epoch WFPC2 images we used the standard *HST* data products for individual exposures, and then used the D task of the IRAF package to correct the geometric distortions. For cosmic-ray cleaning, registering and combining these corrected images we developed dedicated IRAF scripts. The quality of our final cross-instrument astrometry is limited by the larger pixel size, as well as the lower S/N ratio and number of the individual first-epoch PC frames available for stacking (see § 3.4).

3.3.2 Object catalogues and PSF fitting

The instrumental positions and magnitudes of the field objects were measured using the IRAF task S F , an improved version of D F that fits Gaussian profiles to stellar images. The combined images from both the WFPC2/PC and ACS/HRC detectors have a well-sampled point spread function (PSF) with the full-width-at-half-maximum (FWHM) of stellar images, respectively, 2.4 and 2.8 pixels. Our PSF fits were restricted within the area of the Airy disc (3.0 and 2.0 pixel radius for PC and HRC data respectively), where the point source flux is well approximated by the Gaussian model. Outside the Airy disc the PSFs show a variety of shapes, including rings, possible diffraction spikes and bright spots in the case of higher S/N objects. These features can mimic stars and need to be carefully considered during object cross-identification. We imposed a minimum separation of 3$\times$FWHM between any two sources detected in the same image and verified that there are essentially no spurious objects in the final source lists. The loss of number statistics due to the accidental rejection of actual stars in tight groups is insignificant. In fact, the centroid measurements for objects in the wings of other stars are notoriously unreliable and best avoided. The minimum separation cut also helps in cross-identification of objects between the two epochs (§ 3.4), since the expected intrinsic object shifts may reach $\sim$2 pixels.

The final object catalogues were converted to the VEGA magnitude system (Girardi et al. (2002) and references therein) and the astrometric transformations to the Galactic (l, b) coordinates were established using the World Coordinate System (WCS) headers of the ACS images. Our estimated S/N ratios for object fluxes are based on propagated errors in pixel counts that account for photon statistics (§1.4.3).

3.4 Estimating transverse motions of the Galactic bulge stars

Absolute astrometry is difficult in the crowded Galactic bulge fields. Until we can establish a decent sample of extragalactic objects shining through the low extinction windows (c.f. Sumi et al. 2005), the only readily available reference velocity in the Galactic bulge is the mean velocity along the line of sight. By setting to zero the mean proper motion for a group of stars selected without use of the kinematic information, we still preserve the kinematic meaning of the second order moments. In this analysis we use the magnitude- and distance-selected samples to investigate the spatial dependence of the covariance matrix of the transverse velocity field across the Galactic bar.

3.4.1 Relative proper motions and their dispersions

Having measured the instrumental positions of stars on both the first- and the second-epoch images, we tied the WFPC2/PC positions to the ACS/HRC pixel grid. The object shifts Δl and Δb in the Galactic coordinates between the two epochs could then be calculated using the WCS information from the ACS headers. We derived third-order polynomial transformations between the pixel grids of the two detectors using a least-squares fit to the positions of a few hundred stars in the magnitude range $16.5 < I_{\mathrm{F814W}} < 21.5$. Stars brighter than $I_{\mathrm{F814W}} = 16.5$ were often saturated while those with $I_{\mathrm{F814W}} > 21.5$ were too faint to have useful S/N ratios, particularly for the fields with short exposures (Tables 3.1 and 3.2). Our procedure for cross-identifying stars starts from matching the first 20 objects (out of ~50 brightest stars with $17 < I_{\mathrm{F814W}} < 18$) using the triangle matching algorithm (Groth 1986 and Woźniak 2000). The initial low-order fit is then iteratively refined. A star with a transverse velocity of 100 km/s at a distance of 8 kpc will move by 26.4 mas, or roughly one ACS/HRC pixel, assuming a 10 year baseline. Accordingly, we adopted a tolerance radius of 100 mas for the final matching.

After geometrically aligning and transforming object positions to the Galactic (l, b) coordinates, we folded the data with the time baseline and estimated all components of the transverse velocity tensor, i.e. dispersions $\sigma_{\rm l}$, $\sigma_{\rm b}$ and the normalized covariance $C_{\rm lb} \equiv \sigma_{\rm lb}/(\sigma_{\rm l}\sigma_{\rm b})$. The sample of stars used to trace the kinematic parameters of the Galactic bulge was limited to the magnitude range $18.0 < I_{\rm F814W} < 21.0$, i.e. dominated by the bulge main-sequence population near the turn-off point. This puts all lines of sight (with data sets of the varying depth and dynamic range) on a more common footing. However, as already noted by Kuijken and Rich (2002), the results are insensitive to the details of the magnitude cuts.

3.4.2 Astrometric errors

The 1σ centroid errors from PSF fitting (per coordinate) can be estimated from the S/N ratio:

$$\delta \approx \gamma \times \frac{\rm FWHM}{\rm S/N}, \tag{3.1}$$

where $\gamma = 0.6$ for a Gaussian PSF model and the FWHM is in pixels (see e.g. Kuijken and Rich 2002). We tested this prescription by stacking independent subsets of images taken at a single epoch. Similarly to Kuijken and Rich (2002), we find that equation 3.1 is an excellent representation of the actual astrometric uncertainties in our data, with the exception of the brightest stars, for which a constant systematic contribution of 0.025 pixel is required. Consequently, we used equation 3.1 with the systematic term added in quadrature to estimate the astrometric errors and their contribution to the apparent proper motion dispersions. The formulas for estimating $\sigma_{\rm l}$, $\sigma_{\rm b}$ and their errors corrected for the measurement variance can be found in Spaenhauer et al. (1992). Throughout this chapter we use bootstrapped uncertainties of the sample statistics (from 1000 trials) that turned out to be slightly more conservative than analytical formulas. The estimated intrinsic dispersions reported in § 3.5 are 5 – 10% lower compared to the raw values. The cross term $C_{\rm lb}$ need not be corrected, as long as the errors in l and b are uncorrelated. None of our conclusions depend on the precise value or even the presence of this correction.

The limiting S/N ratio for a useful detection in our analysis is about 10 and corresponds to a $I_{\mathrm{F814W}} \approx 21.5$ mag star in the combined image of two 40-second WFPC2/PC exposures. The same star will be detected at S/N $\approx$ 28 in the lowest quality ACS stack (eight 40-second frames). The shortest time baseline in our data is 3.388 years, and the typical 1σ astrometric uncertainties for a 21.5 mag star are $\sim$7.2 and $\sim$1.5 mas in the first- and the second-epoch images respectively. In this worst case scenario, the proper motion can be measured to an accuracy 2.5 mas yr^{-1}. The images for the first eight fields in Table 3.1 have relatively long exposure times, so the resulting proper motion errors are only $\sim$0.06 mas yr^{-1} for bright stars and $\sim$0.25 mas yr^{-1} for the faintest stars in those samples.

Table 3.3: Results of the proper motion mini-survey. The dispersions $\sigma_{\rm l}, \sigma_{\rm b}$ and the dimensionless correlation coefficient $C_{\rm lb}$ were measured for 35 lines of sight in the Galactic bulge (l, b). The number of stars $N_{\rm stars}$ used to estimate the kinematics are also given.

Field name	l [deg]	b [deg]	$\sigma_{\rm l}$ [mas yr^{-1}]	$\sigma_{\rm b}$ [mas yr^{-1}]	$C_{\rm lb}$	$N_{\rm stars}$
101-C	3.65	−3.47	2.85 ± 0.09	2.45 ± 0.08	−0.15 ± 0.05	445
104-B	2.73	−2.87	2.97 ± 0.10	2.50 ± 0.10	−0.05 ± 0.05	407
104-C	2.80	−2.93	2.74 ± 0.09	2.51 ± 0.10	−0.15 ± 0.04	482
104-D	2.79	−2.92	2.84 ± 0.10	2.36 ± 0.10	−0.10 ± 0.05	437
108-A	2.42	−2.35	2.90 ± 0.12	2.32 ± 0.12	−0.08 ± 0.06	396
108-C	2.02	−2.48	3.15 ± 0.10	2.52 ± 0.07	−0.09 ± 0.04	615
119-A	1.32	−3.77	2.89 ± 0.10	2.44 ± 0.08	−0.14 ± 0.04	471
119-C	0.85	−3.89	2.79 ± 0.10	2.65 ± 0.08	−0.14 ± 0.04	459
119-D	1.06	−4.12	2.75 ± 0.10	2.56 ± 0.09	−0.05 ± 0.06	420
120-A	1.76	−4.48	2.75 ± 0.09	2.52 ± 0.09	−0.04 ± 0.05	397
128-A	2.28	−4.08	2.63 ± 0.11	2.33 ± 0.12	−0.12 ± 0.05	357
128-B	2.33	−4.13	2.70 ± 0.12	2.29 ± 0.13	−0.13 ± 0.06	338
167-A	5.17	−4.16	2.75 ± 0.11	2.36 ± 0.09	−0.18 ± 0.05	317
94-BLG-3 .	0.68	−2.84	2.84 ± 0.10	2.58 ± 0.10	−0.12 ± 0.05	496
94-BLG-4 .	0.49	−3.00	2.58 ± 0.11	2.46 ± 0.09	−0.03 ± 0.04	413
95-BLG-10	0.89	−2.68	3.07 ± 0.10	2.41 ± 0.09	−0.12 ± 0.04	487
95-BLG-11	0.99	−4.21	2.82 ± 0.09	2.62 ± 0.09	−0.14 ± 0.04	443
95-BLG-13	3.64	−3.78	2.61 ± 0.13	2.31 ± 0.12	−0.14 ± 0.05	309
95-BLG-14	2.12	−2.78	2.95 ± 0.13	2.50 ± 0.11	−0.12 ± 0.05	463
95-BLG-19	3.87	−4.36	2.61 ± 0.11	2.17 ± 0.10	−0.13 ± 0.06	300
95-BLG-36	3.73	−3.37	2.75 ± 0.12	2.11 ± 0.11	−0.10 ± 0.05	376

Table 3.4: Results of the proper motion mini-survey (continuation of Table 3.3).

Field name	l [deg]	b [deg]	σ_l [mas yr^{-1}]	σ_b [mas yr^{-1}]	C_{lb}	N_{stars}
95-BLG-37	2.54	−3.33	2.72 ± 0.12	2.44 ± 0.12	−0.04 ± 0.05	442
95-BLG-38	2.20	−2.29	2.87 ± 0.12	2.46 ± 0.10	−0.05 ± 0.04	474
95-BLG-41	1.91	−3.07	2.79 ± 0.10	2.34 ± 0.10	−0.04 ± 0.05	450
95-BLG-7 .	5.42	−4.01	2.86 ± 0.14	1.88 ± 0.11	−0.20 ± 0.07	265
96-BLG-14	3.01	−3.24	2.71 ± 0.12	2.40 ± 0.12	−0.17 ± 0.05	373
96-BLG-17	3.17	−3.38	3.07 ± 0.10	2.55 ± 0.09	−0.16 ± 0.04	557
96-BLG-4 .	2.84	−3.57	2.68 ± 0.14	2.26 ± 0.14	−0.04 ± 0.06	329
96-BLG-5 .	3.22	−3.07	3.17 ± 0.10	2.39 ± 0.08	−0.13 ± 0.05	535
97-BLG-18	2.77	−2.87	2.99 ± 0.10	2.38 ± 0.10	−0.12 ± 0.04	433
97-BLG-24	3.40	−2.79	3.00 ± 0.11	2.39 ± 0.10	−0.10 ± 0.05	398
97-BLG-38	3.03	−2.94	2.95 ± 0.12	2.21 ± 0.10	−0.06 ± 0.05	395
97-BLG-41	1.32	−1.95	2.58 ± 0.07	2.13 ± 0.07	−0.09 ± 0.04	612
98-BLG-6 .	1.53	−2.13	3.26 ± 0.10	2.79 ± 0.12	−0.07 ± 0.05	670
99-BLG-22	2.46	−3.50	3.11 ± 0.10	2.60 ± 0.09	−0.17 ± 0.04	493
KR-BW* . .	1.14	−3.77	2.87 ± 0.08	2.59 ± 0.08	−0.07 ± 0.03	694
KR-SgrI* . .	1.26	−2.66	3.07 ± 0.08	2.73 ± 0.07	−0.09 ± 0.04	752

* The KR-BW and KR-SgrI fields are the Baade's Window and the Sagittarius-I field from Kuijken and Rich (2002)

3.5 Results

The results are given in Tables 3.3 – 3.4, and plotted in Figures 3.1 – 3.2. Proper motions for individual stars are available online[3]. After presenting our measurements

---

[3] `http://science.simkoz.com/`

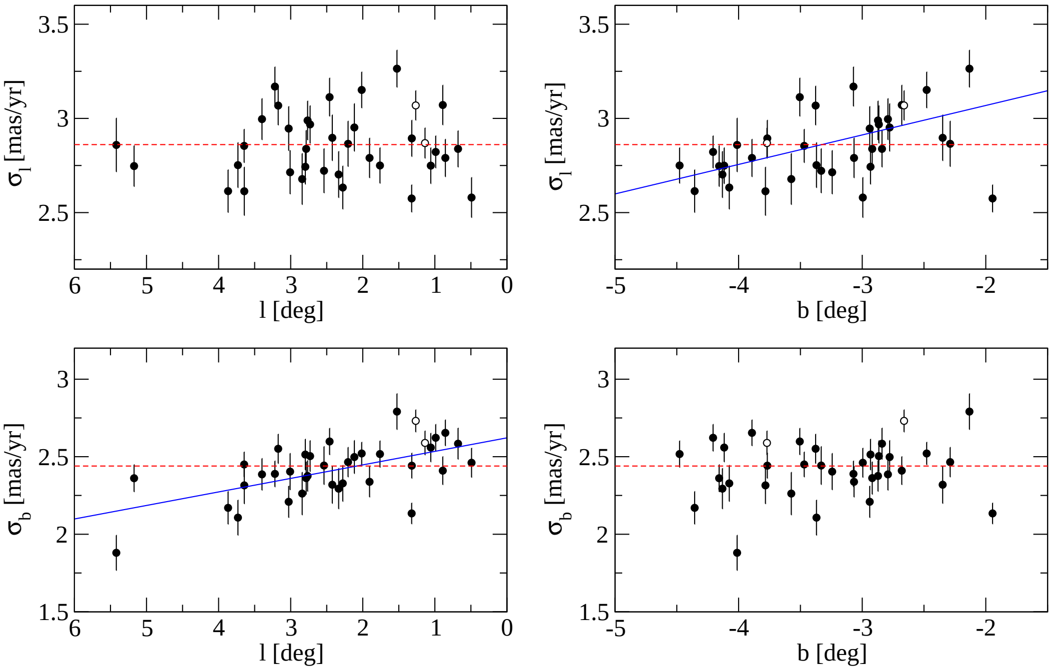

Figure 3.1: Spatial dependence of proper motion dispersions $\sigma_{\rm l}$ and $\sigma_{\rm b}$ in Galactic coordinates for our turn-off point dominated sample in the Galactic bulge (Tables 3.3 and 3.4). The two open circles are for the Baade's Window and Sagittarius-I fields from Kuijken & Rich (2002). The lines show linear regressions (solid) and weighted means (dashed) of the data. For the top right panel, the rightmost data point was not used in the fit.

we check for consistency with two other published data sets (§ 3.5.3). A more detailed discussion and comparison with the results of Kuijken and Rich (2002) follows in § 3.6.

3.5.1 Proper motion dispersions

The spatial dependence of the proper motion dispersions $\sigma_{\rm l}, \sigma_{\rm b}$ is shown in Figure 3.1. Recall that at a distance of 8 kpc, a velocity of 100 km s^{-1} implies a proper motion of 2.64 mas yr^{-1}. The most visible trends are in $\sigma_{\rm l}(b)$ and $\sigma_{\rm b}(l)$, that tend to increase closer to the Galactic plane and the Galactic centre. Both gradients are weak, but clearly present. From a simple straight line fit we find: $\sigma_{\rm l} = (0.16 \pm 0.04) \times b + 3.38 \pm 0.13$

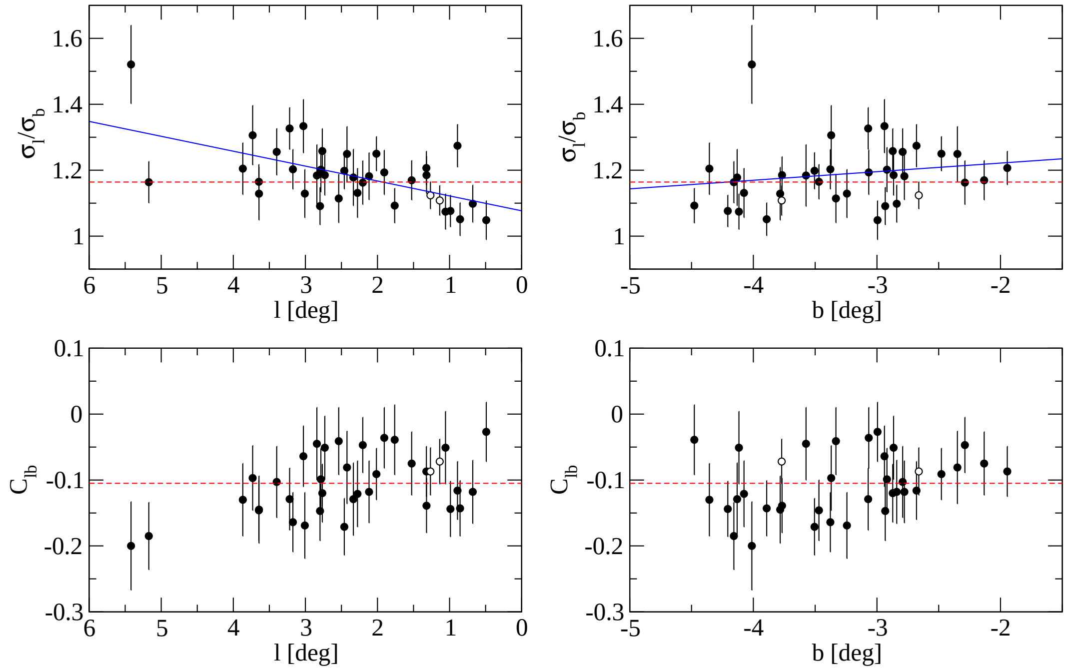

Figure 3.2: Similar to Figure 3.1 but for the anisotropy ratio $\sigma_\mathrm{l}/\sigma_\mathrm{b}$ and covariance term $C_\mathrm{lb} \equiv \sigma_\mathrm{lb}/(\sigma_\mathrm{l}\sigma_\mathrm{b})$.

and $\sigma_\mathrm{b} = (-0.09 \pm 0.02) \times l + 2.62 \pm 0.06$. Consequently, σ_b increases from 2.1 to 2.6 mas yr^{-1}, or by about 20%, as the longitude l varies from 5.5 to 0.5 deg. Similarly, σ_b changes from 2.6 to 3.2 mas yr^{-1} between $b = -4.5$ and -2 deg. Intriguingly, the last data point around $b \approx -2$ deg has some of the lowest dispersions measured for all fields. We excluded a number of possible data processing errors and the fluctuation is still marginally consistent with the observed scatter. There is no other indication of the intrinsic variations on the field-to-field scale. The distributions of $\sigma_\mathrm{l}(l)$ and $\sigma_\mathrm{b}(b)$ are flat within the scatter from random errors and projection effects in the presence of gradients.

3.5.2 Anisotropy and covariance

In Figure 3.2 we plot the apparent shape and orientation of the proper motion ellipsoid as a function of location in the bulge. There is a significant level of anisotropy, i.e.

$\sigma_\mathrm{l}/\sigma_\mathrm{b} > 1$, throughout the covered area. Moreover, the velocity distribution shows a tendency to become more isotropic for lines of sight approaching the Galactic centre at a roughly fixed latitude b. This is a reflection of the increase in σ_b with approximately constant σ_l (§ 3.5.1). The trend of more anisotropy toward the Galactic plane is also driven primarily by one of the dispersions (σ_l), but it is more difficult to see. Part of the reason for this is the narrow range of b covered by the data. The formal fits give: $\sigma_\mathrm{l}/\sigma_\mathrm{b} = (0.05 \pm 0.01) \times l + 1.08 \pm 0.03$ and $\sigma_\mathrm{l}/\sigma_\mathrm{b} = (0.03 \pm 0.03) \times b + 1.27 \pm 0.08$.

The estimates of the covariance term from Table 3.3 (plotted in Figure 3.2) are all negative and scatter uniformly in the range $-0.20 < C_\mathrm{lb} < -0.02$. This indicates that in our Galactic bulge fields the stellar motions in directions parallel and perpendicular to the plane are significantly anti-correlated. An observational bias that would account for the observed clustering of the data points has to operate in a similar way over a large range of observational settings. After investigating several possibilities, we found no explanation for this result other than a true correlation between μ_l and μ_b. Taking a field with a relatively low S/N ratio in our data and assuming perfectly correlated errors in μ_l and μ_b, the expected covariance is only $C_\mathrm{lb} \approx 0.02$. A more serious concern is a possible presence of preferred telescope orientations. Indeed, for about half of our fields the relative roll angle between the two compared observations falls in a narrow range of 25 deg. The other half, however, is spread over all possible orientations and still shows about the same covariance. The skewness of the ACS focal plane cannot be the cause of the observed correlation, because the measurements in both Kuijken and Rich (2002) fields use only WFPC2/PC data and yet they perfectly agree with the rest of the C_lb values. There is a slight hint in Figure 3.2 that C_lb may vary with longitude, although this impression seems to rely on the two points farthest from the bulge minor axis ($l = \sim 5.3$ deg in the left panel of Figure 3.2) that fall below the rest of the data.

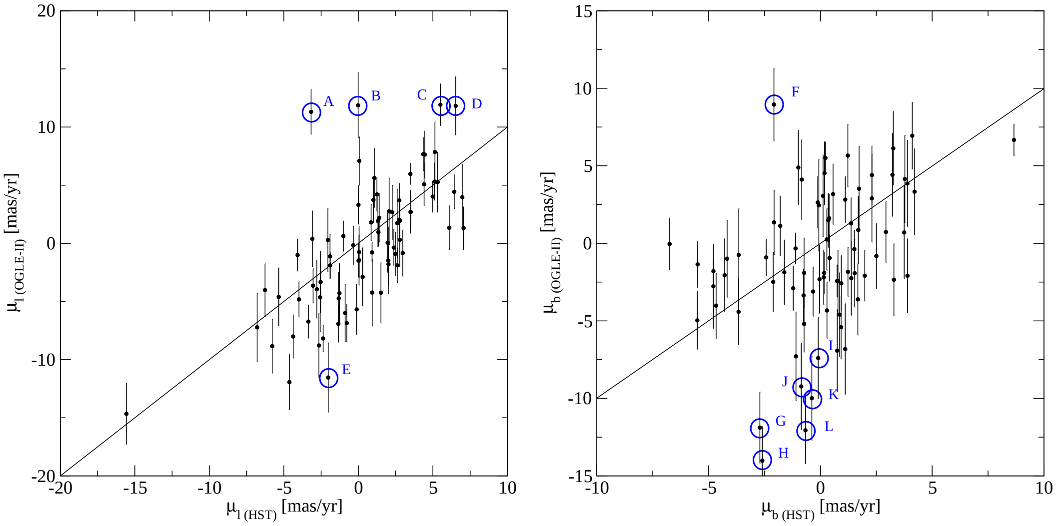

Figure 3.3: Comparison between our *HST* measurements and the ground-based OGLE–II data for bright stars from the catalogue of Sumi et al. (2004). There are 77 stars covered by our observations that have catalogue errors of 3 mas yr^{-1} or better in Sumi et al. (2004). Significant discrepancies (marked by alphabets) are caused by blending (see Figure 3.4). The solid lines indicate that the two measurements (ground-based and from the *HST*) are equal.

3.5.3 Comparisons with previous work

OGLE–II proper motion catalogue

Sumi et al. (2004) used the large number statistics of the OGLE–II database (Udalski et al. 1997) to derive relative proper motions of ∼5×10^5 stars in the Galactic bulge region from hundreds of observations covering a 4-year baseline. The OGLE–II catalogue is a valuable resource for kinematic studies of bright stars such as Red Clump Giants (RCG) that are relatively free of source confusion effects. However, at the 1.3″ FWHM seeing of the ground based OGLE–II images, a random RCG star still has ∼38% probability of being strongly perturbed by an unresolved blend (Sumi et al. 2006). It is instructive to cross-validate the results of Sumi et al. (2004) and our high-resolution *HST* measurements against each other.

Out of 35 programme fields in Tables 3.1 and 3.2, 15 are covered by the OGLE–II

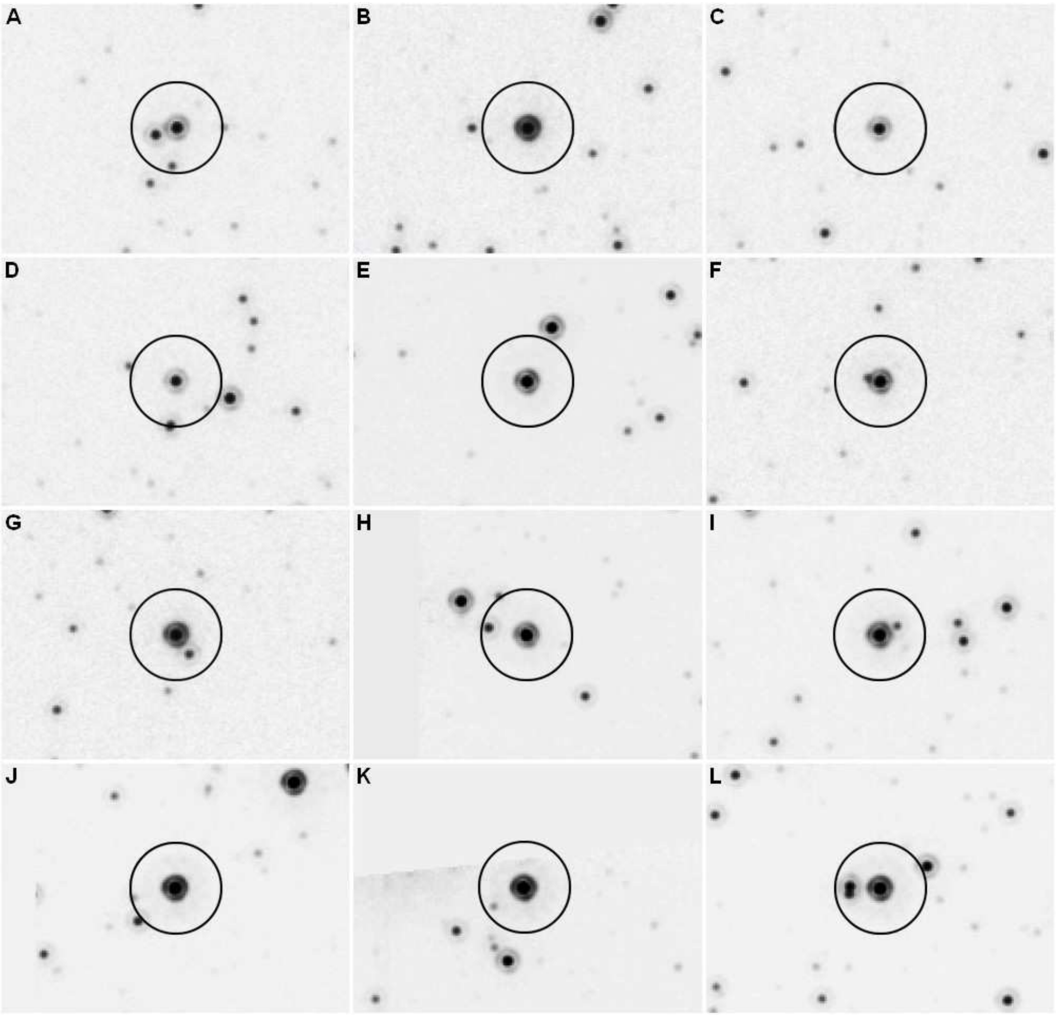

Figure 3.4: Cut-off *HST* images for the outliers marked by alphabets in Figure 3.3. All significant outliers in Figure 3.3 can be linked to source confusion and flux blending.

proper motion catalogue. In our *HST* sample we found 77 stars for which the catalogue proper motion error is 3 mas yr^{-1} or better. The two data sets were compared star by star after adjusting for an arbitrary zero point of the proper motion scale. The results are plotted in Figure 3.3 and show a good overall agreement between our measurements and those of Sumi et al. (2004). All significant outliers were labelled and checked for blending. Figure 3.4 demonstrates that virtually all these substantial discrepancies are linked to the presence of an unresolved companion within $\sim 1''$ of the primary object.

Table 3.5: Proper motion dispersions from Kuijken and Rich (2002) compared with the results of our reanalysis of the same data

			This work		
Field	l [°]	b [°]	σ_l [mas yr^{-1}]	σ_b [mas yr^{-1}]	N_stars
BW	1.14	−3.77	2.87 ± 0.08	2.59 ± 0.08	694
Sgr-I	1.27	−2.66	3.07 ± 0.08	2.73 ± 0.07	752

			Kuijken and Rich (2002)		
Field	l [°]	b [°]	σ_l [mas yr^{-1}]	σ_b [mas yr^{-1}]	N_stars
BW	1.14	−3.77	2.91 ± 0.06	2.51 ± 0.05	1076
Sgr-I	1.27	−2.66	3.10 ± 0.06	2.73 ± 0.05	1388

Kuijken & Rich (2002)

Our approach to measure the positions and proper motions of stars (§ 3.3.2) is somewhat simpler than the method used by Kuijken and Rich (2002). The latter study used the images from the WFPC2/WF chips and had to accommodate a strong undersampling of the PSF. In contrast, our use of the WFPC2 data was limited to the critically sampled images from the PC detector. The second-epoch ACS/HRC images have four times the PSF sampling of the WF images, so we could take advantage of the conventional PSF fitting techniques.

Regardless, in order to eliminate the possibility of a hidden error we re-analysed the PC data in both fields studied by Kuijken and Rich (2002) using our tools. Table 3.5 shows the results of this comparison. The agreement between the two sets of measurements is remarkably close despite significant differences in the sample size and the adopted selection criteria. This also confirms that our results are not significantly affected by several subtle instrumental effects that can potentially influence astrometric work with the *HST* images (e.g. Kuijken and Rich 2002 and references therein).

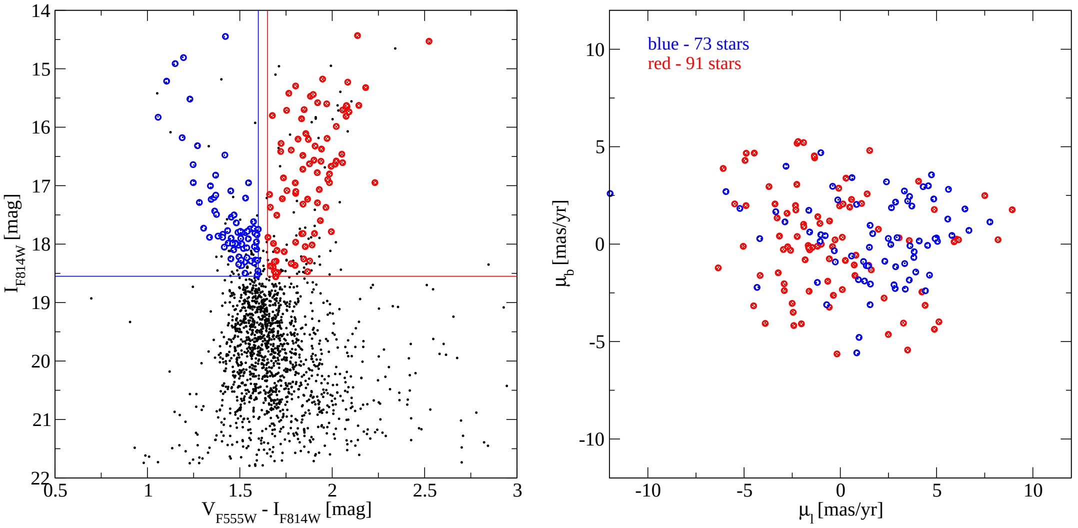

Figure 3.5: Colour-magnitude diagram (CMD; left) and relative proper motions (right) for stars in three nearly coincident stellar fields from Tables 3.3 and 3.4: 97-BLG-18, 104-C and 104-D. The red and blue stars above the turn-off point show the kinematics characteristic of the bulge and disk populations, respectively.

3.6 Discussion

3.6.1 Distance and population trends

The study of Kuijken and Rich (2002) focused on cleaning the Galactic bulge population and removing the contamination by the bluer disk stars. Above the bulge turn-off point, the stellar colours alone are sufficient to separate the blue disk main-sequence from the red giants, subgiants and clump giants. The size of our fields is generally too small to provide useful statistics of bright stars above turn-off point, and good colour information is only available for about 1/3 of the lines of sight. However, three of the fields in Tables 3.1 and 3.2 with useful colours (97-BLG-18, 104-C and 104-D) are close to each other and were combined in order to look for a kinematic distinction between the Galactic disk and bulge populations. Figures 3.5 and 3.6 show that in the frame of reference of a mean star (of any colour), the longitude proper motions of the blue disk stars are biased toward positive values, while the red bulge stars tend to

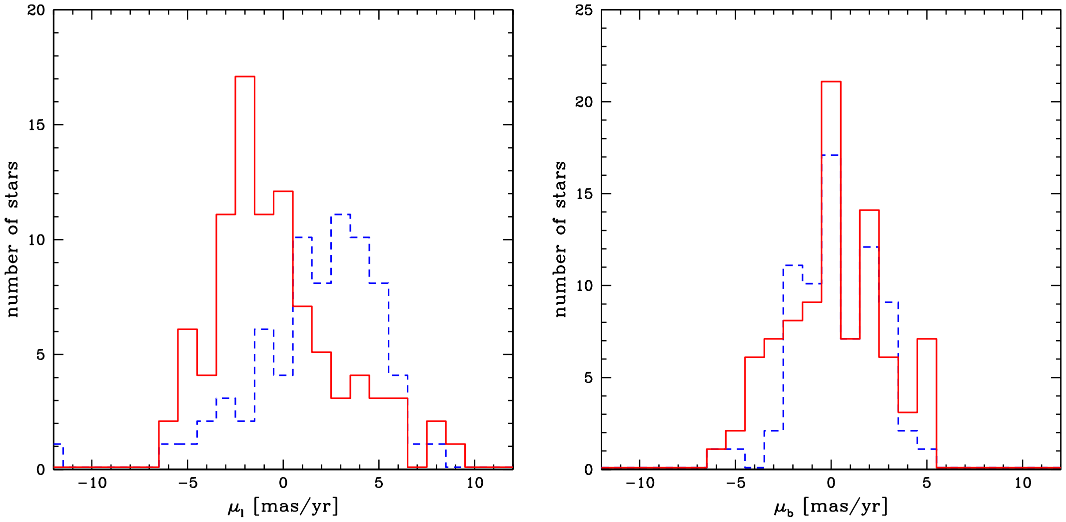

Figure 3.6: Histograms of relative proper motions of the red (solid line) and blue (dashed line) samples from Figure 3.5. The blue disk stars ‘rotate in front’ of the Galactic bulge parallel to the plane.

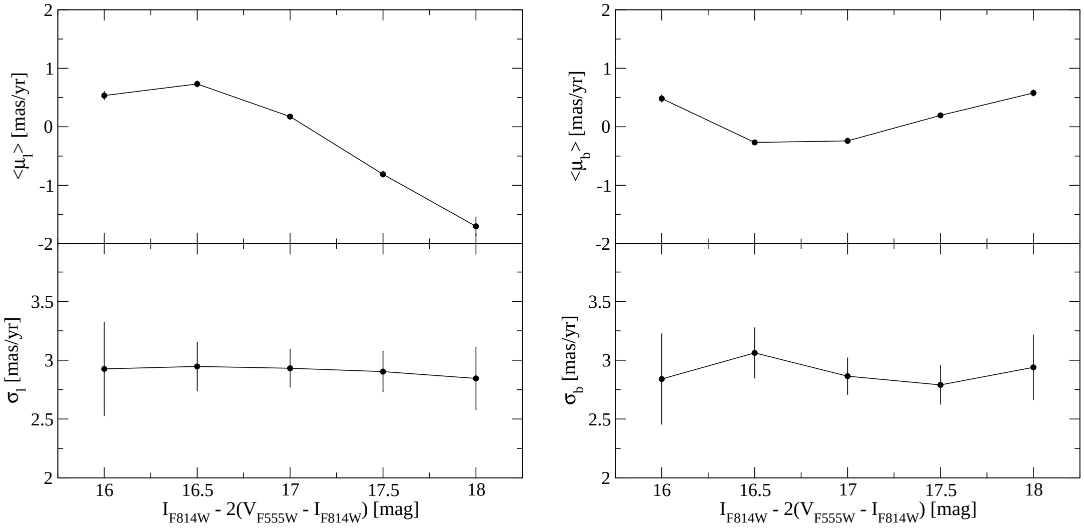

Figure 3.7: Average relative proper motions and dispersions of stars in Baade’s Window in bins of $M^* \equiv I_{F814W} - 2 \times (V_{F555W} - I_{F814W})$, an approximate distance indicator.

have more negative μ_l. The blue and red samples were selected, respectively, using the conditions $(V - I) < 1.65$ and $(V - I) > 1.7$. This effect was previously observed by Kuijken and Rich (2002) in their two fields with multi-epoch WFPC2 data and there is little doubt that it is due to the disk stars ‘rotating in front’ of the bulge.

Kuijken and Rich (2002) also devised an approximate distance measure:

$$M^* = I_{F814W} - 2(V_{F555W} - I_{F814W}), \tag{3.2}$$

chosen to remove the slope of the main-sequence in the colour-magnitude diagram. In Figure 3.7 we present the average proper motions and their dispersions for the Baade’s Window in bins of M^*. As expected, with an increasing depth along the line of sight, the kinematic signature gradually changes from that characteristic of the disk stars, to the one typical for the bulge. In the Kuijken and Rich (2002) data this trend continues to very faint stars that are likely on the far side of the bulge, and if so, it constitutes a ‘rotation curve’ of the bulge. The colours for our fields are generally of lower S/N ratio or nonexistent, and do not allow to see this in much detail.

3.6.2 Stellar velocity ellipsoid of the Galactic bar

A detailed modelling of the measurements in Table 3.3 is beyond the scope of this chapter. Here we only comment on possible directions and new possibilities.

Zhao et al. (1996) interpreted the bulge anisotropy in terms of the rotation support of the Galactic bulge and related the ratio σ_l/σ_b directly to the level of flattening of the light density distribution. They also concluded that the value $\sigma_l/\sigma_b = 1.10 - 1.15$ observed in Baade’s Window ($l = 1^\circ, b = -4^\circ$), with which our measurements are consistent, can be explained by rigid rotation. The presence of any disk stars, however, will also contribute rotational broadening to σ_l. Since in the vicinity of our fields the disk fraction increases closer to the plane, it follows that the measured gradient $\sigma_l = (0.16 \pm 0.04) \times b + 3.38 \pm 0.13$ could be due to disk contamination. The changes of skewness in the μ_l distribution tend to support this (c.f. Figure 3.6). Another possibility is that the rotation rate of the bulge actually increases at lower $|b|$, as found by Izumiura et al. (1995) from the radial velocities of 124 SiO masers in the Galactic bulge. It has been observed that for giants in Baade's Window the metal-poor stars display more spread in the vertical motion and less anisotropy when compared to metal-rich samples (Zhao et al. 1994, 1996). Both of these metallicity dependencies are quite steep, so it is likely that the gradient $\sigma_{\rm b} = (-0.09 \pm 0.02) \times l + 2.62 \pm 0.06$ is related to a changing mix of populations with more metal-poor stars closer to the Galactic bulge minor axis.

We are not aware of any previous detections of the cross terms in the Galactic bulge velocity field except the report by Zhao et al. (1994) of a significant vertex deviation between the radial and longitudinal motions from $C_{\rm rl}$. That result is based on a photographic sample of ~200 K and M giants from Spaenhauer et al. (1992). We note that the latter sample actually shows a hint of a slightly negative covariance between $\mu_{\rm l}$ and $\mu_{\rm b}$ (c.f. Figure 1 of Zhao et al. 1994). The superb resolution of the *HST* enabled very significant detections of the $C_{\rm lb}$ cross term in many fields. The non-diagonal elements of the velocity tensor are crucial to determining the dominant orbit families, the importance of streaming motions and the need for the intrinsic anisotropy versus solid body rotation in the Galactic bulge (Zhao et al. 1994, 1996; Häfner et al. 2000). Häfner et al. (2000) published detailed calculations of $C_{\rm lb}$ for several lines of sight at positive longitudes including Baade's Window ($l = 1^\circ, b = -4^\circ, C_{\rm lb} = 0.04$), and two others: ($l = 8.4^\circ, b = -6^\circ, C_{\rm lb} = 0.15$) and ($l = 1.21^\circ, b = -1.67^\circ, C_{\rm lb} = 0.04$). Taken at face value these predictions are roughly of the same magnitude as the results from § 3.5, but have the opposite sign. For a proper comparison with dynamical models such as the ones in Häfner et al. (2000) and Bissantz et al. (2004) we need to wait until the calculations are folded with the appropriate selection functions, since our measurements are based on substantially deeper data than most of the previous samples.

3.7 Summary and conclusions

The main results of our proper motion mini-survey are: (1) high quality proper motion measurements for hundreds of stars along 35 lines of sight across the Galactic bar, (2) establishing the presence of spatial gradients in the dispersions $\sigma_{\rm l}, \sigma_{\rm b}$ and the amount of anisotropy $\sigma_{\rm l}/\sigma_{\rm b}$, and (3) the first reliable detection of the covariance term $C_{\rm lb}$ of the transverse velocity tensor. We cross-validated our measurements with the ground-based OGLE–II data of Sumi et al. (2004) and the benchmark study of Kuijken and Rich (2002). The observed slow rise of $\sigma_{\rm l}$ toward the Galactic plane is likely due to the increasing disk contamination and/or a possible gradient in the bulge rotation speed. The increase in $\sigma_{\rm b}$ toward the minor axis of the bulge is accompanied by the decreasing ratio $\sigma_{\rm l}/\sigma_{\rm b}$ and most likely results from the increasing fraction of metal-poor stars. We clearly detect the covariance term $C_{\rm lb} \approx -0.10$ that implies a significant tilt of the Galactic bulge velocity ellipsoid with respect to the Galactic plane. Adopting a bar angle of 20° and the velocity dispersions in Han and Gould (2003), we find the tilt is $\sim -16^\circ$ away from the Galactic plane using the same procedures as in Binney and Merrifield (1998).

The data presented in this chapter provide qualitatively new constraints on dynamical models of the inner Galaxy and dramatically improved number statistics. It may be possible in the near future to augment our proper motion samples with the distance and metallicity estimates. As shown by Kuijken and Rich (2002), deep colour-magnitude diagrams can supply sufficiently accurate distance information to effectively isolate the bulge population. In order to maximize the discriminating power of model comparisons the focus should be on extending the coverage to negative longitudes and locations further from the Galactic centre.

Acknowledgements

We thank Profs. Bohdan Paczyński, Ian Browne and Drs. Vasily Belokurov, Wyn Evans and Nicholas Rattenbury for helpful comments.

4

The first direct detection of a gravitational μ–lens toward the Galactic bulge[1]

4.1 Abstract

We present a direct detection of the gravitational lens that caused the microlensing event MACHO-95-BLG-37. This is the first fully resolved microlensing system involving a source in the Galactic bulge, and the second such system in general. The lens and source are clearly resolved in images taken with the High Resolution Channel of the Advanced Camera for Surveys on board the *Hubble Space Telescope* (*HST*) ~9 years after the microlensing event. The presently available data are not sufficient for the final, unambiguous identification of the gravitational lens and the microlensed source. While the light curve models combined with the high-resolution photometry for individual objects indicate that the source is red and the lens is blue, the colour-magnitude diagram for the line of sight and the observed proper motions strongly support the op-

---

[1] The work presented in this chapter has been accepted for publication in ApJ as Kozłowski S., Woźniak P. R., Mao S. and Wood A. (2007, in press)

posite case. The first scenario points to a metal-poor lens with mass $M \approx 0.6\mathrm{M}_\odot$ at the distance $D_\mathrm{l} \approx 4$ kpc. In the second scenario the lens could be a main-sequence star with $M = 0.8 – 0.9\mathrm{M}_\odot$ about half-way to the Galactic bulge or in the foreground disk, depending on the extinction.

4.2 Introduction

Gravitational microlensing of stars within the Local Group of galaxies (Paczyński 1996) directly probes both luminous and dark matter concentrations along the line of sight. Over the past decade microlensing surveys have continued to enable observations with far-reaching implications, such as constraints on the fraction and content of Galactic dark matter (e.g. Alcock et al. 1996, 1998, 2001a), discovery and characterization of exo-planet systems (Bond et al. 2004; Udalski et al. 2005; Beaulieu et al. 2006; Gould et al. 2006), and measurements of the fundamental properties of stars and their evolutionary end points (Bond et al. 2004; Abe et al. 2003; Gould et al. 2004). Unfortunately, while the light curve of a microlensing event provides the key discovery signature, it is insufficient to solve uniquely for the mass, the distance and the relative transverse velocity of the lens. As a result, out of a few thousand events discovered to date, only a handful allowed the mass of the lens to be measured (An et al. 2002; Gould et al. 2004; Jiang et al. 2004).

In the case of microlensing by a luminous body (a star) the basic degeneracy of the model can be broken by directly observing both the lens and the source. The difficulty with this approach, however, is inherent in the geometry of microlensing that implies milli-arcsecond separations between the lens and source components during the event. So far MACHO-LMC-5 was the only microlensing event for which the lensing body has been resolved (Alcock et al. 2001b). The lens that gravitationally magnified the source in the Large Magellanic Cloud turned out to be a nearby M dwarf in the Galactic disk (Drake et al. 2004; Gould et al. 2004). Bennett et al. (2006) demonstrated the presence of a bright lens component in the planetary microlensing event OGLE-

2003-BLG-235/MOA-2003-BLG-53 and estimated the mass of the host star using the centroid shift of the combined light.

Here we report a direct detection and mass measurement of the gravitational lens responsible for the MACHO-95-BUL-37 event – the first fully resolved microlensing system involving a Galactic bulge source, and the second such system in general.

4.3 Microlensing event MACHO-95-BLG-37

The event was discovered by the MACHO collaboration as a single and apparently achromatic brightening of object 109.20635.2193 in their photometric monitoring database of the Galactic bulge (see Thomas et al. 2005). The object is quite faint ($V \approx 20$ mag) and located in one of the densest fields covered by the survey: equatorial (J2000) and Galactic coordinates $(\alpha, \delta) = (18\text{h}04\text{m}34.44\text{s}, -28^\circ25'33.7'')$, $(l, b) = (2^\circ\!.54, -3^\circ\!.33)$. The location of the MACHO-95-BLG-37 event was one of the targets in our proper motion mini-survey of the Galactic bulge (Chapter 3; Kozłowski et al. 2006a). Each of the 35 fields in the mini-survey was centered on a microlensed source and was covered by two *Hubble Space Telescope* (*HST*) pointings taken several years apart. Using several relatively isolated stars we could co-register the *HST* and ground-based MACHO images to within $0.1''$ and unambiguously identify microlensed sources, even in the presence of additional stars that were only resolved in the *HST* images.

In the case of MACHO-95-BLG-37 we found that not only is the microlensed source accompanied by another very close star with comparable brightness, but also that the relative proper motion of the two components places them within 2.6 ± 3.5 mas of each other on 21 September 1995 (HJD 2449982.3) when the microlensing event took place. The prior probability that the blend is a random coincidence is very small, so we have a clear indication that the companion source is actually the gravitational lens that caused the event of 1995. Before we begin a detailed investigation of this finding (§§ 4.4 – 4.6) we first describe the available data and basic data reductions.

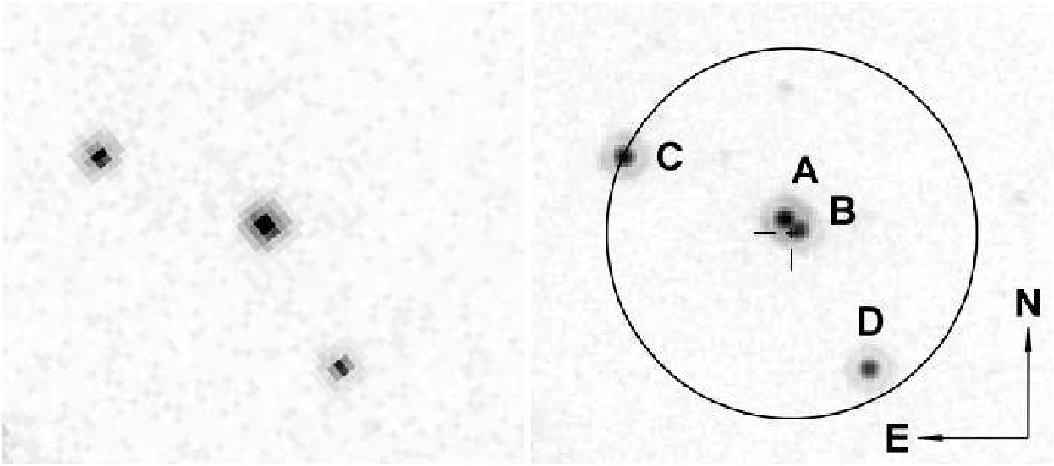

Figure 4.1: *HST* images of the MACHO-95-BLG-37 event location. The first-epoch WFPC2/PC image (left) and the second-epoch ACS/HRC image (right) were taken, respectively, 3.71 and 8.95 yr after the maximum light. The relative trajectory of stars A and B places them within 2.6 mas of each other at the time of the microlensing event. The circle shows a seeing disk characteristic of the ground-based MACHO survey (FWHM $\approx 2''.1$). The crosshair indicates the unbiased centroid of the lensed light from difference imaging.

4.3.1 *HST* astrometry and photometry

A detailed description of the relevant *HST* data[2] is presented in Chapter 3 and only the essential facts are repeated here. The first- and second-epoch images were collected, respectively, 3.71 and 8.95 yr after the event. The first pointing employed the Planetary Chip (PC) of the Wide Field Planetary Camera 2 (WFPC2) instrument, and provided (nearly) simultaneous colour information in both V and I photometric bands using F555W and F814W filters. During the second pointing we used the High Resolution Channel (HRC) of the Advanced Camera for Surveys (ACS) and obtained high signal-to-noise ratio (S/N) imaging in the F814W filter only. In each case we co-added all suitable F555W and F814W images for a given epoch. The field of view covered by the ACS/HRC and WFPC2/PC detectors is similar ($29'' \times 26''$ and $35'' \times 35''$, respec-

---

[2] `http://archive.stsci.edu/hst/`

tively), but not the pixel size (25 versus 45.5 mas). At the *HST* resolution the MACHO database object associated with the microlensing source was immediately revealed to be a composite of four unresolved stars, which we label A through D (Figure 4.1).

The magnitudes and positions of stars A – D were extracted from the fits of stellar profiles. The local point spread function (PSF) models were generated using the TINYTIM software (Krist 1993, 1995) and interpolated with bi-cubic splines. For all model fitting we used the MINUIT package (§1.4.5). Stars A and B have overlapping profiles and required a special model with two PSF components fitted simultaneously. A small section of the ACS/HRC image was fitted first, providing an unbiased value of the second-epoch separation between the two components and a good handle on the flux ratio in the $I_{\rm F814W}$-band. The flux ratio was then fixed at the second-epoch value for the purpose of fitting the $I_{\rm F814W}$-band WFPC2/PC image and obtaining the first-epoch astrometry. Finally, the $(V - I)$ colours of stars A and B were established by fitting the $V_{\rm F555W}$-band image using a model with variable flux ratio and the blend separation fixed at the value taken from the $I_{\rm F814W}$-band fit for the same epoch. The resulting astrometric and photometric measurements are given in Tables 4.1 and 4.2. Note that in the V-band the only available high-resolution imaging comes from the relatively shallow first-epoch WFPC2/PC observation, so the A/B flux ratio is poorly constrained and the errors in V and $(V - I)$ are relatively large for these two stars. In the I-band, however, we have an accurate measurement of the flux ratio from ACS/HRC that allowed us to eliminate a degenerate free parameter from the double PSF fit of the WFPC2/PC data. This explains why the astrometric accuracy for the first-epoch is actually better than for the second-epoch, despite a larger pixel size and a much smaller separation between stars A and B in the WFPC2/PC images compared to the ACS/HRC data. Using simulated images we found that our first-epoch astrometry is biased by about 1.5% toward lower separations. We could not find a better procedure that would eliminate this effect, so a post-factum correction was included in the WFPC2/PC data reported in Table 4.1.

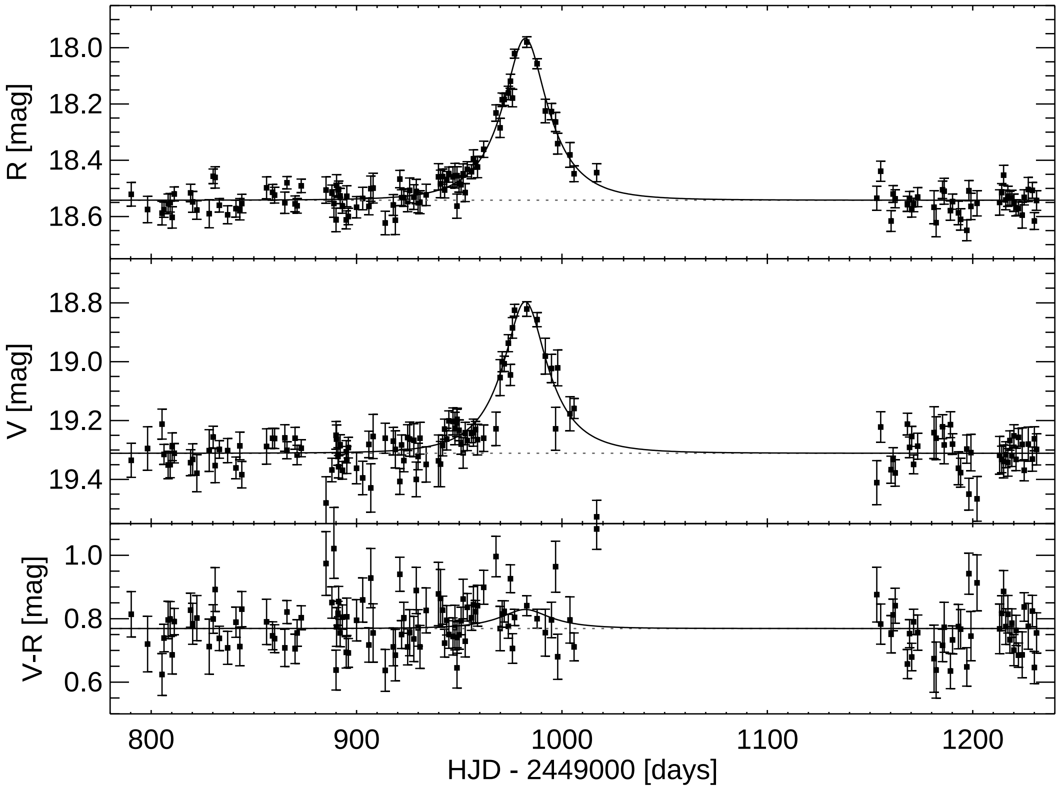

Figure 4.2: Light curve of the MACHO-95-BLG-37 event from our Difference Image Analysis of data in the public MACHO database. A significant colour change near the peak magnification indicates that the microlensed source is redder than the unresolved composite of stars A, B, C and D from Fig. 4.1.

4.3.2 Microlensing light curve revisited

The MACHO-95-BLG-37 event was recorded on a faint star subject to intense crowding, and therefore the standard light curve in the MACHO photometric database has a very low S/N. In order to reduce the uncertainties of the microlensing parameters derived from light curve modelling we performed Difference Image Analysis (DIA; Alard and Lupton 1998; Alard 2000; Woźniak 2000) on the original ground-based images, i.e. on the simultaneous two-colour imaging data collected by the MACHO survey[3]. The PSF matching and photometric solutions were confined to a $2'.5 \times 2'.5$

---

[3] `http://wwwmacho.mcmaster.ca/Data/MachoData.html`

Table 4.1: *HST* astrometry

Instrument	Epoch	$t - t_0$	ΔRA	ΔDEC
	[yr]	[yr]	[mas]	[mas]
WFPC2/PC	1999.43	3.71	-29.9 ± 1.3	-24.9 ± 1.3
ACS/HRC	2004.67	8.95	-74.5 ± 1.6	-63.1 ± 1.6

ΔRA, ΔDEC are positions of star B relative to star A (Figure 4.1) in
a cartesian reference frame aligned with the local equatorial coordinates.
The moment of maximum light t_0 corresponds to HJD = 2449982.3 (Epoch 1995.72).

Table 4.2: *HST* photometry

Star	V_{F555W}	I_{F814W}	$(V - I)$	f_V	f_I
		[mag]	[mag]		
A	20.24 ± 0.08	18.45 ± 0.02	1.79	0.28	0.35
B	20.30 ± 0.08	19.07 ± 0.04	1.23	0.26	0.19
C	20.29 ± 0.03	18.66 ± 0.03	1.63	0.27	0.28
D	20.63 ± 0.04	19.18 ± 0.04	1.45	0.19	0.18

f_V, f_I are fractional contributions to the total flux.

region around the source (approximately 256 × 256 pixels). After discarding observations outside the relevant time interval and rejecting a small fraction of frames with bad seeing we considered a total of 132 images in each of the MACHO photometric bands b_{M} and r_{M}. High S/N reference images were constructed by co-adding 9 good-quality images with a well-behaved PSF. From a series of difference frames in which the source was significantly magnified we derived an unbiased centroid of the lensed light that clearly points to the pair of stars A and B when transformed to the ACS/HRC coordinates (Figure 4.1). One of these two stars must then be the microlensed source.

The reference flux in each band was derived from a comparison between our differential fluxes and conventional PSF photometry obtained with the D P software

(Schechter et al. 1993) running in a fixed-position mode with the input object lists based on our deep reference images. Stars C and D could not be properly deblended, even using fixed *HST* positions transformed to the template coordinates. The template position of the A – D composite was set to the mean ACS/HRC position of stars A and B. We selected 31 calibration images per photometric band with the best overall seeing, background and transparency. In seven of these images the source was visibly magnified. The statistical uncertainty of the reference flux is 8% in $b_{\rm M}$ and 9% in $r_{\rm M}$. The background level estimated by the DoPHOT algorithm in a crowded field is somewhat sensitive to the assumed shape of the PSF (especially in the wings). In our case of a very faint object near the detection limit set by the source confusion we find that the systematic uncertainty in the reference flux can easily reach 10%. This generic problem is partially alleviated by the fact that the systematics are similar in both filters and source blending must always be considered in the analysis of individual light curves in crowded fields.

The final light curves (Figure 4.2) were shifted to the instrumental $b_{\rm M}$, $r_{\rm M}$ scale of the MACHO database using a median offset for a few tens of bright stars near the location of the MACHO-95-BLG-37 event and transformed to approximately standard $V_{\rm M}, R_{\rm M}$ magnitudes following Popowski et al. (2005). We also determined transformations between $V_{\rm M}, R_{\rm M}$ and the standard V, I magnitudes:

$$\begin{aligned} V_{\rm M} &= V + (0.05 \pm 0.11)(V - I) + (0.01 \pm 0.20), \\ R_{\rm M} &= I + (0.62 \pm 0.10)(V - I) - (0.17 \pm 0.18). \end{aligned} \tag{4.1}$$

Hereafter, the subscript is omitted and MACHO filters are implied for V, R photometry. The overall quality of the V-band light curve is lower compared to that in the R-band due to occasional pixel level defects in the $b_{\rm M}$ frames that were clearly visible in the difference images.

Table 4.3: Microlensing light curve model

Parameter	Value	Error
t_0 [days]	982.3	0.3
t_E [days]	25.2	4.2
u_0	0.37	0.10
$f_{\mathrm{s},V}$	0.33	0.12
$f_{\mathrm{s},R}$	0.38	0.14
m_V [mag]	19.314	0.005
m_R [mag]	18.545	0.003
χ^2_ν	1.490	—
ν	255	—

Maximum magnification is at t_0 days after HJD = 2449000.

4.4 Microlensing light curve models

The first step is to obtain the basic microlensing parameters such as the timescale t_E, the dimensionless impact parameter u_0, the moment of the peak brightness t_0, and the baseline magnitudes $m_{V,R}$. In order to preserve consistent colour information, both V- and R-band light curves were fitted simultaneously with a simple microlensing model that allows for flux blending (source fractions $f_\mathrm{s} < 1$). The data point at $t = 1016.9$ days is a moderate outlier in the V-band light curve (Figure 4.2) and is rejected in all analyses. The change in χ^2 due to this cosmetic change is not significant and none of our conclusions are affected. The resulting best-fit model is given in Table 4.3 and provides a marginally acceptable fit (reduced $\chi^2_\nu = 1.49$ for $\nu = 255$ degrees of freedom).

4.4.1 Colours

Using different parameterisations of the model equivalent to the one in Table 4.3, we obtained the source/blend colours and the colour difference with the error bounds that fully account for covariance: $(V-R)_\mathrm{s} = 0.92 \pm 0.04$, $(V-R)_\mathrm{b} = 0.68 \pm 0.04$ and $\Delta(V-R)_\mathrm{s,b} = (V-R)_\mathrm{s} - (V-R)_\mathrm{b} = 0.24 \pm 0.06$. This corresponds to a positive colour shift during the event $\Delta(V-R)_\mathrm{event} \approx +0.06$ mag and indicates that the source is redder than the blend. However, it must be emphasized that the measurement of the reference flux for our light curves poses a significant challenge given the limitations of the available archival data (§ 4.3.2). Both $(V-R)_\mathrm{b}$ and $\Delta(V-R)_\mathrm{s,b}$ are subject to the systematics of the reference flux in two bands. The value of $(V-R)_\mathrm{s}$, on the other hand, is more reliable, because it is constrained by the magnified portion of the light curve, even if the reference fluxes are not known. This is best seen from the model of the simultaneous two-colour DIA light curve written as $\Delta F(t) = F_\mathrm{s} \times A(t) + F_0$ in each band, where $A(t)$ is the magnification factor and $F_0 < 0$ if the source is effectively magnified in the reference image. Although in most cases the source flux F_s is poorly constrained in both colours, the error bounds on the ratio $F_{\mathrm{s},V}/F_{\mathrm{s},R}$ are relatively tight due to covariance and, most importantly, independent of the flux offsets. Therefore, the derived value of $(V-R)_\mathrm{s}$ only depends on the global calibration of flux units for the reference images, which can be done much more reliably using bright isolated stars. In conjunction with the *HST* photometry, the source colour information will be crucial to deciding the identity of the microlensed source, and therefore the lens (§ 4.5.1).

4.4.2 Parallax constraints

The ground-based microlensing light curve provides useful constraints on the acceleration term in the observed trajectory of the lens relative to the source. In the case of a short, low-magnification microlensing event such as MACHO-95-BLG-37 we can only obtain one-dimensional information (Gould et al. 1994). Following the geocentric formalism of Gould (2004), we introduce into the model the dimensionless microlensing parallax vector $\boldsymbol{\pi}_{\rm E}$, where $\pi_{\rm E,\parallel}$ is the component of $\boldsymbol{\pi}_{\rm E}$ opposite the direction of the projected position of the Sun at the peak of the event. We find that $\pi_{\rm E,\parallel} = 0.07^{+0.65}_{-0.46}$, while $\pi_{\rm E,\perp}$ remains unconstrained, i.e. there is no detectable parallax. There are two observations during the event (at $t = 967.9$ and $t = 996.9$ days) with atypically low V-band fluxes and relatively large error bars compared to the adjacent measurements. Without these two data points we get $\pi_{\rm E,\parallel} = 0.00^{+0.67}_{-0.45}$ and the apparent weak asymmetry of the best-fit model goes away. In § 4.5.1 this constraint is improved using *HST* photometry and in § 4.5.2 combined with the *HST* astrometry to place limits on the relative source-lens parallax $\pi_{\rm rel}$.

4.5 Resolution of the microlensing system into lens and source

The fundamental difficulty with resolving a lens detected through time-variable magnification is that its apparent separation from the source is below the *HST* resolution for months or even years after the event. In the case of MACHO-95-BLG-37 (and similarly for MACHO-LMC-5) this problem is greatly reduced due to the rather large relative motion of stars A and B (§ 4.3.1). High-precision *HST* astrometry at two epochs well after the peak magnification allowed us to calculate a very accurate relative trajectory of star B with respect to star A. Simply connecting the two measurements in Table 4.1 we get:

$$\mathbf{r}(t) = \mathbf{r}(t_1)\frac{(t_2 - t)}{(t_2 - t_1)} + \mathbf{r}(t_2)\frac{(t - t_1)}{(t_2 - t_1)}, \tag{4.2}$$

where $\mathbf{r} = (\Delta\alpha, \Delta\delta)$ is the relative position with measurements available at $t_1 = 3.71$ and $t_2 = 8.95$ yr. The separation at the peak of the event ($t = 0$) is then:

$$(\Delta\alpha_0, \Delta\delta_0) = (1.6 \pm 2.5,\ 2.1 \pm 2.5)\ \text{mas}. \tag{4.3}$$

These values are fully consistent with a model in which the two stars are the source and lens, and which predicts a very low value of the two-dimensional separation $r_0 = r(0)$. There are two alternative possibilities: either one of the members of the pair is a random interloper, or it is a companion to either the lens or the source. The first possibility is ruled out by the following argument: In the sky region under consideration the density of stars is 0.085 and 0.176 per square arcsecond for stars brighter than $I = 18.45$ and 19.07 mag, respectively. The corresponding Poisson probabilities of a random alignment within 2.6 mas at the time of the event are 1.8×10^{-6} and 3.7×10^{-6}, respectively, i.e. very low. The other case, of one of the two detected stars being a companion to either the lens or the source, can also be ruled out. It is clear is that one of the two stars must be the source. Furthermore, the rapid relative proper motion excludes the possibility that the second star is a companion of the source (the implied binary motion will be too high, about 400 km/s at a distance of 8 kpc). Thus we only need to consider the possibility that one of the stars is a companion of an unseen dark lens, with a separation of about 2.6 mas between them (recall that the lens is almost perfectly aligned with the lensed source at the peak). This is about $b \approx 3.5$ Einstein radii (for $\theta_{\mathrm{E}} = 0.75 \pm 0.13$ mas, see §4.2). We can approximately model the perturbation of the luminous star on the dark lens as a Chang-Refsdal lens (Chang and Refsdal 1984). The shear induced by the luminous star at the position of the dark lens would be $\gamma = q/b^2 \approx 0.08$, where q is the mass ratio of the luminous companion to the dark lens. The short t_{E} does not favor a massive dark lens such as a black hole and neutron star, and so the mass ratio q is likely larger than one. The caustics will have a size roughly $2\gamma/\sqrt{1-\gamma} \approx 2q/b^2 \sim 0.16$ (e.g. Mao 1992). The caustics size is comparable to the measured impact parameter ($u_0 \sim 0.37$), which would introduce a strong asymmetry in the light curve for most trajectories (not seen in the observed low S/N light curves). Hence we regard the ‘dark’ lens scenario as not very likely. The bright lens hypothesis is thus favored and we conclude that the source and lens system involved in the MACHO-95-BLG-37 microlensing event consists of stars A and B from Figure 4.1 (in an order still to be determined). Our subsequent arguments are based on that assumption.

4.5.1 Identifying the lens

To find out which member of the candidate pair of stars is the lens, we can make use of the observed colour change during the event and the fact that gravitational lensing is achromatic. In Figure 4.3 we plot the colour-magnitude diagram (CMD) of the stellar field around MACHO-95-BLG-37 and stars A – D from Figure 4.1. The light curve in Figure 4.2 reflects the integrated flux of the four stars (unresolved in ground-based images). From the observed colour increase $\Delta(V-R)_{\rm event} \approx +0.06$ mag near the peak magnification we infer that the microlensed source is redder than the composite. Although the $(V-R)$ colours were not measured individually for stars A – D, it is very unlikely that the ordering of the $(V-I)$ and $(V-R)$ colours is different. Stars A and B are, respectively, the reddest and the bluest components of the blend, so the colour shift points to star A as the source. This is entirely in agreement with the source colour $(V-R)_{\rm s} = 0.92 \pm 0.04$ mag and the colour difference $(V-R)_{\rm s,b} = 0.24 \pm 0.06$ mag between the source and the rest of the blend found in § 4.4.1. Equation 4.1 implies *HST* $(V-I)_{\rm s} \approx 1.7$ mag, also consistent with the *HST* photometry of star A. Thus, based on the light curve evidence, star B must be the lens, because star A is the microlensed source. However, in § 4.6 we show that the physical interpretation of the CMD and kinematic data strongly argues against this result.

In principle, the *HST* photometry provides an additional test of these possibilities because we can transform the measurements to the MACHO system and obtain a constraint on the source magnitudes $V = 20.34 \pm 0.09, R = 19.38 \pm 0.05$ assuming star A, and $V = 20.37 \pm 0.11, R = 19.66 \pm 0.08$ assuming star B (including the variance and covariance in transformation coefficients). Unfortunately, the difference $\Delta\chi^2 \approx 0.1$ between the models with stars A and B as the source is completely insignificant. An additional problem is that the contributions of stars A – D to the blend are not known very well. In order to match the total MACHO baseline magnitudes (§ 4.3.2) we would have to make the transformed *HST* fluxes of all four stars fainter by 10 – 15%, depending on the photometric band, and then still assume that only about half of the flux in stars C and D is effectively added to the total flux of stars A and B. This is not surprising knowing that stars C and D are near the edge of the FWHM disk of stars A and B (Figure 4.1) – yet they are too faint to be deblended – and that in ground-based microlensing images the 'sky' level is set by a featureless continuum of merging stars. Overestimating the background by a mere few counts makes stars near the detection limit appear 0.1 – 0.2 mag fainter. The weights are probably slightly different in each photometric band due to details such as the orientation of stars C and D with respect to the PSF that is never perfectly round. Nevertheless, it is still useful to perform a microlensing light curve fit with a single additional 'measurement' of the source magnitude, i.e. effectively constrain f_s. Compared to the results in § 4.4.2, the error bounds on the dimensionless parallax are improved, yielding $\pi_{E,\parallel} = 0.0 \pm 0.4$ for any reasonable set of flux weights.

4.5.2 Proper motion, Einstein ring radius and relative parallax

The relative proper motion $\mu_{\rm rel}$ of the lens with respect to the source provides further clues about the physics of the event. For the case at hand, a robust value of $\mu_{\rm rel}$ can be derived from the *HST* astrometry alone. If we ignore the parallax and approximate $u_0 = 0$, we find $\mu_{\rm rel} = 10.85 \pm 0.16$ mas yr^{-1} and the position angle $\phi = 229.83 \pm 0.84$ deg (North through East). Allowing for a finite impact parameter makes no difference to $\mu_{\rm rel}$, changes ϕ by a mere 0.4 deg, and predicts the lens-source alignment a couple of months after the actual event, consistent within 1σ uncertainties. Including the parallax also has a negligible influence on the trajectory. Thus the Einstein radius can be estimated as $\theta_E = \mu_{\rm rel} t_E = 0.75 \pm 0.13$ mas.

The direction of the dimensionless parallax vector $\boldsymbol{\pi}_E$ is the same as the direction of the lens-source relative proper motion. The component $\pi_{E,\parallel}$ that points away from the projected position of the Sun is almost perfectly due East, since the event peaked on 21 September. Using results from § 4.4.2 and § 4.5.1 we can immediately estimate $\pi_E = |\pi_{E,\parallel}(\sin\phi)^{-1}| < 0.53$, and set an upper limit on the relative lens-source parallax,

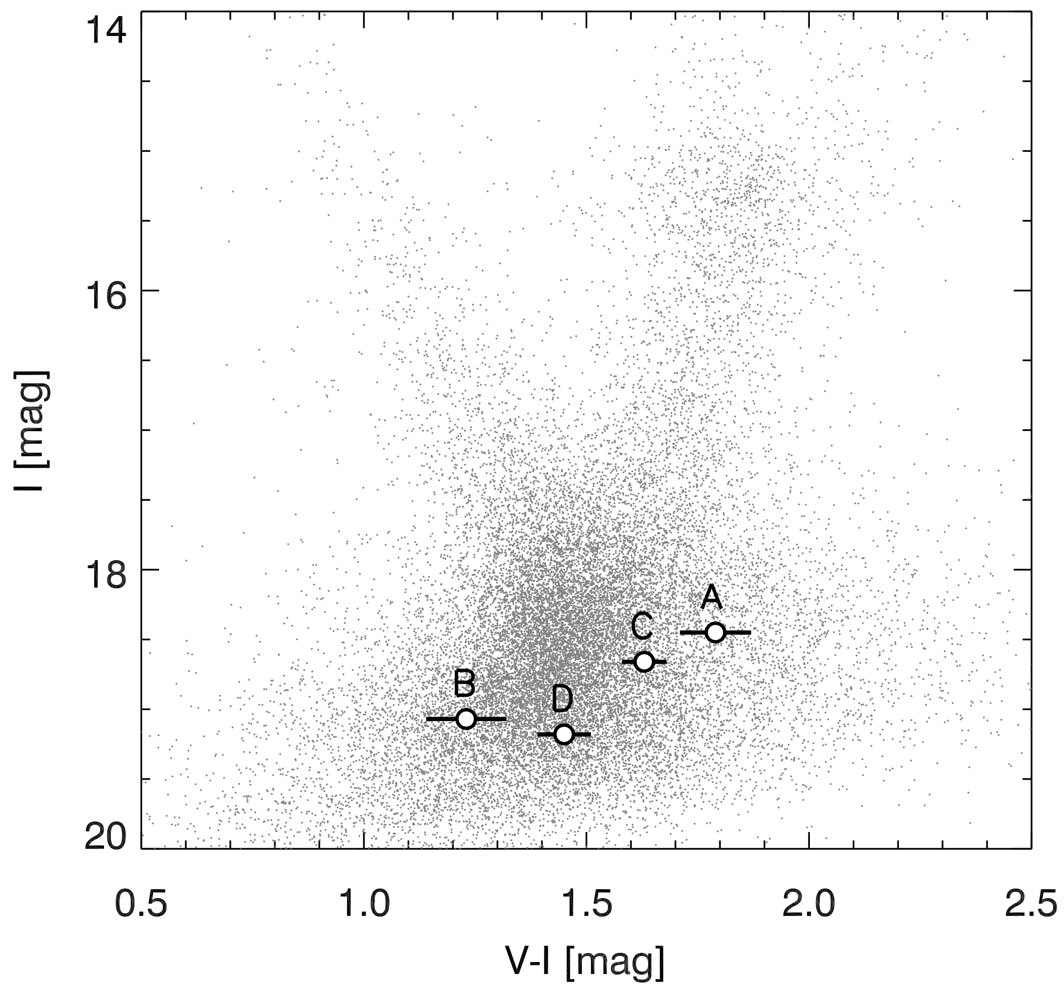

Figure 4.3: Colour-magnitude diagram (CMD) of stars around the MACHO-95-BLG-37 event location. The *HST* photometry of stars A – D from Figure 4.1 (open circles) is plotted against the average bulge and disk population along the line of sight (OGLE-II data; Udalski et al. 2002).

$\pi_{\rm rel} = \pi_{\rm E}\theta_{\rm E} \lesssim 0.3$ mas.

4.6 Microlensing scenarios and the lens mass

The value of the source colour derived in § 4.5.1 favours a scenario in which star A is the source and star B is the lens. However, as we show in this section, such an

Table 4.4: *HST* kinematics of stars A and B

Star	μ_l [mas yr^{-1}]	μ_b [mas yr^{-1}]
A	6.9 ± 0.3	-0.2 ± 0.3
B	-3.8 ± 0.4	3.7 ± 0.4

Proper motions are expressed in an average star reference frame as defined in Chapter 3.

arrangement is very unlikely in the context of the CMD (Figure 4.3) and proper motions measured relative to the Galactic bulge (Table 4.4). Although the extinction-to-reddening ratio in the direction of the event is abnormally low, the reddening anomaly cannot explain the conflict. After Sumi (2004), we adopt the reddening coefficient $R_\mathrm{VI} = A_\mathrm{V}/E_\mathrm{V-I} = 1.98$ and the total bulge extinction $A_\mathrm{V} = 1.54$. In the following discussion we consider both source star cases in some detail and then use the measurement of θ_E from § 4.5.2 to constrain the mass of the lens.

4.6.1 Blue lens scenario

First we attempt to reconcile all available data with the evidence in § 4.5.1 that the source is red. Given its red colour, star A is too faint to be a giant and too bright to be on the main sequence in the Galactic bulge. If it was a giant several magnitudes behind the bulge, it could in principle belong to the Sgr dwarf galaxy, but its observed proper motion is not consistent with Sgr (Ibata et al. 1997). More likely, star A is a dwarf in the foreground disk at a distance of ~2.5 kpc and behind most of the extinction. Then, if star B is indeed the lens, it must be in front of star A, and the only simple solution is that the lens is a nearby white dwarf at ~100 pc or so. Unfortunately, this exciting possibility is ruled out by the parallax constraint $\pi_\mathrm{rel} < 0.3$ mas (§ 4.5.2), as it predicts $\pi_\mathrm{rel} \approx 10$ mas.

The location of star A in the CMD is still marginally consistent with a faint subgiant on the far side of the bulge subject to ∼0.2 mag of extra reddening compared to the general population. But there is little support for that, since the CMD shows a compact red clump and indicates a very uniform extinction across this field (c.f. the extinction map of Sumi 2004). The observed kinematics would also be very unusual for this scenario with star A showing a 7 mas yr^{-1} disk-like prograde motion in the plane and star B moving at a ∼135° inclination. One could still argue that star B is a low metallicity halo subdwarf to explain its motion and dramatically increase the A_V prediction, but there is simply too much fine tuning to consider this a reliable solution.

4.6.2 Red lens scenario

The properties of both stars are much easier to explain if we dismiss for a moment the source colour evidence from § 4.5.1 and assume that star B is the source and star A is the lens. In this case star B is most likely in the bulge, where its absolute magnitude and colour would be approximately $M_\mathrm{I} = 3.6$ mag, $(V - I)_0 = 0.4$ mag assuming a red clump at $I_\mathrm{RC} = 15.3$ mag, $(V-I)_\mathrm{RC} = 1.8$ mag in Figure 4.3 and adopting $M_\mathrm{I,RC} = -0.2$ mag, $(V-I)_\mathrm{0,RC} = 1.0$ mag (Udalski 2000). So the source fits the properties of a metal-poor star near the turnoff point in the bulge, and the observed proper motion is fully consistent with this picture. Then star A must be the lens and can be placed on the main sequence at a distance of ∼4 kpc, where it would follow the Galactic rotation near the plane and move a few mas yr^{-1}. Again, the observed kinematics support this scenario.

4.6.3 The lens mass estimates

Any acceptable scenario for the lens must satisfy the constraint on microlensing geometry set by the measurement of the Einstein radius $\theta_\mathrm{E} = 0.75 \pm 0.13$ mas (§ 4.5.2). For the lens of mass M we have

$$M = \frac{\theta_\mathrm{E}^2}{\kappa \pi_\mathrm{rel}} \mathrm{M}_\odot, \quad \kappa \approx 8.14 \text{ mas}, \tag{4.4}$$

where $\pi_{\rm rel} = D_{\rm l}^{-1} - D_{\rm s}^{-1}$ is the relative parallax for the lens and source distances $D_{\rm l}$ and $D_{\rm s}$, respectively, in kpc. A given value of the source distance $D_{\rm s}$ sets a relationship between the lens mass M and the range of lens distances allowed by the error bounds of $\theta_{\rm E}$. Making a reasonable assumption about the luminosity class of the lens we can parameterize the photometric solutions in the same way, i.e. using the mass of the lens.

For each value of the lens mass M we use the appropriate mass-luminosity-color relation to obtain the absolute magnitude $M_{\rm V}$ and color $(V-I)_0$. Then using the *HST* photometry (§ 4.3.1) we estimate the reddening $E_{\rm V-I}$ through $E_{\rm V-I} = (V-I)_{\rm HST} - (V-I)_0$, and extinction $A_{\rm V}$ using the reddening coefficient $R_{\rm VI} = A_{\rm V}/E_{\rm V-I} = 1.98$ taken from the extinction map of Sumi (2004). Combined with the assumption of the source located at 8 kpc, each set of the above parameters allows a calculation of the lens distance $D_{\rm l}$ and extinction $A_{\rm V}$, which should not exceed total extinction of the bulge $A_{\rm V} = 1.54$ mag (see Fig. 4.4). We adopted the mass-luminosity relation for the main sequence from Schmidt-Kaler (1984) and the empirical color-magnitude relation defined by our polynomial fit to the *Hipparcos* CMD data in absolute magnitudes (*Hipparcos* catalogue; Perryman et al. (1997), Bessell (1990), compiled by I. N. Reid[4]). Our CMD locus for the main sequence is very close to the linear relation of Reid (1991) for $0.5\ {\rm M}_\odot < M < 1.0\ {\rm M}_\odot$ and is brighter by up to 0.3 – 0.5 mag outside this range. For comparison we also used a model grid of low metallicity hydrogen-burning stars with [Fe/H] = −1.0 from Baraffe et al. (1997).

The constraints on the lens resulting from the two major scenarios are plotted in Figure 4.4. The red solid lines show the photometric constraints for star A being the lens and the blue dashed lines are for star B being the lens. Each pair of lines corresponds to a range of solutions allowed by the ±0.1 mag uncertainty in stellar colours. The grey area is the geometric constraint based on the measurement of $\theta_{\rm E}$ (Eq. 4.4) assuming a Galactic bulge source. It is clear that a blue lens (star B) on the main sequence generally underpredicts the amount of extinction for a given distance. If the source is in the bulge, the microlensing constraint selects $D_{\rm l} = 4 - 5$ kpc, where the

---

[4] `http://www-int.stsci.edu/~inr/cmd.html`

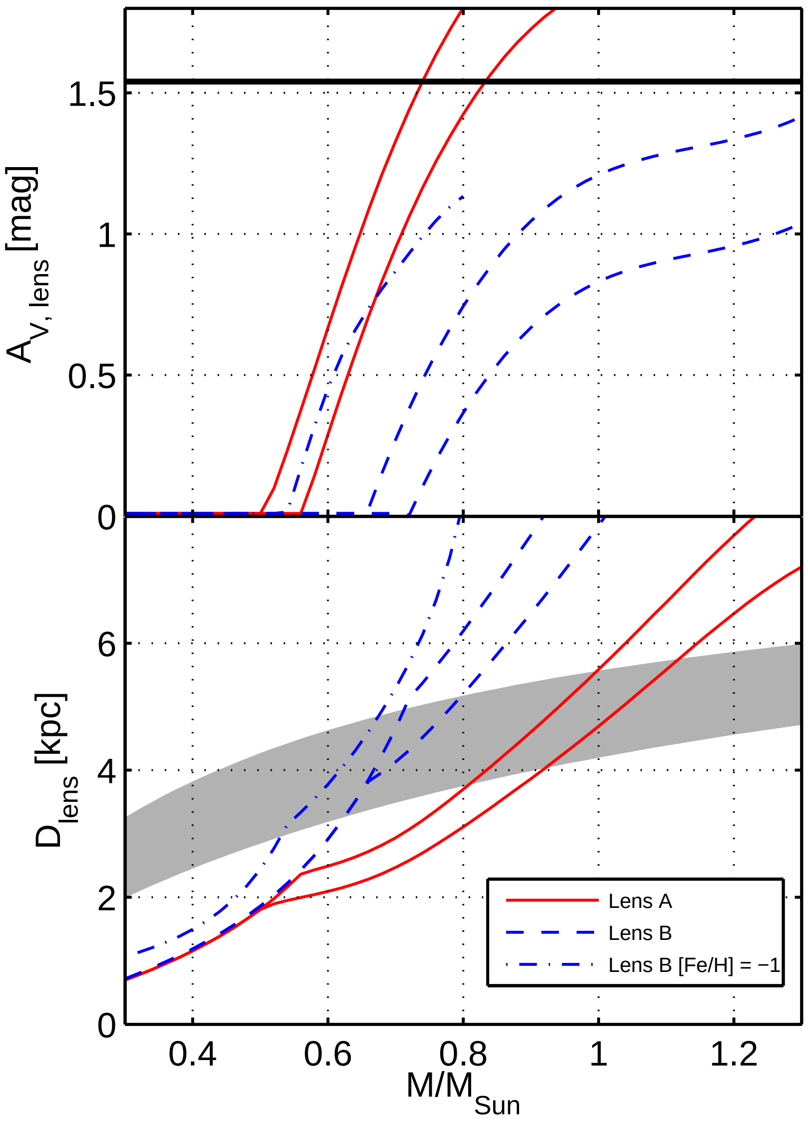

Figure 4.4: Photometric solutions for the lens distance and required extinction (top panel) as a function of the lens mass are shown. The gray area covers microlensing geometries for a source at 8 kpc allowed by the measurement of the Einstein radius $\theta_E = 0.8$ mas with 20% uncertainty. For each main-sequence model we show a pair of lines that reflects the ±0.1 mag uncertainty in stellar colors. A metal-poor model is also shown for star B (dot-dashed line). The top panel shows the required extinction to match the observed magnitude and color of the lens (§4.6.3); the thick horizontal line marks the total Galactic extinction ($A_V = 1.54$ mag) for the line of sight from Sumi (2004).

blue colour of the lens does not allow any significant extinction. Moving the source to a distance much larger than $D_\mathrm{s} = 8$ kpc shifts the range of D_l upward by a few kpc, but the problem with A_V remains. The blue dot-dashed line illustrates the effect of lowering the metallicity of star B to [Fe/H] = −1.0. This does solve the issue of extinction, but requires that the lens is a metal-poor subdwarf in the Galactic halo, or perhaps in the thick disk. Such a possibility is unlikely since the halo and thick disk contribute only a small fraction of stars within the Galactic disk. The mass and the distance of the lens are then $M \approx 0.6\mathrm{M}_\odot$ and $D_\mathrm{l} \approx 4$ kpc. The solution with a red lens (star A) is also not without a wrinkle, because in order to avoid overshooting the total extinction for the bulge we need to make θ_E about 20% larger and the lens ~0.1 mag bluer compared to the best estimates. Nevertheless, we can still find a consistent answer within 1σ uncertainties. In this scenario the lens is a main-sequence star with $M = 0.8 - 0.9\mathrm{M}_\odot$ (spectral type G5 – K0) at a distance of $D_\mathrm{l} \approx 4$ kpc.

4.7 Discussion

There is little doubt that we are directly observing the lens in the MACHO-95-BLG-37 event as it separates from a nearly perfect alignment with the microlensed source. However, the final identification of the gravitational lens is somewhat problematic. While the light curve models combined with the photometric data for individual objects favour a scenario with a blue lens and a red source, the opposite assignment is much more plausible in the context of the colour-magnitude diagram for the line of sight and the observed proper motions. In any case, the lens is a relatively bright star with a mass of ~$0.6\mathrm{M}_\odot$ or ~$0.9\mathrm{M}_\odot$. It is conceivable that additional factors such as binarity of stars affect the interpretation of the MACHO-95-BLG-37 event, but a conclusive resolution of the present conflict will require new data. High-quality spectroscopy would unambiguously pinpoint both the 3-D kinematics and the distance scale.

For the first time in a Galactic bulge event the lens and source have been directly resolved. This is an important addition to the sample of one consisting of the MACHO-

LMC-5 event. There are thousands of known Galactic bulge microlensing events and several dozen of those have archival *HST* pointings suitable for follow-up proper motion work. In our proper motion mini-survey (Chapter 3; Kozłowski et al. 2006a) we included 35 of those fields, and have already identified several more promising candidate lenses. As pointed out by Han and Chang (2003) and Wood (2006), in a few per cent of microlensing events toward the Galactic centre a lens with characteristic motion $\mu_{\rm rel} \lesssim 10{\rm mas\ yr}^{-1}$ may be detectable a decade after the microlensing episode. We are only beginning to probe directly the mass spectrum of the Galactic microlenses; however, we can expect that in the short term the progress will accelerate considerably due to availability of the archival and future *HST* pointings.

Acknowledgements

We thank Prof. Andrew Gould for many useful comments on this chapter. We also thank Drs. Thomas Vestrand, Łukasz Wyrzykowski and Martin Smith for helpful discussions.

5

The Optical Depth in OGLE–III

5.1 Abstract

Gravitational microlensing provides a new way of probing the mass distribution of the Galactic bar. It is sensitive to all massive objects along the line of sight, no matter whether they are luminous or not. Since the first microlensing events were found in 1993 (by MACHO, Alcock et al. 1993; EROS, Aubourg et al. 1993; OGLE, Udalski et al. 1993) there have been almost 4000 events detected until mid-2007. These events allow the construction of a statistically significant map of the optical depth τ as a function of the Galactic coordinates. There have been a dozen previous measurements of the optical depth (Table 5.1), which are in rough agreement with the present theoretical models. The third phase of the OGLE project (OGLE–III) will end in 2008 – 2009 and the whole data set will then be analysed. In this chapter the methodology of the optical depth derivation is presented, along with a description of the newly developed pipeline and image simulator. We apply these to derive, based on 4.2 years of the OGLE–III data, the optical depth toward one of the bulge fields, BLG206 ($l = 1.67^\circ, b = -2.68^\circ$): $\tau = (2.91 \pm 0.77) \times 10^{-6}$. The procedure developed here can in future be applied to derive a complete optical depth map, which will provide strong constraints on Galactic modelling. We also report the discovery of 11 new microlensing events.

5.2 Introduction

Paczyński (1986) first realised that observing millions of stars in the Galactic bulge and nearby galaxies (LMC, SMC and M31) would likely result in the discovery of a microlensing event (Paczyński 1986). He was quickly proved right (Alcock et al. 1993; Aubourg et al. 1993; Udalski et al. 1993). In the second half of the 1990s there were several microlensing surveys, finding dozens of microlensing events per year, mainly towards the Galactic bulge. These were EROS, MACHO, MOA and OGLE (see §1.2). It turned out that the 'standard' microlensing effect does exist as well as many closely related exotic effects such as the parallax effect (e.g. Cook et al. 1994; Smith et al. 2002), finite source-size effects (e.g. Gould 1994; Nemiroff and Wickramasinghe 1994; Witt and Mao 1994; Yoo et al. 2004), binary events (e.g. Axelrod et al. 1994; Mao et al. 1994; Udalski et al. 1994b) and the hottest topic nowadays, lensing by extrasolar planets (Mao and Paczyński 1991; Gould and Loeb 1992; Bond et al. 2004; Udalski et al. 2005; Beaulieu et al. 2006; Gould et al. 2006).

Observations of stellar fields toward the Galactic bulge reveal about two microlensing events per one million monitored stars at any given time ($\tau \approx 2 \times 10^{-6}$). However, the first calculations using non-barred models of the Galaxy predicted $\tau \approx 0.4 \times 10^{-6}$ (e.g. Paczyński 1991). The discrepancy between the observed values (Table 5.1) and theoretical models was partially solved by introducing a bar in the Galactic bulge, inclined at $\sim 25^\circ$ to the line of sight (e.g. Gerhard 2001; Rattenbury et al. 2007b). More sophisticated models of the Milky Way nowadays predict optical depths roughly in agreement with the observed values. Theoretical maps of the optical depth toward the Galactic bulge have been presented in Evans and Belokurov (2002) and Wood and Mao (2005). An observational map of the optical depth would further constrain the models of the inner parts of the Milky Way.

In the following sections the methodology of calculating the optical depth at pixel level is described. In contrast to most previous studies, where the detection efficiency ϵ was calculated based on injection of artificial microlensing events into a database of

Table 5.1: All measured optical depths toward the Galactic bulge.

Collaboration	Location (l, b)	Optical Depth $[\times 10^{-6}]$	N_* $[\times 10^6]$	N_{events}	T_{exp} [yr]	Source
OGLE–I	BW^{I}	~ 3.3	~ 1	12	3	Udalski et al. (1994c)
MACHO	(2.55°, -3.64°)	$3.9^{+1.8}_{-1.2}$	1.3	13^{II}	~ 2	Alcock et al. (1997)
MACHO	(2.68°, -3.35°)	$3.23^{+0.52}_{-0.50}$	~ 17	99	~ 3	Alcock et al. (2000b)
MACHO	(3.9°, -3.8°)	2.0 ± 0.4	~ 2.1	52^{II}	~ 5	Popowski et al. (2001)
MACHO	(2.22°, -3.18°)	$3.36^{+1.11}_{-0.81}$	17	99	~ 2	Popowski (2002)
MOA	(3.0°, -3.8°)	$2.23^{+0.38}_{-0.35}$	~ 230	28	2	Sumi et al. (2003)
EROS–2	(2.5°, -4.0°)	$0.94^{+0.29}_{-0.30}$	1.42	16^{II}	3	Afonso et al. (2003a)
MACHO	(1.5°, -2.68°)	$2.17^{+0.47}_{-0.38}$	6	42^{II}	~ 7	Popowski et al. (2005)
OGLE–2	(1.16°, -2.75°)	$2.55^{+0.57}_{-0.46}$	~ 1.5	32^{II}	4	Sumi et al. (2006)
EROS–2	(∼1°, |3.34|°)	1.68 ± 0.22	5.6	120^{II}	6	Hamadache et al. (2006)
OGLE–III	82 fields	2.19 ± 0.14	53	610	4	ŁW05 PhD thesis^{III}
OGLE–III	BW^{I}	1.89 ± 0.29	6.5	67	4	ŁW05 PhD thesis^{III}
OGLE–III	(1.67°, -2.68°)	2.91 ± 0.77	3.38^{IV}	26	4.2	this thesis

^{I} BW – Baade's Window (l, b) = (1°, -4°), ^{II} measured using Red Clump Giants,
^{III} Wyrzykowski (2005), ^{IV} see §5.5.1 for explanation.

light curves, I inject events into the original survey images. Having constructed these hybrid images (original images with injected microlensing events) it was possible to process them through the same pipeline – in the same way as for original images. This gives a better handle on one of the most vital ingredients of the optical depth – the detection efficiency ϵ. A detailed description of how the pipeline, simulation and calibration software work is presented below.

5.3 Data

The analysis here is based on the data collected between 2001 and 2005 by the OGLE–III group. The observations were made with the 1.3-m Warsaw telescope located in Las Campanas, Chile. In the focal plane of the telescope there is a mosaic CCD camera.

It consists of 8 chips, 2048 × 4096 pixels each, in total giving 8192 × 8192 pixels (Figure 5.2). It corresponds to a field of view of $35' \times 35'$ with one pixel sampling $0.26'' \times 0.26''$ of the sky. The OGLE–III project observes 267 stellar fields, which cover about 91 square degrees, containing about 200 million stars. Most of the bulge fields are spread over the ranges $-12^\circ \leq l \leq 12^\circ$ and $-6^\circ \leq b \leq 6^\circ$. So far OGLE–III has detected about 3000 microlensing events. More detailed descriptions of the telescope setup can be found in Udalski (2003).

The OGLE–III data are not publically available except for information about and light curves of, the detected microlensing events in the Early Warning System[1] (EWS; Udalski et al. 1994a). I was generously provided with the original OGLE–III images spanning the period 2001 – 2005 for nine fields (350 GB of data; private communication). Here I focus on one of these fields in order to demonstrate the method of the calculation of the optical depth. The field BLG206 was chosen for three reasons (Figure 5.2). Firstly, Stanek (1998) reported this field has the lowest extinction toward the Galactic bulge. The second reason was the availability of *HST* data for this field, which were of great use for correction of the number of monitored stars as well as for building the luminosity function used in the detection efficiency simulations. Finally, the most important reason for choosing this field is that it had the highest number of detected microlensing events by mid-2005 in the EWS – 48 events. Of these, only 17 events in this field passed our (more stringent) search criteria (§5.4.5); there were many more candidates. In addition we find 11 new microlensing events, not previously reported in the EWS. In total there were 3456 images analysed – 432 images per chip (31 GB in total).

5.4 Software

Various scripts, the reduction pipeline and the image simulator for the OGLE–III data were developed during this project. In this section the technical part is described in-

---

[1] `http://www.astrouw.edu.pl/~ogle/ogle3/ews/ews.html`

cluding the software that was developed for the optical depth calculation.

5.4.1 Templates

The observational strategy of any microlensing survey is based on many repeated observations of the same part of the sky. After years of observations a survey usually collects hundreds of images of the same stellar field. The most effective way of handling the images of very dense fields is by using the difference image analysis method (DIA, §1.4.6). This method is based on the subtraction of a top quality reference (template) image from all analysed images. The reference image is usually constructed from a dozen or so best quality images out of hundreds collected. It is crucial to construct a reference image characterised by a high signal-to-noise ratio, good seeing and no defects. In this section I describe the method of building such a template image.

Having ~400 images with roughly the same pointing on the sky it is hard to examine by eye all the images and choose the best ones. In this study a simple script was written, which was designed to search through all available images, and was able to choose the best ~30 for futher eye inspection. In the majority of the research presented here the DoPhot software was used. Running DoPhot on an image produces an output file consisting of information about all the detected stars. This includes the instrumental magnitudes, the PSF size and shape, and the background. For each image these output files were analysed by a script software. First, the median parameters of all stars were constructed; they were $FWHM_x$, $FWHM_y$ – size of the PSF, ϵ – expressing the ellipticity of the PSF and *bkg* – the background. Using these parameters I define a simple function expressed as

$$T = FWHM_x + FWHM_y + \alpha \times \epsilon + \beta \times bkg, \tag{5.1}$$

where $\epsilon = abs\left(1 - FWHM_x/FWHM_y\right)$, and $\alpha = 20$ and $\beta = 0.0025$ are the ellipticity and background coefficients, respectively. The parameters α and β are chosen to make each term of the above equation roughly equal. It is important to built the template image having a circular PSF. Therefore, the candidate images had to first satisfy the criterion $\epsilon \leq 0.1$.

It is obvious that the best candidate images are characterised by the smallest possible values of T. All images were processed through the script calculating the function T. The best 30 images were further inspected by eye. After this step there are usually 15 – 20 images remaining for building the template. The successful candidate images were co-registered using the standard DIA tasks as and , then re-sampled onto one common reference frame using and finally stacked together ( ) into one high quality template image (§1.4.6).

5.4.2 Pipeline

Having built the templates it was time to analyse all the images from each series of 432 images. To do so a script calling other executable programmes – a pipeline – was constructed. The main goal of the pipeline is to deliver a database of light curves. One can think of the pipeline as a black box, where on one side we input the images and on the other side we get the output database of light curves.

Since the original OGLE–III pipeline is not available to the open public, I developed my own pipeline, which resembles the original one. The core of the pipeline is a set of DIA codes developed by Woźniak (2000), as described in §1.4.6.

The analysis starts with the set of 2048 × 4096 (single chip) images, which are supposed to point in the same direction on the sky. In practice, it is difficult to always point the telescope in exactly the same direction, so there are shifts of up to 100 pixels between the images. All images have to be co-registered in the template's reference frame. To do so, a task called is used, which calculates rough shifts between the images and is able to find the shifts with an accuracy of ~1 pixel.

The full images are too big to be analysed in one go. They were cut into 4 × 8 preliminary chunks of 512 × 512 pixels each (to be precise they are 552 × 552 pixels, including 20 pixels of margin), according to the shift information from . Next, once again each sub-image of 552×552 pixels is precisely analysed. Several hundred bright stars are detected with in the area of the analysed image as well as in the corresponding area of the template image. Another task precisely identifies the same stars on the two images; the identification radius is 3 pixels. Next, the task finds a transformation between the two lists of stars using n^{th}–order polynomials. Having found coefficients of the transformation we resample an analysed image onto the template reference frame using . We repeat this procedure for all analysed images.

D P is run on the template chunk. It detects stars and provides the information on their positions and magnitudes. Magnitudes are recalculated to standard magnitudes according to a proper calibration coefficient. Having the co-registered sub-images with the template the task was run. It subtracts the template from all analysed images. After the subtraction procedure the task is started, which measures the residual flux at all positions detected previously by D . The calibration of the residual fluxes of stars with the D P fluxes is done. For each observation the residual flux of a star is added to the corresponding baseline flux of the star from the D P output – this is how the database of light curves is built. It consists of the information about each star including the time of the observation, the magnitude and its uncertainty. The information regarding all positions on a chunk image and the whole template are stored as well. We regard these data as the ‘main database’.

There is a second database of light curves produced comprising all genuine variable objects. In principle this is done in exactly the same way as for the main database, except that the variable objects are searched for directly on the subtracted images by the task . It is important not to miss any potentially interesting microlensing events. There might be a microlensing episode ongoing on a very faint star not detected in the main database. In this case the residual flux is assigned to the nearest detected star within 3 pixels, or if there is no star in this area, then is an artificial star is created in the ‘variable database’ with the baseline flux of 10 counts ($I \approx 20$ mag).

Empirically tested parameters of the pseudo-Gaussian PSF, best representing the

Table 5.2: Calibration parameters of the template images.

Field.Chip	ΔI^* [mag]	FWHM [pixel]	FWHM [arcsec]	N_{stars}	Background [counts]
BLG206.1	27.381	3.265	0.85	9993	816.12
BLG206.2	27.351	3.099	0.81	14070	901.42
BLG206.3	27.380	3.130	0.81	14864	826.48
BLG206.4	27.229	3.155	0.82	11928	923.78
BLG206.5	27.250	3.167	0.82	13568	856.71
BLG206.6	27.233	3.241	0.84	11327	836.97
BLG206.7	27.201	3.109	0.81	13124	898.59
BLG206.8	27.127	2.993	0.78	12342	854.86

* where $m_{\mathrm{OGLE-III}} = m_{\mathrm{DoPhot}} + \Delta I$.

OGLE–III database output are $\beta_4 = 0.4$ and $\beta_6 = 0.2$ (see Equation 1.19). The calibration of the templates is summarised in Table 5.2.

5.4.3 Simulation of the OGLE–III images

The simulation software was designed to produce hybrid images as similar to the original ones as possible. The goal was to inject artificial microlensing events into the original survey images. This is, firstly, a relatively fast solution as we do not have to populate the images with stars, and secondly, all image defects, variable stars and cosmic rays are already there. It would be very difficult and time consuming to simulate the images from scratch including all real effects.

Before starting a simulation all the parameters of the images are measured. Similarly to the procedure described in §5.4.1, the median sizes of the PSF, $FWHM_x$ and $FWHM_y$, the PSF position angle ϕ and the background (we assume here that the PSF does not change spatially within 512 × 512 pixels) are measured. Also a median difference of magnitudes for 400 stars on each image and the template is derived. This

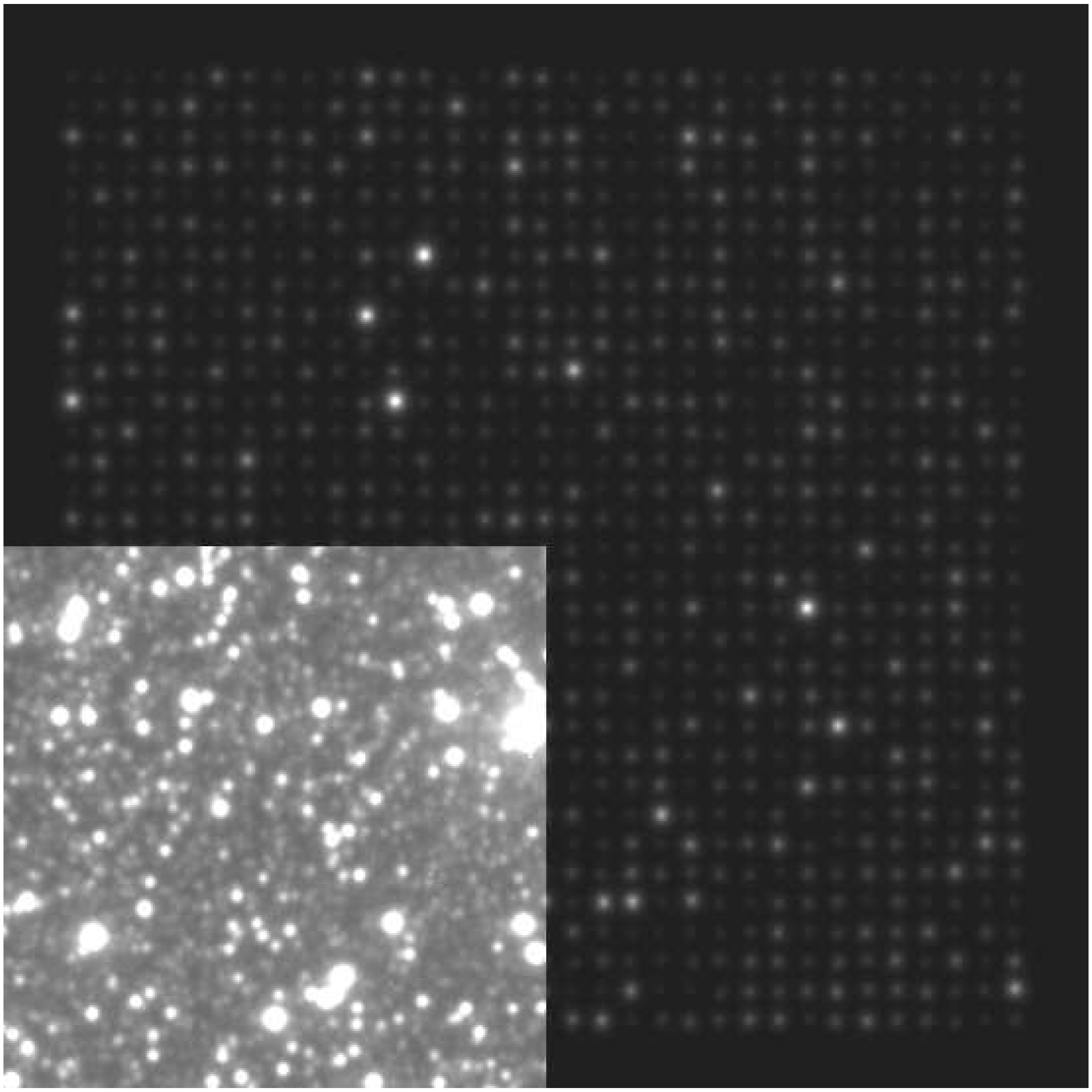

Figure 5.1: A single frame from the simulations is shown. The frame has a size of 552 x 552 pixels. A grid of microlensed sources (33 x 33) separated by ~15 pixels is injected into each frame. In the final step the original OGLE-III image is added to the simulated sources; the inset shows a small patch of 276 x 276 pixels.

accounts for any changes in the brightnesses of stars due to, for example, clouds or changing zenith angle and allows for a proper injection of the magnitudes of stars into the images. All this information (plus Heliocentric Julian Date – HJD) are stored in a log file. Using this information it is possible to calculate the amplification for a given moment in time for each microlensing event. The simulation software uses all the information derived from the original images to inject proper PSFs of the microlensed sources into the images.

From the original OGLE–III images (resampled onto the same reference frame) there are small sub-images of 552×552 pixels cut-off with an 'active area' of 512×512 pixels in the centre. In each of the 432 real sub-images a grid of 33×33 microlensed sources is injected (Figure 5.1). All microlensed sources are separated by 15 pixels, plus a random shift is drawn from the Gaussian distribution with $\sigma = 0.5$ pixel – to account for pixel phase effects.

In each simulation[2] the parameters of the artificial microlensing events were assigned. The magnification peak parameter was drawn from a flat distribution spanning the observation period (HJD= 2452125.68 − 2453659.54). The impact parameter was drawn from a flat distribution of range $u_0 = 0-1$. The magnitudes were drawn from the joint OGLE–III and *HST* luminosity function (Figure 5.3), with a limiting magnitude of $I = 22$ mag. The timescales of all 1089 microlensing events for each simulation are the same (the range is discussed in §5.5.3). There is no need to assign the blending parameter f_s as we get it for free by injecting our events into an already dense stellar field.

5.4.4 Calibrations

In this section the basic calibration procedures used in the optical depth calculation process are described.

Calibration of D P output

The main issue for calibration of the simulated data is to investigate whether the β-parameters (see §1.4.1) of the pseudo-Gaussian profile are properly chosen. Having chosen a set of β-parameters the D P software is run on an analysed image, producing an output file. The positions of stars from this file are cross-correlated with the

---

[2] Two simulation movies can be watched at `http://science.simkoz.com/OGLE3tau/`

original OGLE–III template positions. The differences between the output and OGLE–III magnitudes can then be plotted. The residual magnitudes should show a ‘perfect’ linear trend of the type $I_{\mathrm{OGLE-III}} = I_{\mathrm{DoPhot}} + \Delta I$ for most of the range of magnitudes. As the brightest stars are not severely blended and have high signal-to-noise ratios there should be a pretty good linear trend visible. The spread should be of less than ~0.04 mag for the stars brighter than $I \leq 15$ mag and not more than ~0.5 mag for stars of $I \approx 19$ mag. Any deviation from linearity means that the correct set of β-parameters is still to be found. DoPhot should be re-run with different β-parameters until the analysis arrives at a linear trend.

It was empirically checked that the correct parameters for the analysed template images are $\beta_4 = 0.4$ and $\beta_6 = 0.2$. The calibration parameters of the BLG206 field are presented in Table 5.2.

Double run of DoPhot

In order to derive accurate magnitudes from DoPhot, proper values of the PSF shape and the background in the input parameter file need to be set. The best way of finding these parameters is a double run of DoPhot. The first run is done with a rough estimation of the parameters. In the output file the corrected parameters are stored, however, the magnitudes are incorrect. To correct the magnitudes, the median values of all the output parameters are calculated and applied as the input parameters during the second run of DoPhot. The correct parameters do not change during the second run, but the magnitudes are now recovered correctly.

5.4.5 Search engine

The search engine (along with supporting documentation) was provided by Dr. Łukasz Wyrzykowski from the OGLE collaboration and is partially based on Sumi et al. (2006), it was not built as a part of this thesis. Only the essential parts of the algorithm based on Wyrzykowski (2005) are described. There are several levels of cuts, which can be summarised as:

- Removal of outliers: A measurement is classified as an outlier when its value deviates by more than three standard deviations from a model ($\sigma > 3$) but for both adjacent measurements $\sigma < 2$. This procedure usually removes a couple of points from each light curve.

- Every light curve showing a variability $\sigma_{\mathrm{rel}} > 1.3$ was further analysed, where σ_{rel} is defined as

$$\sigma_{\mathrm{rel}} = \frac{\sigma_{<I>}}{< \Delta I >}, \tag{5.2}$$

$$\sigma_{<I>} = \sqrt{\frac{1}{N(N-1)}\left[N\sum_{i=1}^{N} I_i^2 - \left(\sum_{i=1}^{N} I_i\right)^2\right]}, \tag{5.3}$$

$$< \Delta I >= \frac{\sum_{i=1}^{N} \Delta I_i}{N}, \tag{5.4}$$

  where N is the number of data points on a light curve, and I_i and ΔI_i are an i^{th} measurement of the magnitude and its uncertainty, respectively.

- For each data point on a light curve we define two windows A and B. Window A is centered on an analysed point and spans half of the period of the observations. Window B spans the other half of the observations. The last point of a light curve is followed by the first one in order to assure the continuity of both windows. For each measurement its weight is calculated as

$$\sigma_i = \frac{I_{med,B} - I_i}{\sqrt{\Delta I_i^2 + \sigma_B^2}}, \tag{5.5}$$

  where $I_{med,B}$ is the median magnitude of window B, I_i and ΔI_i are as described above, and σ_B is the standard deviation in window B.

- Next, we search for brightening episodes. They are defined as a clump of at least five adjacent points for which $\sigma_i \geq 1.6$, or if one of these points violates this criterion we further require that at least three points should have $\sigma_i \geq 3$.
- Having recognised all brightening episodes, microlensing events are then searched for. This is done by satisfying the following criteria: the number of peaks is 1 – 3, the maximum deviation $\sigma_{max} \geq 6$ and the sum of the five nearest σ_i to σ_{max} is greater than 20.
- In the final step the standard microlensing model is fitted to all candidate light curves. A candidate is recognised as a microlensing event if the reduced χ^2 for the whole light curve is less than 3 and for the peak ($t_{\mathrm{peak}} \pm 3t_{\mathrm{E}}$) the reduced $\chi^2 \leq 2.5$. In addition the peak has to appear within the period of the first and last observation.

5.4.6 The catalogue of light curves

As a result of running the pipeline on the set of images two output databases of light curves are built: one for stars detected by D P on the original images and one for variable objects detected by G on subtracted images. Since all calibrations are made within the pipeline, the resulting light curves are already calibrated to the standard photometric magnitudes. They are, however, not extinction-corrected. There were 170,000 – 210,000 stars found and measured per CCD chip of the BLG206 field, which gives a total of ~1.5 million light curves.

The output files include three columns (HJD, I–magnitude and the I–magnitude uncertainty). All the measurements of an i^{th} star were stored before/above all the measurements of the $i^{\mathrm{th}} + 1$ star within a file. All measurement problems were marked with the error code 99.99. The light curves of 26 microlensing used in this study are presented in Figures 5.5 – 5.8. Sample light curves of the variable stars are shown in Figure 5.12.

5.5 Calculation of the optical depth

The derivation of the optical depth τ in this chapter is based on the widely accepted formula (e.g. Sumi et al. 2006)

$$\tau = \frac{\pi}{2N_{*}T_{\mathrm{exp}}} \sum_{i}^{N_{\mathrm{events}}} \frac{t_{\mathrm{E},i}}{\epsilon(t_{\mathrm{E},i})}, \tag{5.6}$$

where N_{*} is the total number of stars a given experiment monitors, T_{exp} is the duration of the experiment, $t_{\mathrm{E},i}$ is the Einstein radius crossing time of the i-th event, and $\epsilon(t_{\mathrm{E},i})$ is the detection efficiency for the timescale.

From the above equation, it is clear that there are at least three factors which should be considered carefully. These are the number of monitored stars, the timescale of an event and the detection efficiency for that timescale.

5.5.1 The number of monitored stars

The faintest detected stars (blends) in the OGLE–III survey are of $I \approx 20.5$ mag, with the peak of the luminosity function at $I = 18 - 19$ mag. There have been ~3000 microlensing events detected by OGLE–III before August 2007. In about 200 cases the source star was fainter than $I = 20.5$ mag, and ~1200 events happened on source stars fainter than $I = 19$ mag. These faint stars are mostly blends of much fainter stars, which would be undetectable on their own in this experiment (especially for $I > 20.5$). However, if an event occurs on a very faint source star, a small impact parameter may allow this star to appear above the threshold level for detection. So in principle for small impact parameters, stars much fainter than the threshold level can be detected. In practice if the *HST* and OGLE images are compared it can be seen that each OGLE star (blend) is ‘made of’ a number of fainter *HST* stars (e.g. Figure 2.1). Empirically it was checked in the EWS that source stars are not fainter than $I \approx 22$ mag. In the following study we adopt $I = 22$ mag as the limiting magnitude.

Since the star counts in the OGLE–III database are found for the stars (blends) brighter than $I \approx 20.5$ mag, the number of monitored stars needs to be corrected since

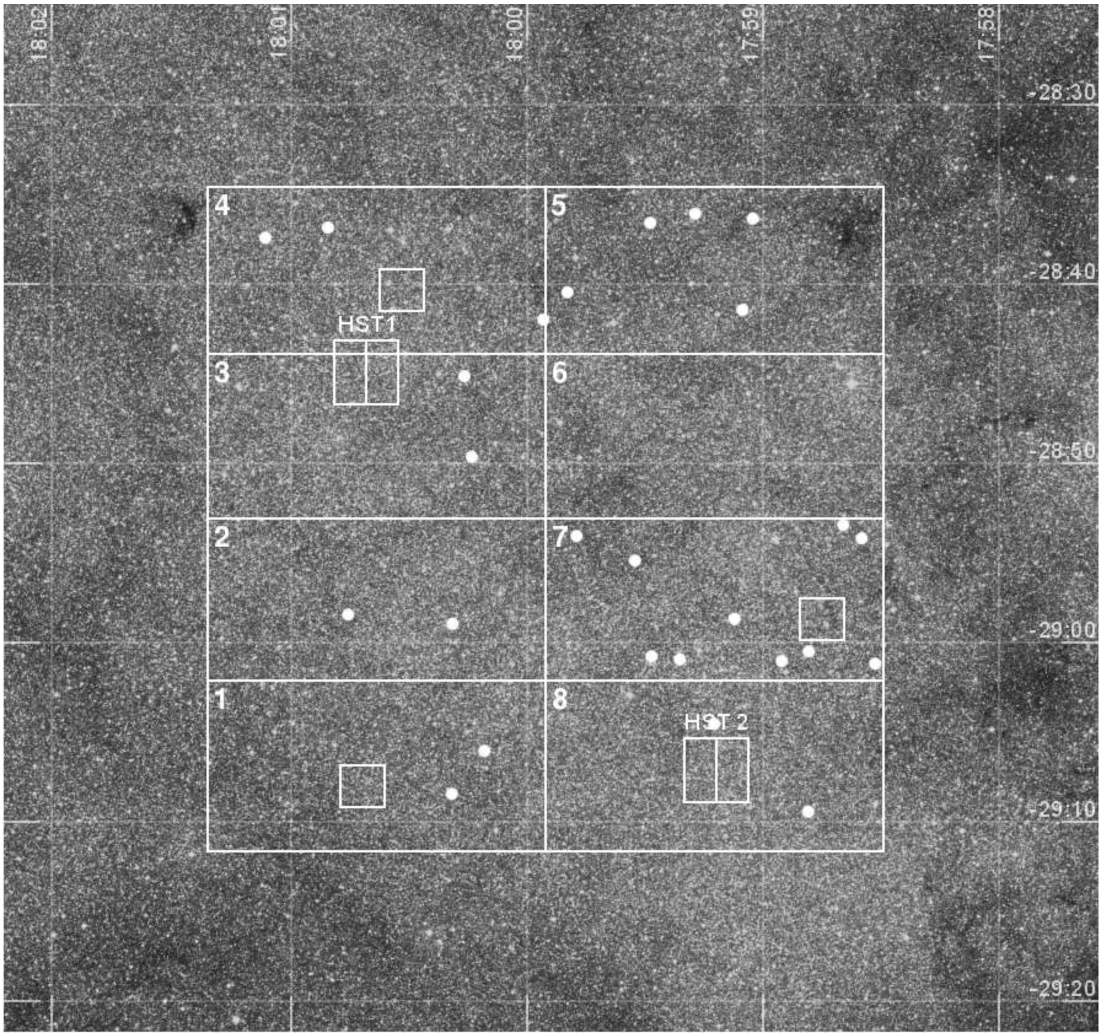

Figure 5.2: Location of the BLG206 field from the OGLE–III survey on top of the Digital Sky Survey image is shown. There are eight BLG206 chips' contours superimposed on the image as well as the two *HST*/ACS/WFC locations (marked as HST1 and HST2), three locations for which the detection efficiency ϵ was calculated (squares) and 26 positions of the microlensing events used in this study (dots). The OGLE–III fields are aligned to equatorial coordinates; the RA and Dec grid is marked. The field of view is $35' \times 35'$.

any faint star in a blend can be microlensed. To account for blending, on the *HST* images, stars brighter than $I \approx 22$ mag within each OGLE blend are counted. To do so we use two *HST* fields overlapping with the chosen BLG206 field. They are marked as HST1 and HST2 in Figure 5.2. These two images were taken from the HST archive, where they can be found as *J8Q603011* and *J8Q602011*, respectively. Both images were taken with the ACS/WFC camera in the $I-$band and the exposure time was 1044s.

In the above exercise it is found that the number of monitored stars should be multiplied by 2.120 in the field HST1 and by 2.363 in the field HST2. We adopt a conversion number of 2.120 for chips 2, 3, 4, 5 and 2.363 for chips 1, 6, 7, 8. This gives the statistical number of monitored stars as 3,379,937 in the field BLG206.

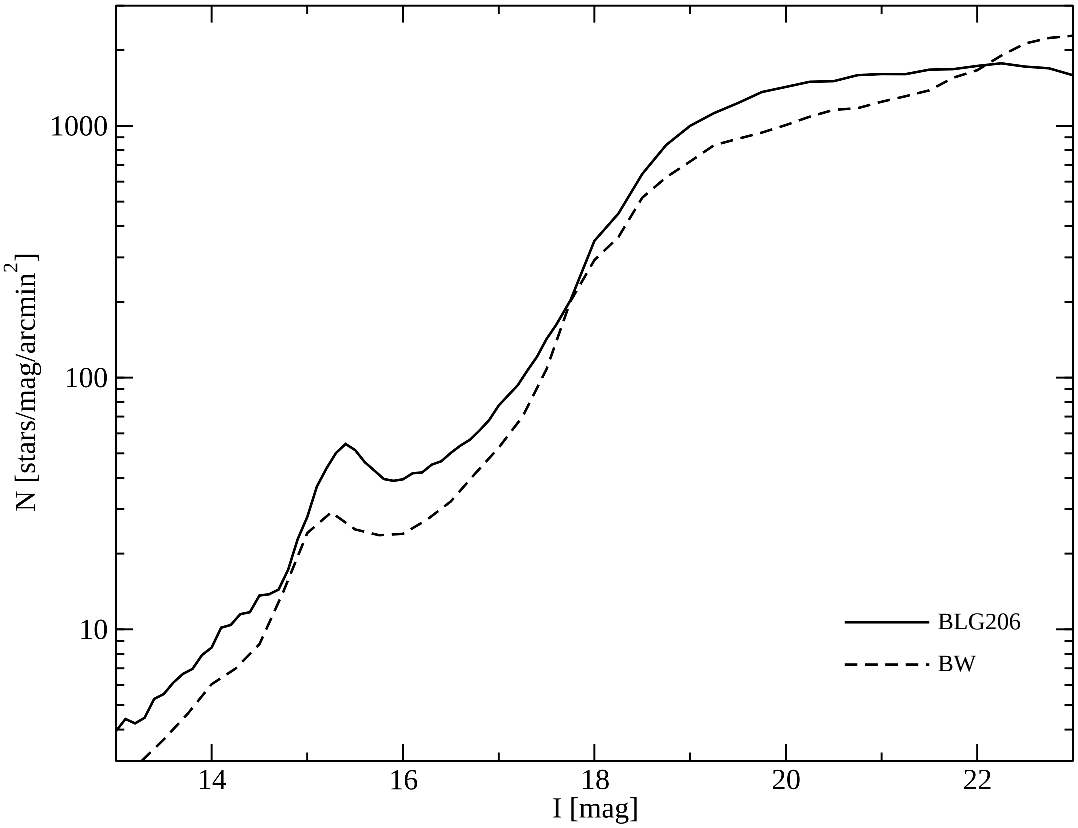

Figure 5.3: Joint the OGLE–III and HST luminosity functions for Baade's Window (dashed line) and BLG206 (solid line) are shown. The luminosity function for BLG206 was derived from the fields marked in Figure 5.2 as HST1 and HST2 and was used for calculation of the detection efficiency ϵ (§5.5.3).

5.5.2 The timescale of an event

All ground-based images of crowded stellar fields, such as the Galactic bulge, are strongly affected by blending, where a ‘star’ in a ground-based image in fact consists of several unresolved stars (Chapter 2, Figures 2.1, 2.2, 3.4 and 4.1). The modelling of a microlensing light curve is usually degenerate due to source confusion, which prevents an accurate measurement of the event timescale (Woźniak and Paczyński 1997), and as a result the optical depth. Recent studies of the optical depth toward the Galactic bulge were done using the Red Clump Giants (RCGs), which are relatively bright and therefore less affected by blending. Sumi et al. (2006), however, found ~38% of the RCGs were blended with fainter components. Having found only 26 microlensing events, which occurred on mainly faint and therefore strongly blended sources, we cannot choose the analysis of relatively unblended RCGs. We, therefore, use all the available microlensing events for the optical depth calculation.

5.5.3 Detection efficiency

In order to calculate a robust optical depth from the OGLE–III data it is also crucial to evaluate the detection efficiency $\epsilon(t_{E,i})$. The simulation software was used (described in detail in §5.4.3) to produce the hybrid OGLE–III images.

The simulator is run on the images from three different parts of the field BLG206 (chips 1, 4 and 7). There were 27 simulations performed for each location. The simulation were run for $\log(t_{\rm E}) = 0.4 - 2.7$, which gives the range $t_{\rm E} = 2.5 - 500$ days. From $\log(t_{\rm E}) = 0.4$ to 1.1 the simulations were spaced at intervals of 0.1 and were run twice to increase the statistics for these timescales. From $\log(t_{\rm E}) = 1.1$ to 2.7 the simulations were spaced at intervals of 0.2 and were run just once. The magnitudes within the grid were shuffled for each simulation.

The simulated images were then processed through the same pipeline described in §5.4.2. The output databases of the light curves were analysed with the same search engine (§5.4.5; a sample of artificial microlensing events is shown in Figure 5.11). In the next step, positions of the recovered microlensing events from the database were cross-correlated with the input positions. As some of the brighter events' PSF wings were spread over a substantial area causing many stars around to mimic microlensing events, the nearest output star with respect to the injected position was looked for. The cross-correlation radius of three pixels plus the nearest neighbour criterion were used to remove all spurious 'ghost' microlensing events. The resulting detection efficiency curves are shown in Figure 5.4.

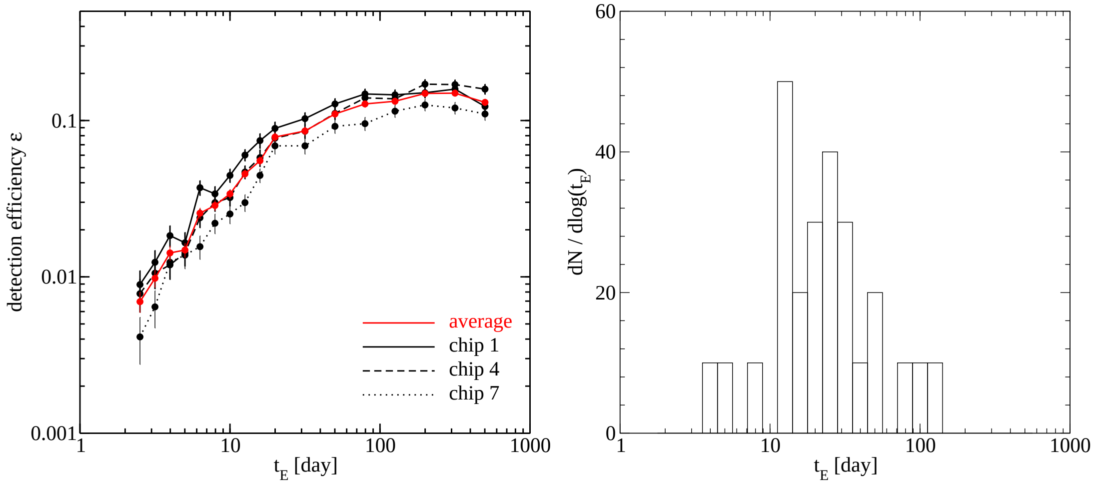

Figure 5.4: Detection efficiencies (left panel) for three locations in the BLG206 field (calculated in the small squares in Figure 5.2) and the distribution of timescales (right panel) are shown. In the left panel the solid black line marks the detection efficiency for chip 1, the dashed line corresponds to chip 4, the dotted line to chip 7, and the solid red line marks the average detection efficiency for all three fields. The simulation of the detection efficiency was done to a limiting magnitude of $I = 22$ mag.

There are hints that there may be a correlation between the detection efficiency and stellar density (or extinction). From Figure 5.4 one can see that detection efficiency drops with increasing number of stars; there were 5642, 5767, and 5897 stars for the sub-areas of chips 1, 4 and 7, respectively (marked with the small squares in Figure 5.2). The mean deviation of the three curves from the average one for all the timescales is about ±20% (see the left panel of Figure 5.4). At the most likely timescales (see the right panel in Figure 5.4), the average deviation is smaller, about

15 – 18%. If we adopt any individual efficiency curve, the resulting optical depth differs by about ±20% from the value that we obtain using the average efficiency curve.

Alcock et al. (2000b) reports a similar analysis as presented in this chapter. The artificial microlensing events were injected into simulated images down to a limiting magnitude of $V = 23$ mag. The fields analysed in Alcock et al. (2000b) are of rather low extinction; field 104 of their study overlaps with the BLG206 field. The comparison of the MACHO detection efficiency curve with the average one from this study shows the same dependence with a median ratio of 1.34.

5.5.4 The microlensing events for the optical depth

There are 28 microlensing events found in the field BLG206 meeting the given criteria. Two of them are binary events (see Figure 5.9) and are removed from our sample of the single lens events. The remaining 26 microlensing events are shown in Figures 5.5 – 5.8 and the fitted parameters are summarised in Tables 5.3 and 5.4. We find the fraction of binary events of 7% to be in agreement with previous studies where it was estimated as 3 – 8% (e.g. Jaroszyński 2002; Jaroszyński et al. 2004). Following the analysis of Sumi et al. (2006) we adopt that a binary event has a timescale of $\sqrt{2} \times (t_\mathrm{E}$ of a single lens event) – assuming the binary lens consists of two stars having the same timescales. In the final step the optical depth measured on the single lens events is multiplied by $\sqrt{2} \times n_\mathrm{binary}/(1 - n_\mathrm{binary}) = 1.106$, where n_binary is the fraction of binary events.

Our selection criteria are more stringent than the OGLE–III ones. In total there are 1349 microlensing candidate light curves (the 'preliminary list') passing all the criteria except the chi-square ones (§5.4.5). The final list of candidates which pass all the criteria consists of 64 microlensing events. After removing the 'ghost' events our sample contains 26 single and 2 binary events. Out of the 31 EWS missing events, 25 are found in the preliminary list of candidates. They do not make it to the final list because of a high χ^2 caused by either a small scatter from a standard microlensing light curve, due to for example variability of a source or blend (Wyrzykowski et al. 2006) or/and underestimated error bars. It is a common problem for both the OGLE–III and our database (and in general for DIA-based light curves) that the error bars for bright microlensing events ($I < 14.5$ mag) are underestimated, causing unacceptably high χ^2 (see Figure 5.10).

5.5.5 Results

In the previous sections all the ingredients necessary for the optical depth calculation were presented. Summarising all of them, they are

- the number of monitored stars $N_* = 3,379,937$ (§5.5.1),
- the experiment exposure $T_{\rm exp} = 1533.86$ days,
- the microlensing events' timescales $t_{E,i}$ (presented in Tables 5.3 and 5.4),
- the detection efficiency curve (shown in Figure 5.4).

Using equation 5.6 and the average detection efficiency we find optical depths of

$$\tau_{\rm BLG206} = (2.91 \pm 0.77) \times 10^{-6} \quad \text{and} \quad \tau_{\rm BLG206} = (3.22 \pm 0.85) \times 10^{-6} \tag{5.7}$$

for the single lens events, and including binary events, respectively. The measurement of τ is done toward the field BLG206 centered at $(l, b) = (1.68°, -2.67°)$. The uncertainty of τ is calculated based on the equation given by Han and Gould (1995):

$$\frac{\sigma_\tau}{\tau} = \sqrt{\frac{\eta}{N_{\rm events}}}, \qquad \eta = \frac{< t_E^2 >}{< t_E >^2}. \tag{5.8}$$

For the 26 presented events $\eta = 1.83$, which gives a relative error of ~27%. To reduce the relative error to 20% or 10% we would need a sample of 46 or 183 events with similar η, respectively.

Applying a simple error propagation method we find an error bar of $\pm 0.26 \times 10^{-6}$ for the average detection efficiency curve and taking into account the covariance between all parameters (using any of the single detection efficiencies) we find an error bar of $\pm 0.86 \times 10^{-6}$ for the 26 single lens events.

5.6 Discussion and future work

The major improvement of this study over previous ones is the development of the simulator of hybrid images. It injects the artificial microlensing events into the original images, which are then analysed by the pipeline. This procedure treats all the real effects such as variable stars, cosmic rays, etc., present in the data.

Another new development is usage of the *HST* archival data for building the luminosity function for a given field as well as the correction of the number of monitored stars.

The search engine used in this chapter needs further investigation to answer the question of why only 17 out of 48 microlensing events found in the EWS passed our stringent criteria. Another 25 were on the preliminary list of candidates, indicating that the criteria in the last stage of the search have to be fine-tuned in order to maximise the event detection rate. This is particularly crucial if one wants to minimise the uncertainty of τ. It is estimated that lowering the search criteria, and/or rescaling the error bars for bright events, we should find 50 – 60 events in this field. The results presented here, however, are valid and correct since the same search criteria were applied to both the real and hybrid images.

The detection efficiency curves are different for each location on the sky. From Figure 5.4 there are hints that the detection efficiency drops with increasing stellar density (in fact with decreasing extinction). This problem, however, has not been studied in this chapter. It would be optimal to calculate the detection efficiency for each event's timescale. The average detection efficiency curve, which was used in this study for all events, likely skews the optical depth value. Applying any of the three single detection efficiencies presented here to the τ equation changes the derived optical depth by ± ∼20%.

The presented value of τ stays in rough agreement with previous studies (Table 5.1). The two nearest fields are those presented in Popowski et al. (2005) and Sumi et al. (2006). These fields are located at $(l, b) = (1.5^\circ, -2.68^\circ)$ and $(l, b) = (1.16^\circ, -2.75^\circ)$, with the $\tau = 2.17^{+0.47}_{-0.38} \times 10^{-6}$ and $\tau = 2.55^{+0.57}_{-0.46} \times 10^{-6}$, respectively. Wood and Mao (2005) used the G2 Galactic bulge model of Dwek et al. (1995), with the method of Han and Gould (2003), to predict the optical depth in this region; $\tau = (2.34 - 2.54) \times 10^{-6}$. Wood (2007) compares the above mentioned fields, with the G2 and E2 bulge model of Dwek et al. (1995). He predicted $\tau = (2.14 - 2.19) \times 10^{-6}$ for the G2 model and $\tau = (1.57 - 1.61) \times 10^{-6}$ for the E2 model. The result of the investigation here is in agreement ($\sim 1.5\sigma$) with the MACHO and OGLE–II results, as well as with the predictions of Wood and Mao (2005) and the G2 model prediction of Wood (2007), but is about a factor of two higher than his prediction with the E2 model.

In principle all the procedures presented here can be repeated for all OGLE–III bulge fields and those in the LMC and SMC. The ultimate goal is the analysis of the whole OGLE–III data set in 2008 – 2009, when this ongoing phase of the project will be completed. An observation-based map of the optical depth is feasible in the context of the amount of collected data. It is likely, however, that the map will not be as constraining as it is intended to be. The error bars on the optical depth in the central bulge fields will likely stay at the level of ∼15% and increase to ∼40% at ∼10° from the Galactic centre. It will be enough to distinguish between which of the existing models better represents the inner part of the bulge. The predicted differences in this region are of ∼50% between the models of Dwek (G2 and E2), Freudenreich and Binney (Evans and Belokurov 2002; Wood and Mao 2005). It is doubtful that the present data will be able to put constraints on the outer parts of the bulge. To add further confusion to the picture, the optical depths based on Red Clump Giants are systematicaly lower than those based on all events. It is partially understood as the effect of blending but the issue has not been entirely solved (see e.g. Wood 2007). Smith et al. (2007), however, show that the derived optical depths for all microlensing events should be increased by several per cent (~5% in our case) due to the effects of blending.

There will be only a couple of hundred Red Clump Giants (spread over many fields) detected in the OGLE–III database. This is statistically speaking not enough to put constraints on the existing Galactic models in terms of the optical depth map. Such a map of the optical depth would, however, be extremely interesting and should be constructed when possible.

Acknowledgements

I would like to thank Drs. Shude Mao, Andrzej Udalski, Łukasz Wyrzykowski, Michał Szymański, Przemysław Woźniak, Nicholas Rattenbury, Eamonn Kerins, Alexander Wood, and Miss Dandan Xu for comments on this chapter. This work would not be possible without the data provided by the OGLE group and the DIA codes provided by Dr. Przemysław Woźniak.

Table 5.3: Microlensing events used for the optical depth calculation.

Star's name (field.chip.No)	OGLE / new	t_{E} [day]	t_{peak} HJD-2450000 [day]	u_0	I–baseline [mag]	f_{s}	χ^2	$\chi^2_{/\mathrm{dof}}$
206.1.33563	05-023	30.10 ± 1.02	3466.2 ± 0.1	0.703 ± 0.039	15.292 ± 0.001	0.854 ± 0.081	1235.26	2.900
206.1.54513	05-221	125.71 ± 33.03	3512.7 ± 0.4	0.062 ± 0.020	19.190 ± 0.005	0.073 ± 0.024	686.23	1.618
206.2.60188	04-169	31.77 ± 8.92	3112.8 ± 0.3	0.123 ± 0.048	19.231 ± 0.005	0.226 ± 0.094	1206.32	2.852
206.2.105542	03-147	18.62 ± 2.02	2780.8 ± >0.1	0.192 ± 0.037	17.654 ± 0.001	0.500 ± 0.102	944.30	2.217
206.3.36391	05-205	27.69 ± 5.17	3503.5 ± 0.3	0.305 ± 0.089	18.897 ± 0.004	0.467 ± 0.174	853.50	2.023
206.3.45071	**new**	87.34 ± 16.53	3338.4 ± 3.1	0.112 ± 0.124	18.072 ± 0.002	0.249 ± 0.103	1045.93	2.470
206.4.122545	**new**	51.34 ± 13.23	2139.8 ± 0.2	0.128 ± 0.038	18.594 ± 0.003	0.471 ± 0.154	865.629	2.037
206.4.37.v*	03-292	13.38 ± 1.81	2837.1 ± >0.1	0.097 ± 0.018	19.581 ± 0.009	1.751 ± 0.324	967.75	2.292
206.4.3297.v*	**new**	37.55 ± 7.41	3086.3 ± 0.1	0.096 ± 0.024	19.553 ± 0.007	0.395 ± 0.105	768.43	1.821
206.5.69909	04-137	13.51 ± 0.62	3123.3 ± 0.1	0.748 ± 0.052	15.398 ± >0.001	1.376 ± 0.169	1187.66	2.781
206.5.83280	04-233	23.92 ± 2.78	3141.0 ± >0.1	0.060 ± 0.008	18.257 ± 0.002	0.182 ± 0.026	750.86	1.758
206.5.104856	02-268	12.88 ± 4.62	2471.4 ± >0.1	0.072 ± 0.034	17.995 ± 0.002	0.129 ± 0.060	717.12	1.695
206.5.128822	**new**	23.81 ± 6.50	2170.4 ± 0.6	0.132 ± 0.051	18.638 ± 0.003	0.521 ± 0.229	717.57	1.688
206.5.4555.v*	**new**	11.63 ± 4.13	3078.6 ± 0.1	0.184 ± 0.129	19.949 ± 0.006	0.981 ± 0.623	952.55	2.252

* from the variable stars database.

Table 5.4: Microlensing events used for the optical depth calculation (continuation of Table 5.3).

Star's name (field.chip.No)	OGLE / new	t_E [day]	t_{peak} HJD-2450000 [day]	u_0	I–baseline [mag]	f_s	χ^2	$\chi^2_{/dof}$
206.7.416	03-308	21.11 ± 0.72	2874.5 ± >0.1	0.387 ± 0.022	15.708 ± >0.001	0.793 ± 0.060	785.14	1.865
206.7.18168	05-024	29.68 ± 6.68	3406.8 ± 10.4	0.196 ± 0.179	16.524 ± >0.001	0.200 ± 0.244	830.57	1.959
206.7.21032	04-184	27.09 ± 4.98	3129.3 ± 0.3	0.207 ± 0.058	18.283 ± 0.003	0.262 ± 0.085	681.44	1.611
206.7.25004	04-073	3.94 ± 0.20	3075.0 ± >0.1	0.554 ± 0.010	17.525 ± 0.013	1.000 – fixed	772.48	1.818
206.7.48050	**new**	48.16 ± 20.04	3291.4 ± 0.1	0.036 ± 0.023	17.831 ± 0.002	0.034 ± 0.017	1046.04	2.473
206.7.76724	03-364	5.21 ± 0.20	2866.7 ± >0.1	0.097 ±0.008	15.743 ± >0.001	0.879 ± 0.064	1203.71	2.826
206.7.98153	03-214	13.44 ± 0.52	2805.9 ± 0.2	0.607 ± 0.021	18.440 ± 0.003	1.000 – fixed	707.01	1.664
206.7.118074	**new**	8.40 ± 3.45	2494.1 ± 0.2	0.288 ± 0.181	16.393 ± >0.001	0.094 ± 0.074	630.09	1.486
206.7.131307	**new**	17.25 ± 3.32	2438.4 ± >0.1	0.099 ± 0.023	18.508 ± 0.003	0.356 ± 0.089	1062.41	2.494
206.7.184411	03-110	92.42 ± 20.66	2701.7 ± 5.6	0.189 ± 0.075	18.905 ± 0.005	0.418 ± 0.229	1005.75	2.418
206.8.31409	**new**	20.72 ± 8.06	3115.5 ± 0.1	0.066 ± 0.034	19.496 ± 0.008	0.229 ± 0.115	797.01	1.893
206.8.92813	04-248	19.17 ± 2.75	3141.4 ± >0.1	0.027 ± 0.005	17.918 ± 0.002	0.135 ± 0.023	758.89	1.816
206.2.109774[b]	**new**	—	—	—	18.894 ± 0.005	—	—	—
206.8.85131[b]	**new**	—	—	—	16.721 ± 0.001	—	—	—

[b] binary event.

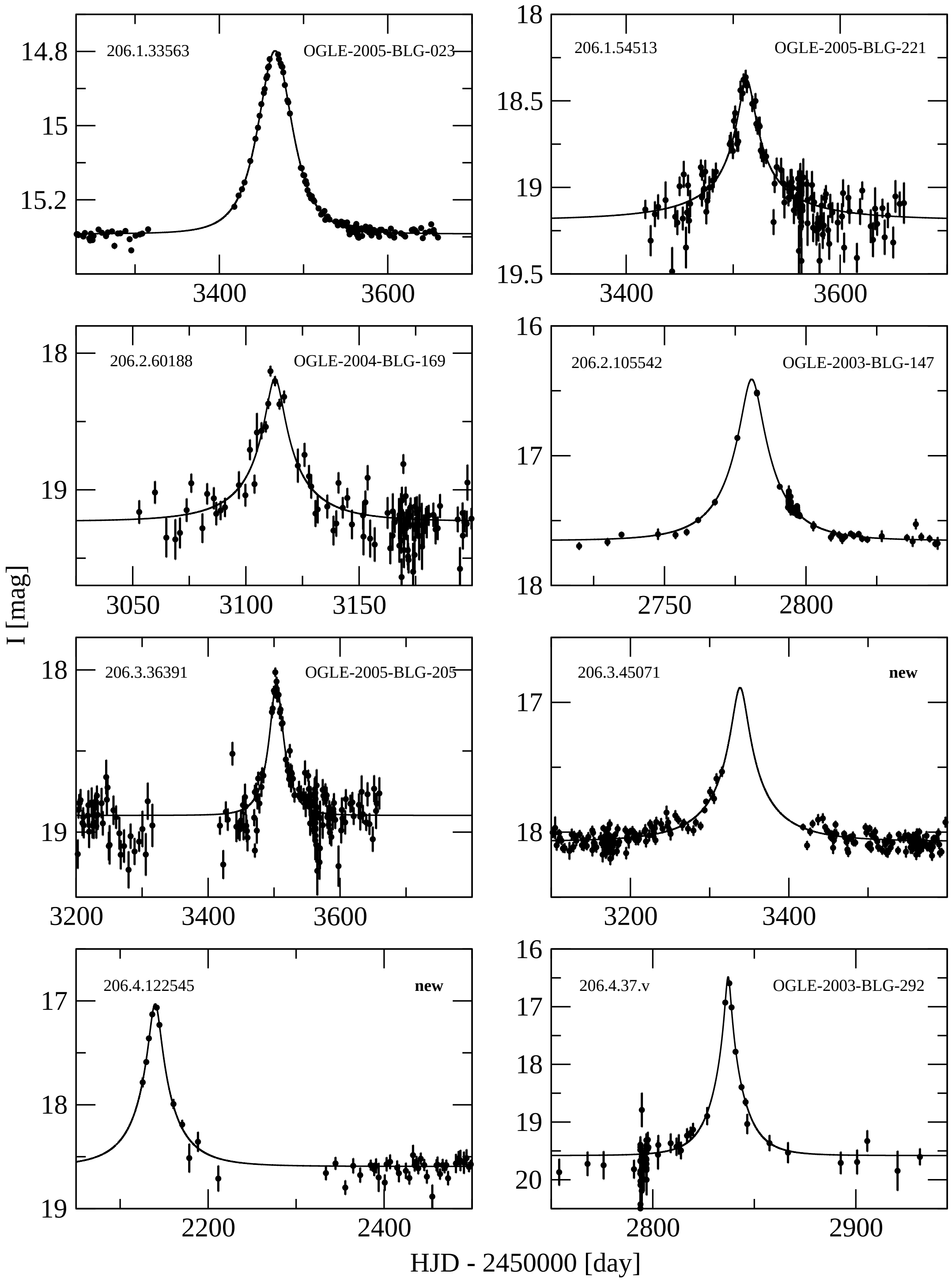

Figure 5.5: Light curves of microlensing events used in the optical depth calculation.

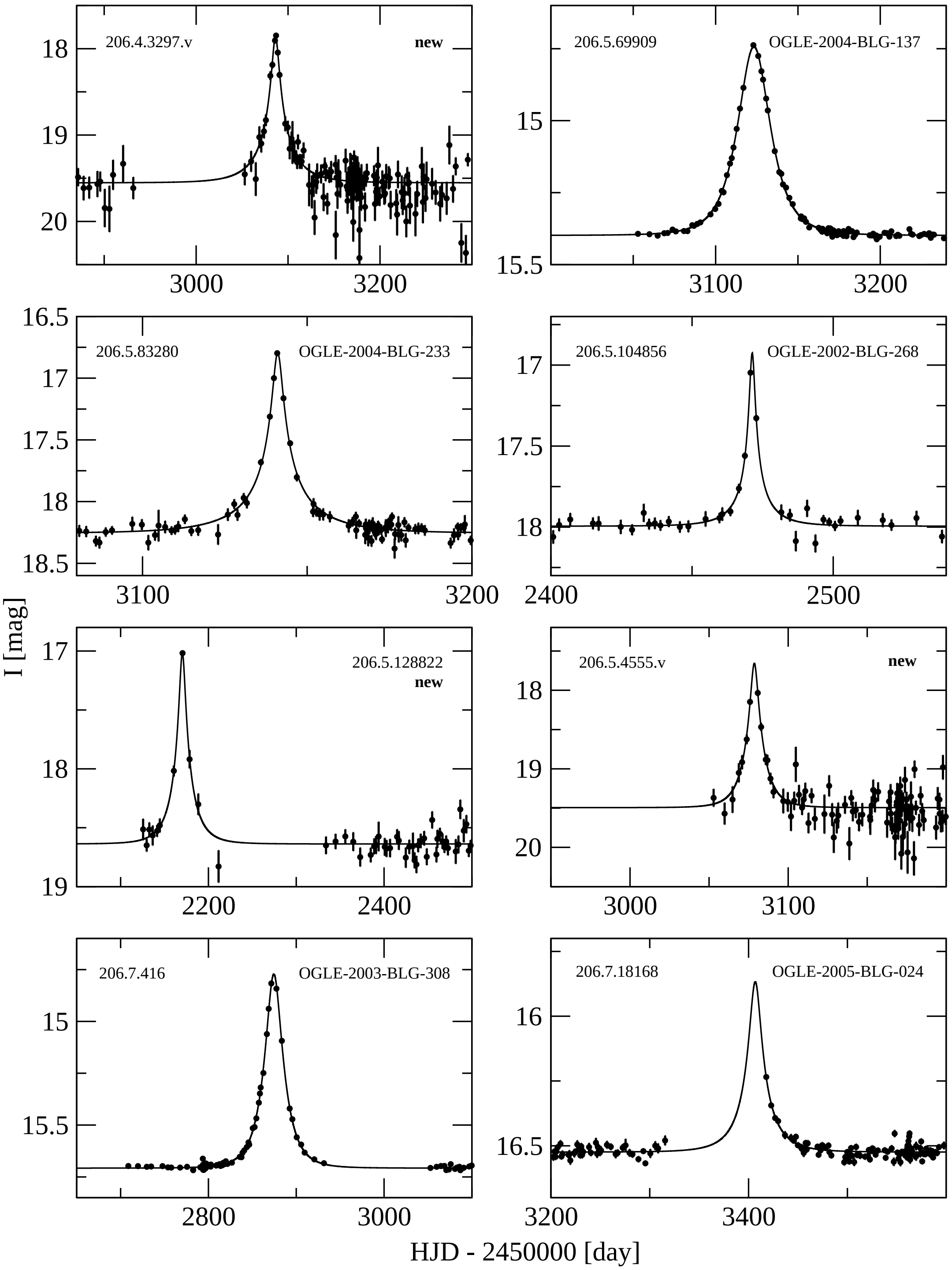

Figure 5.6: Light curves of microlensing events used in the optical depth calculation.

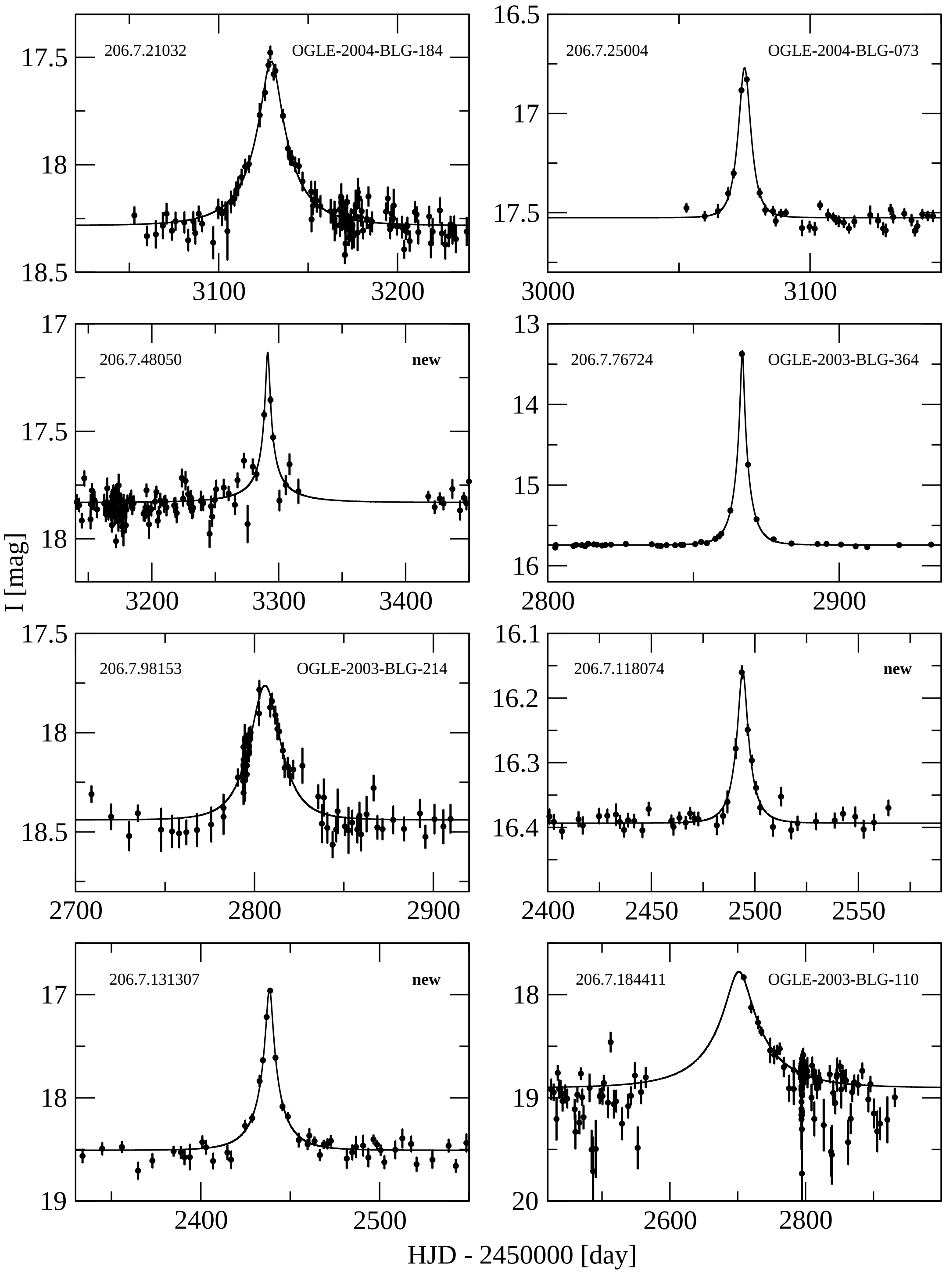

Figure 5.7: Light curves of microlensing events used in the optical depth calculation.

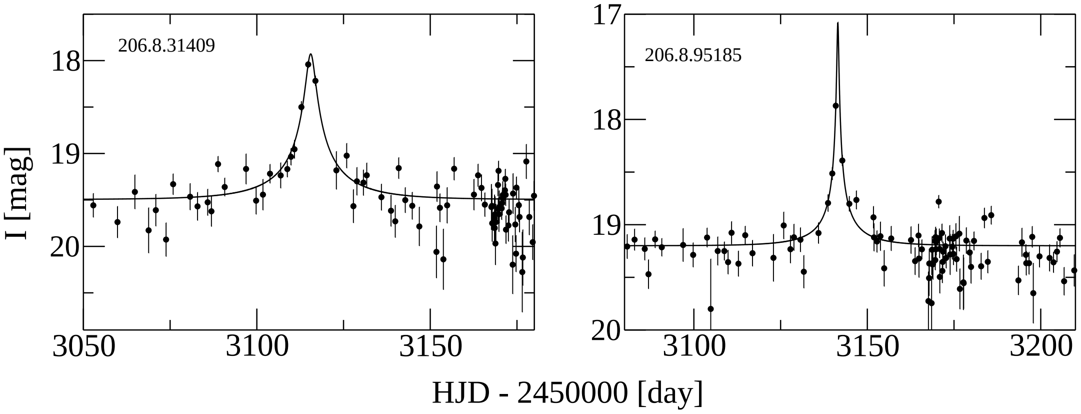

Figure 5.8: Light curves of microlensing events used in the optical depth calculation.

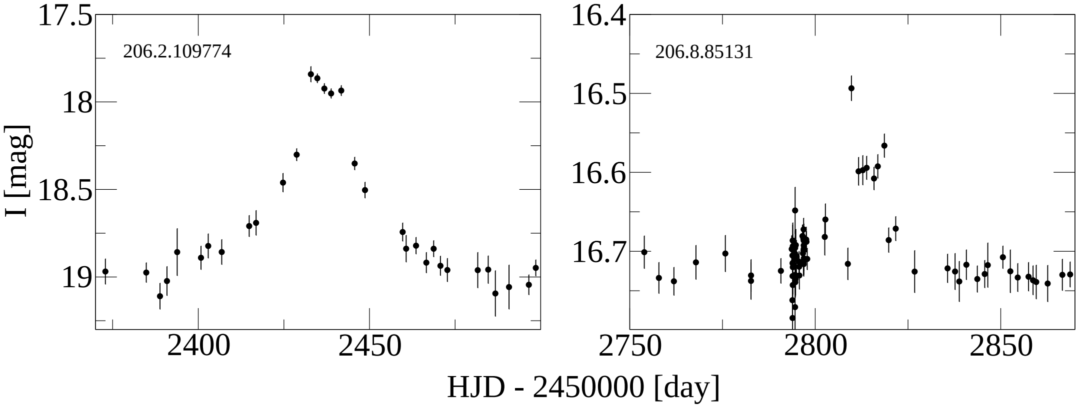

Figure 5.9: Light curves of the two binary microlensing events.

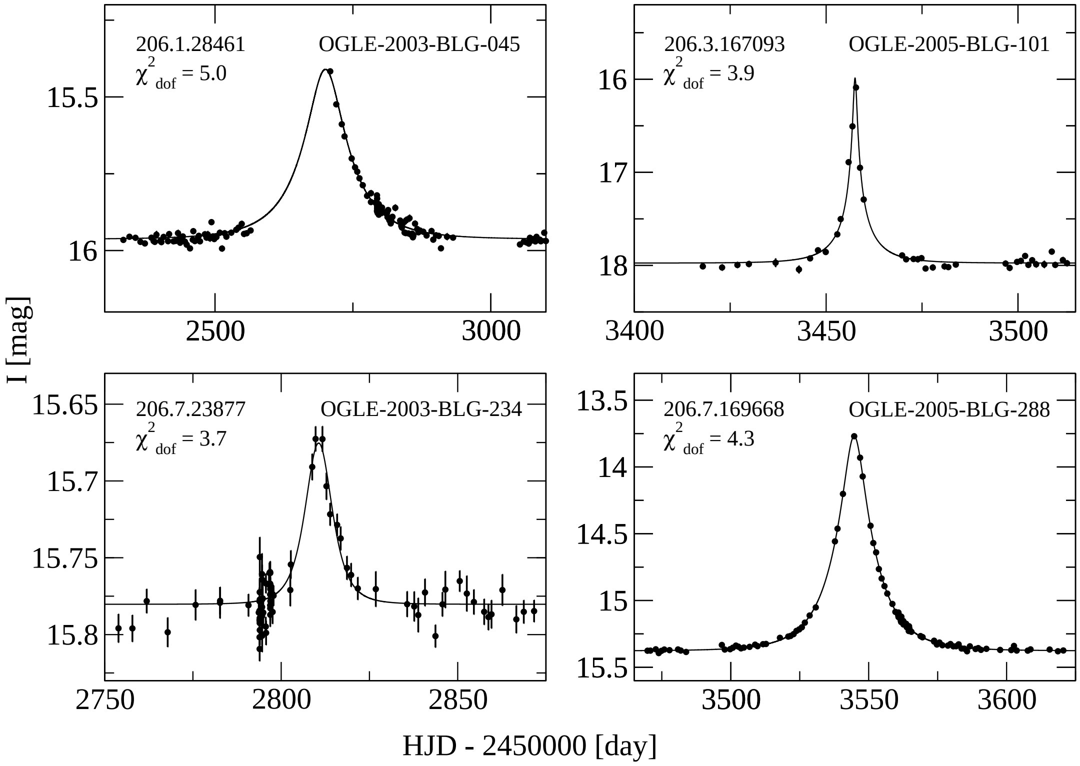

Figure 5.10: A sample of four OGLE–III microlensing events which did not pass the search criterion $\chi^2_{\rm dof} < 3$ (see §5.4.5). Underestimated error bars cause a high $\chi^2_{\rm dof}$, as indicated, for bright events.

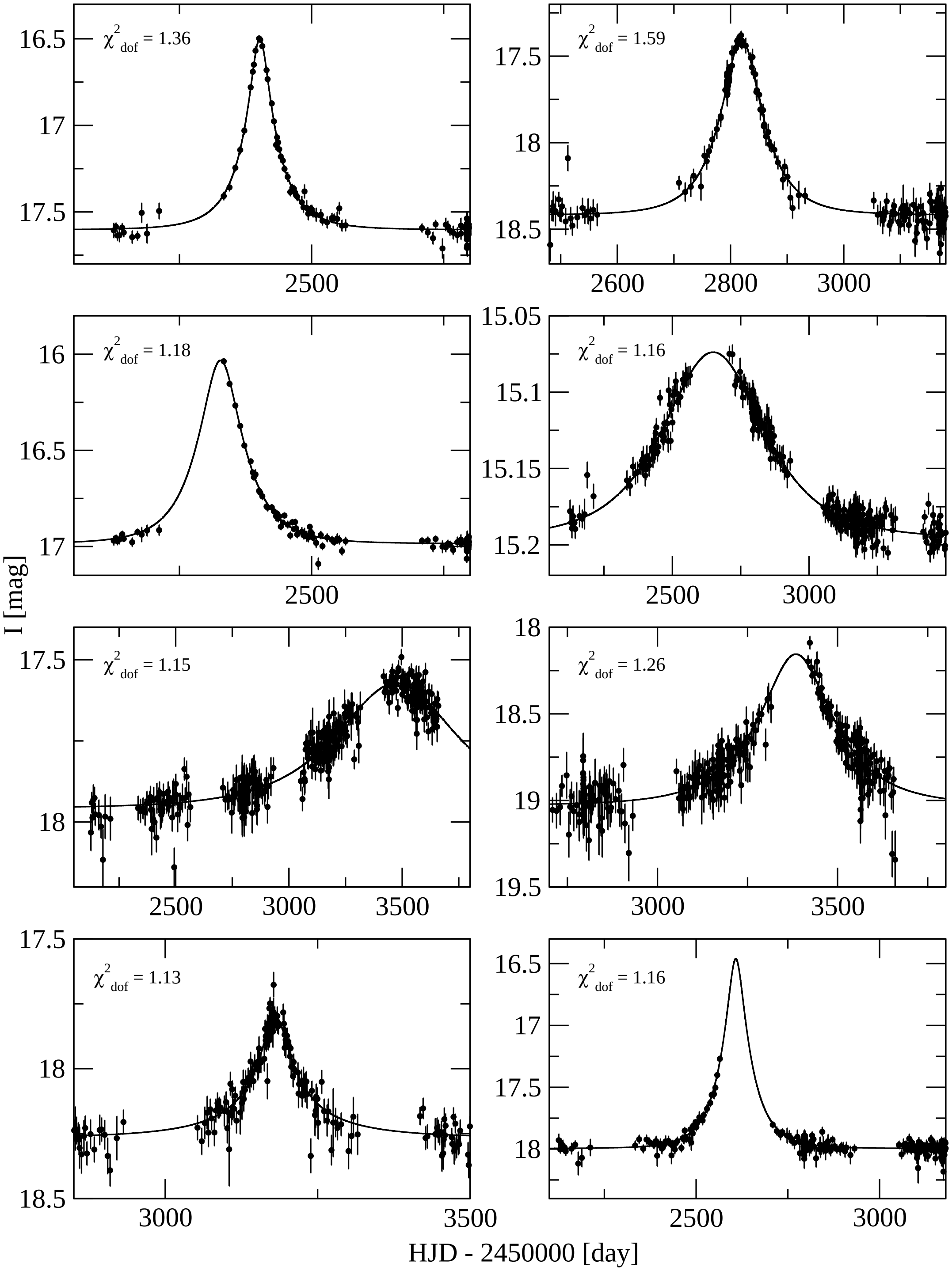

Figure 5.11: Light curves of artificial microlensing events.

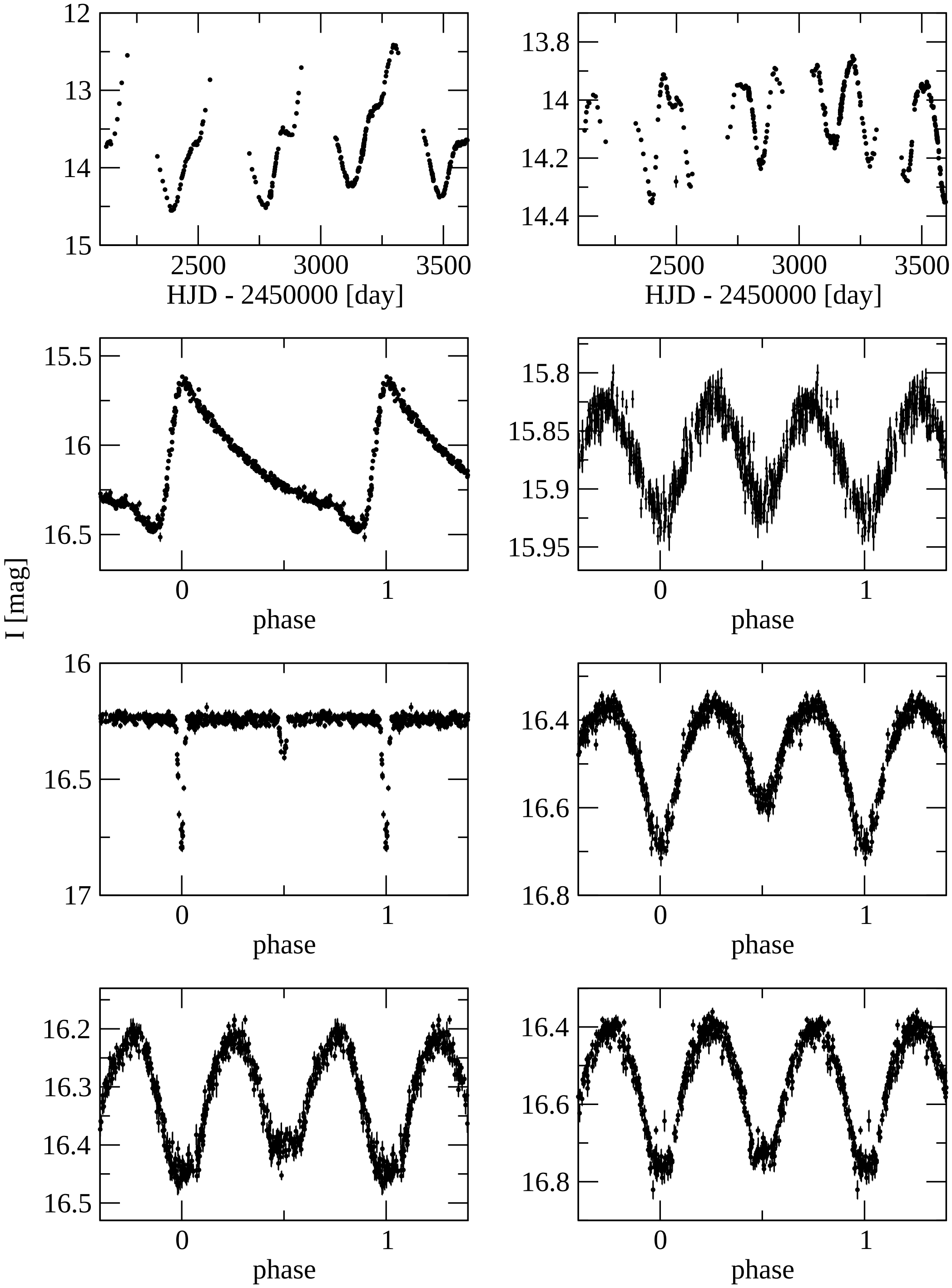

Figure 5.12: Sample light curves of variable stars from the database.

6

Summary and future work

6.1 Summary of the work presented in this thesis

The reseach presented in this thesis addresses three microlensing- and one kinematics-related topics of Galactic astronomy. The high spatial resolution of the *HST* allows a thorough investigation of blending issues. It is shown that blending is present in all microlensing applications, and is analysed differently in each scientific chapter of this thesis.

In Chapter 2 seven microlensing events from the OGLE–III database are analysed. They have coinciding images in the *HST* archive, which allow resolution of the ground-based blends into separate stars on the *HST*. The difference imaging method is used to find the residual light of the magnified source-stars on the subtracted images. Cross-correlation of the OGLE–III and *HST* images, and transformations of the DIA positions of the microlensed stars to the *HST* reference frames, pinpoint the microlensed stars. The difference in the passbands between the OGLE–III and *HST* images is the only deficiency of this project. Nevertheless, in most cases the blending fractions derived from the *HST* are in agreement with the fitted ones. Fitting the single lens model to the data with the fixed *HST* blending fractions does not make significant changes to the goodness of the fits (except for the event MOA-2002-BLG-33, which in fact is a binary event), which implies that the fractions of light derived in the adjacent passbands (V, R) are directly applicable to the I-band light curves.

Chapter 3 presents a study of the kinematics of the Galactic bulge. Based on two-epoch *HST* observations of 35+2 bulge fields we determine the relative proper motions of ~26,000 stars with an accuracy of a fraction of a milli-arcsec per year. Applying cuts on signal-to-noise ratio/magnitudes, we use ~16,000 stars to calculate the proper motion dispersions and covariance term. We find small gradients of the proper motion dispersions with respect to the Galactic coordinates. The increasing $\sigma_{\rm l}(b)$ is likely due to a gradient in the bulge rotation and/or could be an effect of the disk contamination. The increase of $\sigma_{\rm b}(l)$ along with decreasing anisotropy $\sigma_{\rm l}/\sigma_{\rm b}$ suggests a higher contribution of metal-poor (bulge) stars to the total number of observed stars. Both our analysis and the recent paper of Rattenbury et al. (2007a) show clear detection of a non-zero covariance term $C_{\rm lb}$; in our case the error-weighted $C_{\rm lb} \approx -0.10$. This result suggests a possible tilt of the bulge velocity ellipsoid by ~16° with respect to the Galactic plane.

Each of the 35 fields presented in Chapter 3 is centered on a past microlensed source from the MACHO database. As pointed out by Han and Chang (2003) and Wood (2006), in a few per cent of microlensing events toward the Galactic centre a luminous lens may be detectable a decade after the microlensing episode. Out of 35 candidate microlensed stars we find six of them have extended and certainly different PSFs compared to most neighbouring stars. In one case, described in Chapter 4, we find two well-separated PSFs. We investigate the possibility of these two stars being a lens and source. Using various techniques we analyse the original MACHO images (with DIA) producing new light curves. The *HST* astrometry (giving the proper motions) and photometry (giving the magnitudes of all contributing stars) are invaluable parts of this project. Based on various arguments such as the relative proper motions, colour shift, CMD, parallax effect, etc. there are no doubts that we have detected the lens and source separating from a nearly perfect alignment (~1/3 mas at the microlensing peak; the Einstein radius $\theta_{\rm E} = 0.75 \pm 0.13$ mas). The available data, however, are not sufficient to provide the final answer on which star is the lens and which is the source. Two competing scenarios predict that the lens is a star with a mass of ~0.6 $M_\odot$ or ~0.9 $M_\odot$ at a distance of ~4 kpc from us. The source star is likely located in the bulge at a distance of 8 – 9 kpc.

Chapter 5 presents the analysis of the massive microlensing dataset. We analyse one of the OGLE–III fields – BLG206 – using data spanning 4.2 years. We build our own pipeline for the image analysis and an image simulator for the detection efficiency calculations. In total we analyse 3456 images, each of 2048 × 4096 pixels in size, detecting 1.5 million stars and building light curves for each of them. We find 17 known and 11 previously unknown microlensing events (including two binary ones). The major improvement over previously published studies comes with the image simulator. It uses the original images and injects artificial microlensing events into them. The hybrid images are then processed through the same pipeline and search algorithm, providing information on the detection efficiency of events. We calculate the optical depth in this field to be $\tau_{\mathrm{BLG206}} = (2.91 \pm 0.77) \times 10^{-6}$ for 26 single lens events and $\tau_{\mathrm{BLG206}} = (3.22 \pm 0.85) \times 10^{-6}$ for 28 events including the two binary ones. Our approach can in principle be extended to all the OGLE–III fields.

6.2 Future work

The detection rate of microlensing events toward the Galactic bulge is of ~500 per year. The project presented in Chapter 2 was conducted using the data spanning the years 2001 – 2004. Three years later (now – 2007) there are ~1500 new events in the OGLE–III database. In addition, as the *HST* takes more and more images, there will be more and more coinciding images with the OGLE–III events. It would be interesting to conduct a similar project in the near future in order to further explore the subject. The blending issue can be tested by the simulation means as well. It should be straightforward to simulate simultaneously a series of the OGLE–III hybrid images along with the corresponding *HST* image. Both the OGLE–III hybrid and *HST* images would have microlensing events injected into them.

The proper motion survey presented in Chapter 3 covers 5° × 2.5° in the vicinity of Baade's Window. Rattenbury et al. (2007a) present a similar analysis using ground-based data, providing 45 additional measurements of the proper motion dispersions and covariance term. It should be pretty straightforward to extend the *HST* proper motion survey for both positive and negative Galactic latitudes and longitudes. Unfortunately, we were not awarded *HST* time in the present proposal cycle. What is striking is that there are already plenty of suitable first epoch-images in the HST archive.

There are five more candidates for direct detection of a lens in our sample of 35. The existing data, however, are not sufficient to conduct a similar analysis as presented in Chapter 4. Clearly more data are necessary. Han and Chang (2003) based their calculation of the amount of detectable lenses on the analytical resolvability of two Gaussian functions. In principle two stars can be resolvable for separations smaller than predicted by the analytical approach. We are currently working on so-called detectability maps. We simulate *HST* and *JWST* images, in which we inject two stars of different magnitudes at different separations. We then perform fitting of two PSFs and compare the output with input parameters. This is still an ongoing project, but preliminary results show that there should be an order of magnitude more (∼20%) resolvable/detectable lenses than predicted by Han and Chang (2003). Assuming that the five other candidates are indeed the unresolved lens and source the fraction of detectable lenses from our sample is ∼17% (6/35) – substantially higher than the previous estimates.

Another planned project is to understand the kinematic identity of the microlensed sources. We have identified 35 microlensed sources out of which 29 have reliable proper motions (another 6 as described above are blends of two or more stars). At the preliminary stage the Kolmogorov-Smirnov test shows no difference between the proper motion distribution of the 29 microlensed stars and the ∼26,000 field stars. However, a more thorough investigation is necessary in order to pinpoint their kinematic identity.

We are also working toward building a map of the optical depth as a function of the Galactic coordinates. In total there will be nine adjacent fields analysed. The expected accuracy of the optical depth in those fields is better than ~25%. We expect that the spatial measurements of the optical depth will provide important constraints on the existing Galactic models.

References

Abe, F., Bennett, D. P., Bond, I. A., Calitz, J. J., Claret, A., Cook, K. H., Furuta, Y., Gal-Yam, A., Glicenstein, J.-F., Hearnshaw, J. B., Hauschildt, P. H., Kent, D., Kilmartin, P. M., Kurata, Y., Masuda, K., Maoz, D., Matsubara, Y., Meintjes, P. J., Moniez, M., Muraki, Y., Noda, S., Ofek, E. O., Okajima, K., Philpott, L., Rattenbury, N. J., Rhie, S. H., Sako, T., Sullivan, D. J., Sumi, T., Terndrup, D. M., Tristram, P. J., Yanagisawa, T., and Yock, P. C. M.: 2003, *A&A* **411**, L493

Afonso, C., Albert, J. N., Alard, C., Andersen, J., Ansari, R., Aubourg, É., Bareyre, P., Bauer, F., Beaulieu, J. P., Blanc, G., Bouquet, A., Char, S., Charlot, X., Couchot, F., Coutures, C., Derue, F., Ferlet, R., Fouqué, P., Glicenstein, J. F., Goldman, B., Gould, A., Graff, D., Gros, M., Haissinski, J., Hamadache, C., Hamilton, J. C., Hardin, D., de Kat, J., Kim, A., Lasserre, T., LeGuillou, L., Lesquoy, É., Loup, C., Magneville, C., Mansoux, B., Marquette, J. B., Maurice, É., Maury, A., Milsztajn, A., Moniez, M., Palanque-Delabrouille, N., Perdereau, O., Prévot, L., Regnault, N., Rich, J., Spiro, M., Tisserand, P., Vidal-Madjar, A., Vigroux, L., and Zylberajch, S.: 2003a, *A&A* **404**, 145

Afonso, C., Albert, J. N., Andersen, J., Ansari, R., Aubourg, É., Bareyre, P., Beaulieu, J. P., Blanc, G., Charlot, X., Couchot, F., Coutures, C., Ferlet, R., Fouqué, P., Glicenstein, J. F., Goldman, B., Gould, A., Graff, D., Gros, M., Haissinski, J., Hamadache, C., de Kat, J., Lasserre, T., Le Guillou, L., Lesquoy, É., Loup, C., Magneville, C., Marquette, J. B., Maurice, É., Maury, A., Milsztajn, A., Moniez, M., Palanque-Delabrouille, N., Perdereau, O., Prévot, L., Rahal, Y. R., Rich, J., Spiro, M., Tisserand, P., Vidal-Madjar, A., Vigroux, L., and Zylberajch, S.: 2003b, *A&A* **400**, 951

Alard, C.: 1997, *A&A* **321**, 424

Alard, C.: 2000, *A&AS* **144**, 363

Alard, C.: 2001, *A&A* **379**, L44

Alard, C. and Lupton, R. H.: 1998, *ApJ* **503**, 325

Alcock, C., Akerloff, C. W., Allsman, R. A., Axelrod, T. S., Bennett, D. P., Chan, S., Cook, C. H., Freeman, K. C., Griest, K., Marshall, S. L., Park, H. S., Perlmutter, S., Peterson, B. A., Pratt, M. R., Quinn, P. J., Rodgers, A. W., Stubbs, C. W., and Sutherland, W.: 1993, *Nature* **365**, 621

Alcock, C., Allsman, R. A., Alves, D., Ansari, R., Aubourg, E., Axelrod, T. S., Bareyre, P., Beaulieu, J.-P., Becker, A. C., Bennett, D. P., Brehin, S., Cavalier, F., Char, S., Cook, K. H., Ferlet, R., Fernandez, J., Freeman, K. C., Griest, K., Grison, P., Gros, M., Gry, C., Guibert, J., Lachieze-Rey, M., Laurent, B., Lehner, M. J., Lesquoy, E., Magneville, C., Marshall, S. L., Maurice, E., Milsztajn, A., Minniti, D., Moniez, M., Moreau, O., Moscoso, L., Palanque-Delabrouille, N., Peterson, B. A., Pratt, M. R., Prevot, L., Queinnec, F., Quinn, P. J., Renault, C., Rich, J., Spiro, M., Stubbs, C. W., Sutherland, W., Tomaney, A., Vandehei, T., Vidal-Madjar, A., Vigroux, L., and Zylberajch, S.: 1998, *ApJL* **499**, L9+

Alcock, C., Allsman, R. A., Alves, D., Axelrod, T. S., Becker, A. C., Bennett, D. P., Cook, K. H., Freeman, K. C., Griest, K., Guern, J., Lehner, M. J., Marshall, S. L., Peterson, B. A., Pratt, M. R., Quinn, P. J., Rodgers, A. W., Stubbs, C. W., Sutherland, W., and The MACHO Collaboration: 1996, *ApJ* **471**, 774

Alcock, C., Allsman, R. A., Alves, D., Axelrod, T. S., Bennett, D. P., Cook, K. H., Freeman, K. C., Griest, K., Guern, J., Lehner, M. J., Marshall, S. L., Park, H.-S., Perlmutter, S., Peterson, B. A., Pratt, M. R., Quinn, P. J., Rodgers, A. W., Stubbs, C. W., and Sutherland, W.: 1997, *ApJ* **479**, 119

Alcock, C., Allsman, R. A., Alves, D. R., Axelrod, T. S., Becker, A. C., Bennett, D. P., Cook, K. H., Dalal, N., Drake, A. J., Freeman, K. C., Geha, M., Griest, K., Lehner, M. J., Marshall, S. L., Minniti, D., Nelson, C. A., Peterson, B. A., Popowski, P., Pratt, M. R., Quinn, P. J., Stubbs, C. W., Sutherland, W., Tomaney, A. B., Vandehei, T., and Welch, D.: 2000a, *ApJ* **542**, 281

Alcock, C., Allsman, R. A., Alves, D. R., Axelrod, T. S., Becker, A. C., Bennett, D. P., Cook, K. H., Dalal, N., Drake, A. J., Freeman, K. C., Geha, M., Griest, K., Lehner, M. J., Marshall, S. L., Minniti, D., Nelson, C. A., Peterson, B. A., Popowski, P., Pratt, M. R., Quinn, P. J., Stubbs, C. W., Sutherland, W., Tomaney, A. B., Vandehei, T., and Welch, D. L.: 2001a, *ApJL* **550**, L169

Alcock, C., Allsman, R. A., Alves, D. R., Axelrod, T. S., Becker, A. C., Bennett, D. P., Cook, K. H., Drake, A. J., Freeman, K. C., Geha, M., Griest, K., Keller, S. C., Lehner, M. J., Marshall, S. L., Minniti, D., Nelson, C. A., Peterson, B. A., Popowski, P., Pratt, M. R., Quinn, P. J., Stubbs, C. W., Sutherland, W., Tomaney, A. B., Vandehei, T., and Welch, D.: 2001b, *Nature* **414**, 617

Alcock, C., Allsman, R. A., Alves, D. R., Axelrod, T. S., Becker, A. C., Bennett, D. P., Cook, K. H., Drake, A. J., Freeman, K. C., Geha, M., Griest, K., Lehner, M. J., Marshall, S. L., Minniti, D., Nelson, C. A., Peterson, B. A., Popowski, P., Pratt, M. R., Quinn, P. J., Stubbs, C. W., Sutherland, W., Tomaney, A. B., Vandehei, T., and Welch, D. L.: 2000b, *ApJ* **541**, 734

An, J. H., Albrow, M. D., Beaulieu, J.-P., Caldwell, J. A. R., DePoy, D. L., Dominik, M., Gaudi, B. S., Gould, A., Greenhill, J., Hill, K., Kane, S., Martin, R., Menzies, J., Pogge, R. W., Pollard, K. R., Sackett, P. D., Sahu, K. C., Vermaak, P., Watson, R., and Williams, A.: 2002, *ApJ* **572**, 521

Aubourg, E., Bareyre, P., Brehin, S., Gros, M., Lachieze-Rey, M., Laurent, B., Lesquoy, E., Magneville, C., Milsztajn, A., Moscoso, L., Queinnec, F., Rich, J., Spiro, M., Vigroux, L., Zylberajch, S., Ansari, R., Cavalier, F., Moniez, M., Beaulieu, J. P., Ferlet, R., Grison, P., Vidal-Madjar, A., Guibert, J., Moreau, O., Tajahmady, F., Maurice, E., Prevot, L., and Gry, C.: 1993, *Nature* **365**, 623

Axelrod, T., Alcock, C., Allsman, R., Bennett, D., Cook, K., Freeman, K., Peterson, B., Quinn, P., Rodgers, A., Griest, K., Marshall, S., Perlmutter, S., Pratt, M., Stubbs, C., and Sutherland, W.: 1994, in *Bulletin of the American Astronomical Society*, Vol. 26 of *Bulletin of the American Astronomical Society*, pp 912–+

Babusiaux, C. and Gilmore, G.: 2005, *MNRAS* **358**, 1309

Baraffe, I., Chabrier, G., Allard, F., and Hauschildt, P. H.: 1997, *A&A* **327**, 1054

Beaulieu, J.-P., Bennett, D. P., Fouqué, P., Williams, A., Dominik, M., Jorgensen, U. G., Kubas, D., Cassan, A., Coutures, C., Greenhill, J., Hill, K., Menzies, J., Sackett, P. D., Albrow, M., Brillant, S., Caldwell, J. A. R., Calitz, J. J., Cook, K. H., Corrales, E., Desort, M., Dieters, S., Dominis, D., Donatowicz, J., Hoffman, M., Kane, S., Marquette, J.-B., Martin, R., Meintjes, P., Pollard, K., Sahu, K., Vinter, C., Wambsganss, J., Woller, K., Horne, K., Steele, I., Bramich, D. M., Burgdorf, M., Snodgrass, C., Bode, M., Udalski, A., Szymański, M. K., Kubiak, M., Więckowski, T., Pietrzyński, G., Soszyński, I., Szewczyk, O., Wyrzykowski, Ł., Paczyński, B., Abe, F., Bond, I. A., Britton, T. R., Gilmore, A. C., Hearnshaw, J. B., Itow, Y., Kamiya, K., Kilmartin, P. M., Korpela, A. V., Masuda, K., Matsubara, Y., Motomura, M., Muraki, Y., Nakamura, S., Okada, C., Ohnishi, K., Rattenbury, N. J., Sako, T., Sato, S., Sasaki, M., Sekiguchi, T., Sullivan, D. J., Tristram, P. J., Yock, P. C. M., and Yoshioka, T.: 2006, *Nature* **439**, 437

Benjamin, R. A., Churchwell, E., Babler, B. L., Indebetouw, R., Meade, M. R., Whitney, B. A., Watson, C., Wolfire, M. G., Wolff, M. J., Ignace, R., Bania, T. M., Bracker, S., Clemens, D. P., Chomiuk, L., Cohen, M., Dickey, J. M., Jackson, J. M., Kobulnicky, H. A., Mercer, E. P., Mathis, J. S., Stolovy, S. R., and Uzpen, B.: 2005, *ApJL* **630**, L149

Bennett, D. P.: 2005, *ApJ* **633**, 906

Bennett, D. P., Akerlof, C., Alcock, C., Allsman, R., Axelrod, T., Cook, K. H., Freeman, K., Griest, K., Marshall, S., Park, H.-S., Perlmutter, S., Peterson, B., Quinn, P., Rodgers, A., Stubbs, C. W., and Sutherland, W.: 1993, in C. W. Akerlof and M. A. Srednicki (eds.), *Texas/PASCOS '92: Relativistic Astrophysics and Particle Cosmology*, Vol. 688 of *New York Academy Sciences Annals*, pp 612–+

Bennett, D. P., Anderson, J., Bond, I. A., Udalski, A., and Gould, A.: 2006, *ApJL* **647**, L171

Bennett, D. P., Becker, A. C., Quinn, J. L., Tomaney, A. B., Alcock, C., Allsman, R. A., Alves, D. R., Axelrod, T. S., Calitz, J. J., Cook, K. H., Drake, A. J., Fragile, P. C., Freeman, K. C., Geha, M., Griest, K., Johnson, B. R., Keller, S. C., Laws, C., Lehner, M. J., Marshall, S. L., Minniti, D., Nelson, C. A., Peterson, B. A., Popowski, P., Pratt, M. R., Quinn, P. J., Rhie, S. H., Stubbs, C. W., Sutherland, W., Vandehei, T., and Welch, D.: 2002, *ApJ* **579**, 639

Bessell, M. S.: 1990, *A&AS* **83**, 357

Binney, J.: 2005, in C. Turon, K. S. O'Flaherty, and M. A. C. Perryman (eds.), *ESA SP-576: The Three-Dimensional Universe with Gaia*, pp 89–+

Binney, J. and Merrifield, M.: 1998, *Galactic astronomy*, Galactic astronomy / James Binney and Michael Merrifield. Princeton, NJ : Princeton University Press, 1998.

Bissantz, N., Debattista, V. P., and Gerhard, O.: 2004, *ApJL* **601**, L155

Blitz, L. and Spergel, D. N.: 1991, *ApJ* **379**, 631

Bond, I. A., Udalski, A., Jaroszyński, M., Rattenbury, N. J., Paczyński, B., Soszyński, I., Wyrzykowski, Ł., Szymański, M. K., Kubiak, M., Szewczyk, O., Żebruń, K., Pietrzyński, G., Abe, F., Bennett, D. P., Eguchi, S., Furuta, Y., Hearnshaw, J. B., Kamiya, K., Kilmartin, P. M., Kurata, Y., Masuda, K., Matsubara, Y., Muraki, Y., Noda, S., Okajima, K., Sako, T., Sekiguchi, T., Sullivan, D. J., Sumi, T., Tristram, P. J., Yanagisawa, T., and Yock, P. C. M.: 2004, *ApJL* **606**, L155

Buchalter, A., Kamionkowski, M., and Rich, R. M.: 1996, *ApJ* **469**, 676

Calchi Novati, S., Paulin-Henriksson, S., An, J., Baillon, P., Belokurov, V., Carr, B. J., Crézé, M., Evans, N. W., Giraud-Héraud, Y., Gould, A., Hewett, P., Jetzer, P., Kaplan, J., Kerins, E., Smartt, S. J., Stalin, C. S., Tsapras, Y., and Weston, M. J.: 2005, *A&A* **443**, 911

Chang, K. and Refsdal, S.: 1984, *A&A* **132**, 168

Cook, K., Alcock, C., Allsman, R., Axelrod, T., Freeman, K., Peterson, B., Quinn, P., Rodgers, A., Bennett, D., Perlmutter, S., Griest, K., Marshall, S., Pratt, M., Stubbs, C., and Sutherland, W.: 1994, in *Bulletin of the American Astronomical Society*, Vol. 26 of *Bulletin of the American Astronomical Society*, pp 1336–+

Cousins, A. W. J.: 1976, *MmRAS* **81**, 25

Dalal, N. and Lane, B. F.: 2003, *ApJ* **589**, 199

de Jong, J. T. A., Kuijken, K., Crotts, A. P. S., Sackett, P. D., Sutherland, W. J., Uglesich, R. R., Baltz, E. A., Cseresnjes, P., Gyuk, G., Widrow, L. M., and The MEGA collaboration: 2004, *A&A* **417**, 461

de Rujula, A., Jetzer, P., and Masso, E.: 1992, *A&A* **254**, 99

de Vaucouleurs, G., in Kerr, F., and Rodgers, A., e.: 1964, *Australian Academy of Sciences* p. 195

Delplancke, F., Górski, K. M., and Richichi, A.: 2001, *A&A* **375**, 701

Di Stefano, R. and Esin, A. A.: 1995, *ApJL* **448**, L1+

Drake, A. J., Cook, K. H., and Keller, S. C.: 2004, *ApJL* **607**, L29

Dwek, E., Arendt, R. G., Hauser, M. G., Kelsall, T., Lisse, C. M., Moseley, S. H., Silverberg, R. F., Sodroski, T. J., and Weiland, J. L.: 1995, *ApJ* **445**, 716

Erwin, P. and Sparke, L. S.: 1999, *ApJL* **521**, L37

Evans, N. W. and Belokurov, V.: 2002, *ApJL* **567**, L119

Fruchter, A. S. and Hook, R. N.: 2002, *PASP* **114**, 144

Georgelin, Y. M. and Georgelin, Y. P.: 1976, *A&A* **49**, 57

Gerhard, O.: 2002, in G. S. Da Costa and H. Jerjen (eds.), *The Dynamics, Structure and History of Galaxies: A Workshop in Honour of Professor Ken Freeman*, Vol.

273 of *Astronomical Society of the Pacific Conference Series*, pp 73–+

Gerhard, O. E.: 2001, in J. G. Funes and E. M. Corsini (eds.), *ASP Conf. Ser. 230: Galaxy Disks and Disk Galaxies*, pp 21–30

Ghez, A. M., Klein, B. L., Morris, M., and Becklin, E. E.: 1998, *ApJ* **509**, 678

Girardi, L., Bertelli, G., Bressan, A., Chiosi, C., Groenewegen, M. A. T., Marigo, P., Salasnich, B., and Weiss, A.: 2002, *A&A* **391**, 195

Gould, A.: 1994, *ApJL* **421**, L71

Gould, A.: 2004, *ApJ* **606**, 319

Gould, A., Bennett, D. P., and Alves, D. R.: 2004, *ApJ* **614**, 404

Gould, A. and Loeb, A.: 1992, *ApJ* **396**, 104

Gould, A., Miralda-Escude, J., and Bahcall, J. N.: 1994, *ApJL* **423**, L105+

Gould, A., Udalski, A., An, D., Bennett, D. P., Zhou, A.-Y., Dong, S., Rattenbury, N. J., Gaudi, B. S., Yock, P. C. M., Bond, I. A., Christie, G. W., Horne, K., Anderson, J., Stanek, K. Z., DePoy, D. L., Han, C., McCormick, J., Park, B.-G., Pogge, R. W., Poindexter, S. D., Soszyński, I., Szymański, M. K., Kubiak, M., Pietrzyński, G., Szewczyk, O., Wyrzykowski, Ł., Ulaczyk, K., Paczyński, B., Bramich, D. M., Snodgrass, C., Steele, I. A., Burgdorf, M. J., Bode, M. F., Botzler, C. S., Mao, S., and Swaving, S. C.: 2006, *ApJL* **644**, L37

Groth, E. J.: 1986, *AJ* **91**, 1244

Häfner, R., Evans, N. W., Dehnen, W., and Binney, J.: 2000, *MNRAS* **314**, 433

Hamadache, C., Le Guillou, L., Tisserand, P., Afonso, C., Albert, J. N., Andersen, J., Ansari, R., Aubourg, É., Bareyre, P., Beaulieu, J. P., Charlot, X., Coutures, C., Ferlet, R., Fouqué, P., Glicenstein, J. F., Goldman, B., Gould, A., Graff, D., Gros, M., Haissinski, J., de Kat, J., Lesquoy, É., Loup, C., Magneville, C., Marquette, J. B., Maurice, É., Maury, A., Milsztajn, A., Moniez, M., Palanque-Delabrouille, N., Perdereau, O., Rahal, Y. R., Rich, J., Spiro, M., Vidal-Madjar, A., Vigroux, L., and Zylberajch, S.: 2006, *A&A* **454**, 185

Han, C. and Chang, H.-Y.: 2003, *MNRAS* **338**, 637

Han, C. and Gould, A.: 1995, *ApJ* **449**, 521

Han, C. and Gould, A.: 2003, *ApJ* **592**, 172

Holtzman, J. A., Burrows, C. J., Casertano, S., Hester, J. J., Trauger, J. T., Watson, A. M., and Worthey, G.: 1995, *PASP* **107**, 1065

Howell, S. B.: 2000, *Handbook of CCD Astronomy*, Handbook of CCD astronomy / Steve B. Howell. Cambridge, U.K. ; New York : Cambridge University Press, c2000. (Cambridge observing handbooks for research astronomers ; 2)

Ibata, R. A., Wyse, R. F. G., Gilmore, G., Irwin, M. J., and Suntzeff, N. B.: 1997, *AJ* **113**, 634

Izumiura, H., Catchpole, R., Deguchi, S., Hashimoto, O., Nakada, Y., Onaka, T., Ono, T., Sekiguchi, K., Ukita, N., and Yamamura, I.: 1995, *ApJS* **98**, 271

Jaroszyński, M.: 2002, *Acta Astronomica* **52**, 39

Jaroszyński, M., Udalski, A., Kubiak, M., Szymański, M., Pietrzyński, G., Soszyński, I., Żebruń, K., Szewczyk, O., and Wyrzykowski, Ł.: 2004, *Acta Astronomica* **54**, 103

Jiang, G., DePoy, D. L., Gal-Yam, A., Gaudi, B. S., Gould, A., Han, C., Lipkin, Y., Maoz, D., Ofek, E. O., Park, B.-G., Pogge, R. W., Udalski, A., Kubiak, M., Szymański, M. K., Szewczyk, O., Żebruń, K., Wyrzykowski, Ł., Soszyński, I., Pietrzyński, G., Albrow, M. D., Beaulieu, J.-P., Caldwell, J. A. R., Cassan, A., Coutures, C., Dominik, M., Donatowicz, J., Fouqué, P., Greenhill, J., Hill, K., Horne, K., Jørgensen, S. F., Jørgensen, U. G., Kane, S., Kubas, D., Martin, R., Menzies, J., Pollard, K. R., Sahu, K. C., Wambsganss, J., Watson, R., and Williams, A.: 2004, *ApJ* **617**, 1307

Johnson, H. L. and Morgan, W. W.: 1953, *ApJ* **117**, 313

Kerins, E. and Point-Agape Collaboration: 2003, in N. J. C. Spooner and V. Kudryavtsev (eds.), *Identification of Dark Matter*, pp 183–188

Koekemoer, A. M., Fruchter, A. S., Hook, R. N., and Hack, W.: 2002, in S. Arribas, A. Koekemoer, and B. Whitmore (eds.), *The 2002 HST Calibration Workshop, Baltimore, Maryland, October 17 and 18, 2002. Edited by Santiago Arribas, Anton Koekemoer, and Brad Whitmore. Baltimore, MD: Space Telescope Science Institute, 2002., p.337*, pp 337–+

Kozłowski, S., Woźniak, P. R., Mao, S., Smith, M. C., Sumi, T., Vestrand, W. T., and Wyrzykowski, Ł.: 2006a, *MNRAS* **370**, 435

Kozłowski, S., Woźniak, P. R., Mao, S., Smith, M. C., Sumi, T., Vestrand, W. T., and Wyrzykowski, Ł.: 2006b, *VizieR Online Data Catalog* **737**, 435

Kozłowski, S., Woźniak, P. R., Mao, S., and Wood, A.: 2007, *ArXiv Astrophysics e-prints*

Krist, J.: 1993, in R. J. Hanisch, R. J. V. Brissenden, and J. Barnes (eds.), *ASP Conf. Ser. 52: Astronomical Data Analysis Software and Systems II*, pp 536–+

Krist, J.: 1995, in R. A. Shaw, H. E. Payne, and J. J. E. Hayes (eds.), *ASP Conf. Ser. 77: Astronomical Data Analysis Software and Systems IV*, pp 349–+

Kuijken, K. and Rich, R. M.: 2002, *AJ* **124**, 2054

Mao, S.: 1992, *ApJ* **389**, 63

Mao, S., Di Stefano, R., Alcock, C., Cook, K., Rhie, S., Allsman, R., Axelrod, T., Freeman, K., Peterson, B., Quinn, P., Rodgers, A., Bennett, D., Perlmutter, S., Griest, K., Marshall, S., Pratt, M., Stubbs, C., and Sutherland, W.: 1994, in *Bulletin of the American Astronomical Society*, Vol. 26 of *Bulletin of the American Astronomical Society*, pp 1336–+

Mao, S. and Paczyński, B.: 1991, *ApJL* **374**, L37

Mao, S., Smith, M. C., Woźniak, P., Udalski, A., Szymański, M., Kubiak, M., Pietrzyński, G., Soszyński, I., and Żebruń, K.: 2002, *MNRAS* **329**, 349

Nemiroff, R. J. and Wickramasinghe, W. A. D. T.: 1994, *ApJL* **424**, L21

Paczyński, B.: 1986, *ApJ* **304**, 1

Paczyński, B.: 1991, *ApJL* **371**, L63

Paczyński, B.: 1996, *ARA&A* **34**, 419

Paczyński, B. and Stanek, K. Z.: 1998, *ApJL* **494**, L219+

Perryman, M. A. C., Lindegren, L., Kovalevsky, J., Hoeg, E., Bastian, U., Bernacca, P. L., Crézé, M., Donati, F., Grenon, M., van Leeuwen, F., van der Marel, H., Mignard, F., Murray, C. A., Le Poole, R. S., Schrijver, H., Turon, C., Arenou, F., Froeschlé, M., and Petersen, C. S.: 1997, *A&A* **323**, L49

Persic, M., Salucci, P., and Stel, F.: 1996, *MNRAS* **281**, 27

Popowski, P.: 2002, *ArXiv Astrophysics e-prints*

Popowski, P., Alcock, C., Allsman, R. A., Alves, D. R., Axelrod, T. S., Becker, A. C., Bennett, D. P., Cook, K. H., Drake, A. J., Freeman, K. C., Geha, M., Griest, K., Lehner, M. J., Marshall, S. L., Minniti, D., Nelson, C. A., Peterson, B. A., Pratt, M. R., Quinn, P. J., Stubbs, C. W., Sutherland, W., Tomaney, A. B., Vandehei, T., and Welch, D.: 2001, in J. W. Menzies and P. D. Sackett (eds.), *Microlensing 2000: A New Era of Microlensing Astrophysics*, Vol. 239 of *Astronomical Society of the Pacific Conference Series*, pp 244–+

Popowski, P., Griest, K., Thomas, C. L., Cook, K. H., Bennett, D. P., Becker, A. C., Alves, D. R., Minniti, D., Drake, A. J., Alcock, C., Allsman, R. A., Axelrod, T. S., Freeman, K. C., Geha, M., Lehner, M. J., Marshall, S. L., Nelson, C. A., Peterson, B. A., Quinn, P. J., Stubbs, C. W., Sutherland, W., Vandehei, T., and Welch, D.: 2005, *ApJ* **631**, 879

Press, W. H., Teukolsky, S. A., Vetterling, W. T., and Flannery, B. P.: 1992, *Numerical recipes in FORTRAN. The art of scientific computing*, Cambridge: University Press, —c1992, 2nd ed.

Rattenbury, N. J., Abe, F., Bennett, D. P., Bond, I. A., Calitz, J. J., Claret, A., Cook, K. H., Furuta, Y., Gal-Yam, A., Glicenstein, J.-F., Hearnshaw, J. B., Hauschildt, P. H., Kilmartin, P. M., Kurata, Y., Masuda, K., Maoz, D., Matsubara, Y., Meintjes, P. J., Moniez, M., Muraki, Y., Noda, S., Ofek, E. O., Okajima, K., Philpott, L., Rhie, S. H., Sako, T., Sullivan, D. J., Sumi, T., Terndrup, D. M., Tristram, P. J., Wood, J., Yanagisawa, T., and Yock, P. C. M.: 2005, *A&A* **439**, 645

Rattenbury, N. J., Mao, S., Debattista, V. P., Sumi, T., Gerhard, O., and de Lorenzi, F.: 2007a, *MNRAS* **378**, 1165

Rattenbury, N. J., Mao, S., Sumi, T., and Smith, M. C.: 2007b, *MNRAS* **378**, 1064

Refsdal, S.: 1964, *MNRAS* **128**, 295

Reid, N.: 1991, *AJ* **102**, 1428

Schechter, P. L., Mateo, M., and Saha, A.: 1993, *PASP* **105**, 1342

Schmidt-Kaler, T.: 1984, *Allen's Astrophysical Quantities*

Sevenster, M. N. and Kalnajs, A. J.: 2001, *AJ* **122**, 885

Sirianni, M., Jee, M. J., Benítez, N., Blakeslee, J. P., Martel, A. R., Meurer, G., Clampin, M., De Marchi, G., Ford, H. C., Gilliland, R., Hartig, G. F., Illingworth, G. D., Mack, J., and McCann, W. J.: 2005, *PASP* **117**, 1049

Smith, M. C., Mao, S., and Woźniak, P.: 2002, *MNRAS* **332**, 962

Smith, M. C., Woźniak, P., Mao, S., and Sumi, T.: 2007, *ArXiv e-prints* 707

Spaenhauer, A., Jones, B. F., and Whitford, A. E.: 1992, *AJ* **103**, 297

Stanek, K. Z.: 1998, *ArXiv Astrophysics e-prints*

Stanek, K. Z., Mateo, M., Udalski, A., Szymański, M., Kałużny, J., and Kubiak, M.: 1994, *ApJL* **429**, L73

Sumi, T.: 2004, *MNRAS* **349**, 193

Sumi, T., Abe, F., Bond, I. A., Dodd, R. J., Hearnshaw, J. B., Honda, M., Honma, M., Kan-ya, Y., Kilmartin, P. M., Masuda, K., Matsubara, Y., Muraki, Y., Nakamura, T., Nishi, R., Noda, S., Ohnishi, K., Petterson, O. K. L., Rattenbury, N. J., Reid, M., Saito, T., Saito, Y., Sato, H., Sekiguchi, M., Skuljan, J., Sullivan, D. J., Takeuti, M., Tristram, P. J., Wilkinson, S., Yanagisawa, T., and Yock, P. C. M.: 2003, *ApJ* **591**, 204

Sumi, T., Woźniak, P. R., Eyer, L., Dobrzycki, A., Udalski, A., Szymański, M. K., Kubiak, M., Pietrzyński, G., Soszyński, I., Żebruń, K., Szewczyk, O., and Wyrzykowski, Ł.: 2005, *MNRAS* **356**, 331

Sumi, T., Woźniak, P. R., Udalski, A., Szymański, M., Kubiak, M., Pietrzyński, G., Soszyński, I., Żebruń, K., Szewczyk, O., Wyrzykowski, Ł., and Paczyński, B.: 2006, *ApJ* **636**, 240

Sumi, T., Wu, X., Udalski, A., Szymański, M., Kubiak, M., Pietrzyński, G., Soszyński, I., Woźniak, P., Żebruń, K., Szewczyk, O., and Wyrzykowski, Ł.: 2004, *MNRAS* **348**, 1439

Syer, D. and Tremaine, S.: 1996, *MNRAS* **282**, 223

Thomas, C. L., Griest, K., Popowski, P., Cook, K. H., Drake, A. J., Minniti, D., Myer, D. G., Alcock, C., Allsman, R. A., Alves, D. R., Axelrod, T. S., Becker, A. C., Bennett, D. P., Freeman, K. C., Geha, M., Lehner, M. J., Marshall, S. L., Nelson, C. A., Peterson, B. A., Quinn, P. J., Stubbs, C. W., Sutherland, W., Vandehei, T., and Welch, D. L.: 2005, *ApJ* **631**, 906

Tisserand, P., Le Guillou, L., Afonso, C., Albert, J. N., Andersen, J., Ansari, R., Aubourg, É., Bareyre, P., Beaulieu, J. P., Charlot, X., Coutures, C., Ferlet, R., Fouqué, P., Glicenstein, J. F., Goldman, B., Gould, A., Graff, D., Gros, M., Haissinski, J., Hamadache, C., de Kat, J., Lasserre, T., Lesquoy, É., Loup, C., Magneville, C., Marquette, J. B., Maurice, É., Maury, A., Milsztajn, A., Moniez, M., Palanque-Delabrouille, N., Perdereau, O., Rahal, Y. R., Rich, J., Spiro, M., Vidal-Madjar, A., Vigroux, L., Zylberajch, S., and The EROS-2 Collaboration: 2007, *A&A* **469**, 387

Tody, D.: 1993, in R. J. Hanisch, R. J. V. Brissenden, and J. Barnes (eds.), *Astronomical Data Analysis Software and Systems II*, Vol. 52 of *Astronomical Society of the Pacific Conference Series*, pp 173–+

Udalski, A.: 2000, *ApJL* **531**, L25

Udalski, A.: 2003, *Acta Astronomica* **53**, 291

Udalski, A., Jaroszyński, M., Paczyński, B., Kubiak, M., Szymański, M. K., Soszyński, I., Pietrzyński, G., Ulaczyk, K., Szewczyk, O., Wyrzykowski, Ł., Christie, G. W., DePoy, D. L., Dong, S., Gal-Yam, A., Gaudi, B. S., Gould, A., Han, C., Lépine, S., McCormick, J., Park, B.-G., Pogge, R. W., Bennett, D. P., Bond, I. A., Muraki, Y., Tristram, P. J., Yock, P. C. M., Beaulieu, J.-P., Bramich, D. M., Dieters, S. W., Greenhill, J., Hill, K., Horne, K., and Kubas, D.: 2005, *ApJL* **628**, L109

Udalski, A., Kubiak, M., and Szymański, M.: 1997, *Acta Astronomica* **47**, 319

Udalski, A., Szymański, M., Kałużny, J., Kubiak, M., Krzemiński, W., Mateo, M., Preston, G. W., and Paczyński, B.: 1993, *Acta Astronomica* **43**, 289

Udalski, A., Szymański, M., Kałużny, J., Kubiak, M., Mateo, M., Krzemiński, W., and Paczyński, B.: 1994a, *Acta Astronomica* **44**, 227

Udalski, A., Szymański, M., Kubiak, M., Pietrzyński, G., Soszyński, I., Woźniak, P., Żebruń, K., Szewczyk, O., and Wyrzykowski, Ł.: 2002, *Acta Astronomica* **52**, 217

Udalski, A., Szymański, M., Mao, S., Di Stefano, R., Kałużny, J., Kubiak, M., Mateo, M., and Krzemiński, W.: 1994b, *ApJL* **436**, L103

Udalski, A., Szymański, M., Stanek, K. Z., Kałużny, J., Kubiak, M., Mateo, M., Krzemiński, W., Paczyński, B., and Venkat, R.: 1994c, *Acta Astronomica* **44**, 165

Uglesich, R. R., Crotts, A. P. S., Baltz, E. A., de Jong, J., Boyle, R. P., and Corbally, C. J.: 2004, *ApJ* **612**, 877

Walsh, D., Carswell, R. F., and Weymann, R. J.: 1979, *Nature* **279**, 381

Witt, H. J. and Mao, S.: 1994, *ApJ* **430**, 505

Wood, A.: 2006, *PhD thesis, The University of Manchester, UK*

Wood, A.: 2007, *ArXiv e-prints* 707

Wood, A. and Mao, S.: 2005, *MNRAS* **362**, 945

Woźniak, P. and Paczyński, B.: 1997, *ApJ* **487**, 55

Woźniak, P. R.: 2000, *Acta Astronomica* **50**, 421

Woźniak, P. R., Kozłowski, S., Vestrand, W. T., and Mao, S.: 2005, in *Bulletin of the American Astronomical Society*, Vol. 37 of *Bulletin of the American Astronomical Society*, pp 1383–+

Woźniak, P. R., Udalski, A., Szymański, M., Kubiak, M., Pietrzyński, G., Soszyński, I., and Żebruń, K.: 2001, *Acta Astronomica* **51**, 175

Wyrzykowski, Ł.: 2005, *PhD thesis, Warsaw University, Poland*

Wyrzykowski, Ł., Udalski, A., Mao, S., Kubiak, M., Szymański, M. K., Pietrzyński, G., Soszyński, I., and Szewczyk, O.: 2006, *Acta Astronomica* **56**, 145

Yoo, J., DePoy, D. L., Gal-Yam, A., Gaudi, B. S., Gould, A., Han, C., Lipkin, Y., Maoz, D., Ofek, E. O., Park, B.-G., Pogge, R. W., Udalski, A., Soszyński, I., Wyrzykowski, Ł., Kubiak, M., Szymański, M., Pietrzyński, G., Szewczyk, O., and Żebruń, K.: 2004, *ApJ* **603**, 139

Zhao, H., Rich, R. M., and Biello, J.: 1996, *ApJ* **470**, 506

Zhao, H., Spergel, D. N., and Rich, R. M.: 1994, *AJ* **108**, 2154

Zhao, H., Spergel, D. N., and Rich, R. M.: 1995, *ApJL* **440**, L13

Zwicky, F.: 1937, *ApJ* **86**, 217